High energy processes in young stellar objects and high-mass X-ray binaries
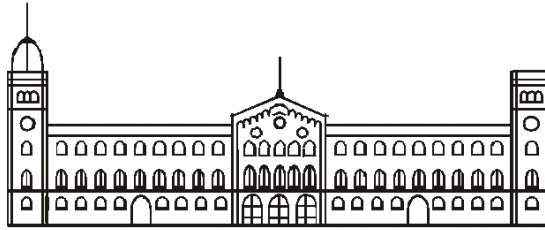
Pere Munar i Adrover

UNIVERSITAT DE BARCELONA

DEPARTAMENT D'ASTRONOMIA I METEOROLOGIA

High energy processes in young stellar objects and high-mass X-ray binaries

Pere Munar i Adrover

BARCELONA (SPAIN), MARCH 2014

PROGRAMA DE DOCTORAT EN FÍSICA
LÍNIA DE RECERCA EN ASTRONOMIA I ASTROFÍSICA
2010-2014

Memòria presentada per **Pere Munar i Adrover**
per optar al grau de Doctor en Física

Director i Tutor

Prof. Josep Maria Paredes Poy

Contents

CONTENTS

Resum de la tesi

Processos d'alta energia en objectes estel·lars joves i binàries de raigs X d'alta massa

L'astrofísica d'altes energies i en concret l'astrofísica de raigs gamma, estudia els processos d'emissió que no poden ser causats per matèria calenta, sinó per altres mecanismes que anomenem *no tèrmics* i que comporten que la matèria que emet aquesta radiació tingui energies per sobre d'1 MeV. Actualment disposem d'un bon nombre d'instruments capaços de detectar aquesta emissió, com ara els satèl·lits *Fermi* i *AGILE* o els telescopis Cherenkov com MAGIC, a la superfície terrestre.

En aquesta tesi hem estudiat principalment dos tipus de sistemes que, tal com s'ha observat o predit teòricament, poden produir radiació gamma: els objectes estel·lars joves i els sistemes binaris de raigs X d'alta massa.

Els objectes estel·lars joves els trobem a les regions de formació estel·lar, que són els bressols on noves estrelles s'estan formant. Aquestes regions consten sobretot de núvols de gas o pols que són escalfats per la radiació que emeten les estrelles joves i les protoestrelles al seu interior. Les característiques d'aquestes regions són principalment la seva elevada densitat i la seva *opacitat* a la radiació òptica, que fa que molts cops apareguin com a regions fosques sobre el fons d'estrelles. La manera que tenim d'estudiar aquestes regions és per mitjà d'altres longituds d'ona, com ara l'infraroig o les ones de ràdio. Aquests dos tipus de radiació poden escapar fàcilment dels núvols moleculars i gràcies a això coneixem el que succeeix al seu interior.

Els pobladors de les regions de formació estel·lar són les protoestrelles i les estrelles joves, entre altres objectes celests. Les protoestrelles són l'estadi que predeceix a la seqüència principal d'una estrella. En aquest estadi de la seva evolució, trobem que la protoestrella està encara acretant matèria del núvol progenitor a través d'un disc d'acreció, i al mateix temps expulsa material en direcció perpendicular a aquest disc per mitjà d'uns dolls formats per interacció magnètica. En aquests dolls de matèria les partícules són expulsades a grans velocitats cap a fora del sistema. En alguns casos, aquestes partícules assoleixen velocitats relativistes tal com evidencia la detecció d'emissió ràdio no tèrmica en alguns d'aquests objectes.

En aquesta tesi ens hem interessat per trobar evidència de més objectes estel·lars joves que presentin emissió no tèrmica, ja sigui en el rang dels raigs X o, sobretot, en el rang

dels raigs gamma. Per a trobar nous candidats hem aprofitat el primer catàleg del satèl·lit *Fermi* i l'hem creuat amb catàlegs d'objectes joves de la Galàxia. D'aquest creuament n'ha sorgit una llista de fonts candidates a ser les contrapartides de certes emissions en raigs gamma detectades per *Fermi*. A més, per tal d'avaluar la validesa estadística de la nostra llista de candidates, hem realitzat simulacions emprant el mètode de Monte Carlo. Aquestes simulacions ens mostren que els objectes estel·lars joves coincidents amb fonts del catàleg de *Fermi* tenen una probabilitat molt baixa de ser coincidències per atzar. En el cas d'altres poblacions d'objectes joves, com ara estrelles massives amb forts vents, o associacions OB, la probabilitat de que tinguem coincidències per atzar és més elevada. Per a les coincidències d'objectes estel·lars joves amb fonts *Fermi*, hem fet una exploració més detallada al voltant d'aquestes fonts per tal d'identificar o descartar altres possibles candidats a contrapartida de la font gamma.

A més a més de la cerca per mitjà de catàlegs, hem fet un estudi en raigs X a partir de dades d'arxiu disponibles sobre un objecte estel·lar jove del que ja es coneix emissió no tèrmica en ràdio: IRAS 16547-4247. Aquest objecte és una protoestrella que encara acreta material per mitjà d'un disc d'acreció i que alhora expulsa material a través de dolls de partícules. Aquests dolls acaben xocant amb el medi que envolta la protoestrella i donen lloc a l'emissió ràdio no tèrmica. Treballs teòrics recents prediuen que aquests tipus d'objectes, a demés de presentar emissió ràdio no tèrmica, podrien ser emissors de raigs gamma. IRAS 16547-4247 és una de les protoestrelles més brillants en l'infrariog i en ràdio i per això ens n'hem interessat. Hem analitzat una observació feta amb *XMM-Newton* al 2004 i hem descobert la contrapartida en raigs X d'aquest objecte. Malauradament no podem fer un estudi de l'espectre ja que la detecció és marginal. Tot i així, podem afirmar que es tracta d'emissió dura en raigs X, i que si prové del xoc dels dolls amb el medi, seria l'emissió d'aquesta naturalesa més dura mai detectada en una protoestrella. D'altra banda, hem realitzat un estudi teòric d'aquesta font per tal de veure si la nostra detecció en raigs X és compatible amb el que s'havia predit teòricament fins ara, i hem vist que necessitem explicar la detecció amb un model tèrmic, enlloc de no tèrmic. A pesar d'això, amb el nostre model encara predim certa quantitat de raigs gamma que podrien ser detectables en un futur.

Finalment, hem estudiat una regió de formació estel·lar que s'ha trobat en coincidència espacial amb una font del segon catàleg de *Fermi*, coneguda com Monoceros R2, que es troba a la Constel·lació de l'Unicorn. Aquesta regió s'ha observat en ràdio i en l'infraroig i és coneguda per contenir un bon nombre d'objectes estel·lars joves tant de baixa massa (com estrelles tipus T-Tauri) com d'alta massa, entre els que destaca la font IRS3. Aprofitant que les dades de *Fermi* són públiques, hem analitzat més de tres anys d'observacions centrades en aquesta regió i l'hem confirmada com a emissora de raigs gamma. Hem obtingut una corba de llum i un espectre que ens permeten comparar la nostra font amb els estudis teòrics que prediuen emissió gamma en protoestrelles. Els nostres resultats ens permeten dir que l'emissió gamma detectada és compatible amb el que s'esperaria

que produïssin un conjunt de ∼100 o més estrelles tipus T-Tauri i/o amb el que s'espera d'objectes estel·lars joves massius amb dolls de matèria. A manca d'altres fonts candidates a contrapartida de la font de raigs gamma, podem dir que Monoceros R2 podria ser la primera regió de formació estel·lar detectada en raigs gamma.

Dins de l'altre gran bloc d'aquesta tesi trobem les estrelles binàries de raigs X d'alta massa. Aquests objectes estan formats per una estrella d'alta massa, del tipus espectral O, Be o A, i un objecte compacte que pot ser o bé un estel de neutrons o bé un forat negre. Dels tres sistemes binaris que hem estudiat en aquesta tesi, a MWC 656 sembla clar que l'objecte compacte és un forat negre, mentre que a HESS J0632+057 i SS-433 encara no se n'ha pogut esbrinar la natura de l'objecte.

El cas més rellevant dels que hem estudiat és el de MWC 656. Aquest sistema està format per una estrella Be i un forat negre, una combinació que mai s'havia detectat, tot i que hi havia prediccions de la possible existència d'aquest tipus de sistemes. Aquest sistema binari va cridar l'atenció a causa d'una emissió puntual de raigs gamma detectada pel satèl·lit *AGILE*, de la que MWC 656 aviat va ser proposada com a contrapartida. Després de ser confirmada com a sistema binari s'ha descobert que l'objecte compacte és un forat negre. Nosaltres hem observat aquesta font amb el telescopi de raigs X *XMM-Newton* i amb els Telescopis MAGIC, en raigs gamma de molt alta energia. La nostra observació de raigs X ha suposat la descoberta de la contrapartida de raigs X d'aquest sistema binari i ens ha permès classificar-la com a binària de raigs X d'alta massa, essent el primer cas que s'ha trobat de HMXB amb Be i forat negre.. El flux observat és molt baix, i això ens indica que la font està en un estat de quiescència[1], on l'acreció cap al forat negre ocorre a un ritme molt baix. La detecció ha estat marginal, motiu pel qual l'espectre que obtenim no és tan precís com voldríem, però ens ha permès estudiar aquesta binària dins el context de la correlació trobada fa uns anys entre emissió en raigs X i ràdio per a sistemes binaris (de baixa massa en general) que contenen un forat negre. Juntament amb límits superiors a l'emissió ràdio obtinguts per membres del nostre grup, podem afirmar que la nostra detecció en raigs X és compatible amb l'esmentada correlació, i que aquesta és extensible a binàries d'alta massa amb forats negres en estat de quiescència.

Amb els Telescopis MAGIC hem observat MWC 656 també, però en aquest cas no l'hem detectada. Aquest fet no ens sorprèn ja que, donada l'emissió mesurada en raigs X, el flux que podríem esperar és molt baix, si ho comparem amb l'altra binària d'alta massa que conté un forat negre a la nostra galàxia (Cygnus X-1), de manera que fins i tot si trobéssim la font en un estat explossiu, una detecció seria difícil pels actuals telescopis Cherenkov.

Altres sistemes que hem estudiat amb MAGIC són HESS J0632+057 i SS 433.

HESS J0632+057 és un sistema binari format per una estrella Be i un objecte compacte

---

[1]En els sistemes binaris amb forat negre es distingeixen diversos estats depenent del règim d'acreció del forat negre. L'estat de quiescència està caracteritzat per una acreció molt baixa amb una presència molt baixa o nul·la d'emissió ràdio i una també molt feble emissió en raigs X.

de natura desconeguda. Durant el transcors d'aquesta tesi altres autors van confirmar HESS J0632+057 com a sistema binari i després va ser detectat per nosaltres com a emissor de raigs gamma. Tot i que no es coneix el tipus d'objecte compacte, estudis recents suggereixen que aquest podria ser un estel de neutrons no acretant que produeix un vent molt fort de partícules relativistes.

Vàrem observar HESS J0632+057 amb MAGIC durant una campanya entre els anys 2010 i 2011. Al febrer de 2011 el satèl·lit de raigs X *Swift* va detectar un increment en el flux de raigs X d'aquesta font i va ser llavors quan es va decidir que MAGIC la tornés a observar. Durant les dues primeres setmanes de febrer es detectà emissió de raigs gamma de molt alta energia provinent de HESS J0632+057 i posteriorment la font es va tornar a apagar. El nou espectre obtingut en raigs gamma de molt alta energia millora l'espectre mesurat quan es va descobrir la font, ja que ara l'emissió detectada s'extén a baixes energies fins a arribar als ~ 140 GeV. L'emissió detectada és compatible amb que sigui produïda per interacció de Compton invers dels electrons relativistes presents i els fotons de l'estrella companya.

Per acabar, amb els Telescopis MAGIC també hem observat SS 433, el primer microquàsar que es va descobrir, ja fa més de 30 anys. Aquest sistema binari és diferent dels altres dos ja que conté una estrella de tipus espectral A, que és orbitada per un objecte compacte que podria ser un forat negre. Recentment, però, la natura de l'objecte compacte s'ha posat en dubte, i alguns treballs suggereixen que es tracta d'un estel de neutrons. Sigui quina sigui la natura de l'objecte compacte, aquest està acretant matèria de l'estrella companya i alhora n'expulsa per mitjà de dolls perpendiculars al disc d'acreció. Es creu que, si el sistema emet radiació gamma de molt alta energia, aquesta hauria de produir-se en aquests dolls, on s'espera que electrons i protons siguin accelerats per mitjà de xocs i altres mecanismes. L'estrella companya i l'objecte compacte estan envoltats per un disc de material prou dens i calent com per a que sigui una possible font d'absorció dels fotons d'alta energia. Aquest disc, a més, presenta un moviment de precessió amb un període de 162 dies, de manera que només hi ha una finestra curta de temps en què, des de la Terra, podem veure les regions més internes del sistema. En aquesta finestra de temps és quan esperem detectar la radiació gamma, si n'hi ha. Cal fer esment també que tal com veiem el sistema des de la Terra, l'estrella companya eclipsa l'objecte compacte cada 13 dies, i aquests eclipsis són també una font important d'absorció de la possible radiació gamma.

Hem observat aquesta font durant els mesos de maig i juny de 2010 però no s'ha detectat. Així, hem calculat límits superiors a l'emissió gamma de molt alta energia que serveixen per a posar restriccions en paràmetres físics, com ara l'eficiència en l'acceleració de partícules en el doll. D'aquesta manera es poden anar refinant els models teòrics que prediuen l'emissió gamma. Amb les restriccions que hem pogut derivar, sembla difícil que els actuals telescopis Cherenkov puguin arribar a detectar aquesta binària. Esperem però, que amb la propera generació de telescopis Cherenkov, amb CTA al capdavant, puguem arribar a detectar-la.

1
Introduction

1.1 High-energy astrophysics

High-energy astrophysics involves all the disciplines in the astrophysics field that are focused in the study of the processes involved in the emission of photons with energies at the X-ray domain and above. Above a certain energy in the X-rays, the emitted photons cannot be related to hot matter anymore. Thus, other mechanisms need to be invoked: non-thermal mechanisms. These processes are capable to inject large amounts of energy into a single particle. The physical scenarios where these phenomena take place are of various nature, usually related to strong shocks, powerful winds of massive stars, relativistic outflows ejected in the cores of active galactic nuclei (AGN), etc. In these scenarios, relativistic particles interact with the ambient matter, the magnetic fields and/or the photon fields to produce the detected gamma-ray emission.

The current generation of detectors have provided an unprecedented sensitivity and spatial resolution to study the extreme universe. In the high-energy (HE) gamma-ray domain, the space missions such as *AGILE* and *Fermi*/LAT provide the scientific community with unvaluable data from processes with energies ranging from 0.3 to 300 GeV. They are continuously studying AGN, gamma-ray bursts (GRB), binary systems, etc., with excellent results. The current distribution of HE gamma-ray sources detected by the *Fermi*/LAT telescope can be seen in the Figure 1.1. For processes producing even higher energy radiation we take advantage from the Atmospheric Imaging Cherenkov Telescopes (IACTs), which with their big collecting areas are capable to detect the few >100 GeV photons that make their trip to the Earth through the air showers developed when the VHE photons interact with the atmosphere. The current VHE source catalog comprise
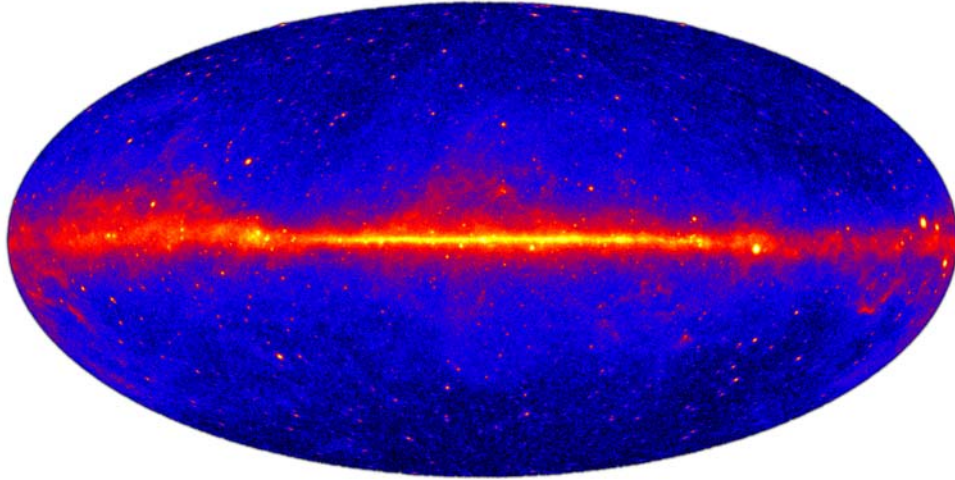
Figure 1.1: High-energy gamma-ray sky map obtained with the *Fermi*/LAT satellite represented in galactic coordinates. The image has been obtained from five years of integration time in the energy range above 1 GeV. Image from `http://fermi.gsfc.nasa.gov/ssc/`.

147 sources (see `http://tevcat.uchicago.edu/`), as can be seen in Figure 1.2, from AGN to gamma-ray binaries.

Gamma-ray emission has been historically related to very energetic and violent scenarios as the ones cited above. However, in recent times different studies have speculated with the possibility of gamma radiation produced in other less-energetic environments, such as young stellar objects (YSO) and star-forming regions (SFR).

The next generation of IACTs, embodied in the Cherenkov Telescope Array (CTA), will suppose a huge leap for the astrophysics and astroparticle physics communities. The capabilities of CTA suppose an increase in one order of magnitude in sensitivity and spatial resolution.

1.2 High-energy emission processes

The detected high-energy photons are produced in a variety of processes in which particles are accelerated up to relativistic energies and interact with the ambient medium. Here we give a brief description of the main mechanisms that have been taken into account throughout this thesis in order to explain the different observed and predicted emissions from YSOs and high-mass X-ray binaries (HMXBs). Depending on the kind of interaction of the relativistic particles with the ambient we can find: thermal or relativistic Bremsstrahlung emission, when particles interact with the electric field of charged particles; synchrotron emission, when relativistic electrons spin around magnetic field lines; inverse Compton, when the particles collide with the ambient photon field; pp-collisions, when relativistic protons collide with other protons. All these processes are explained in
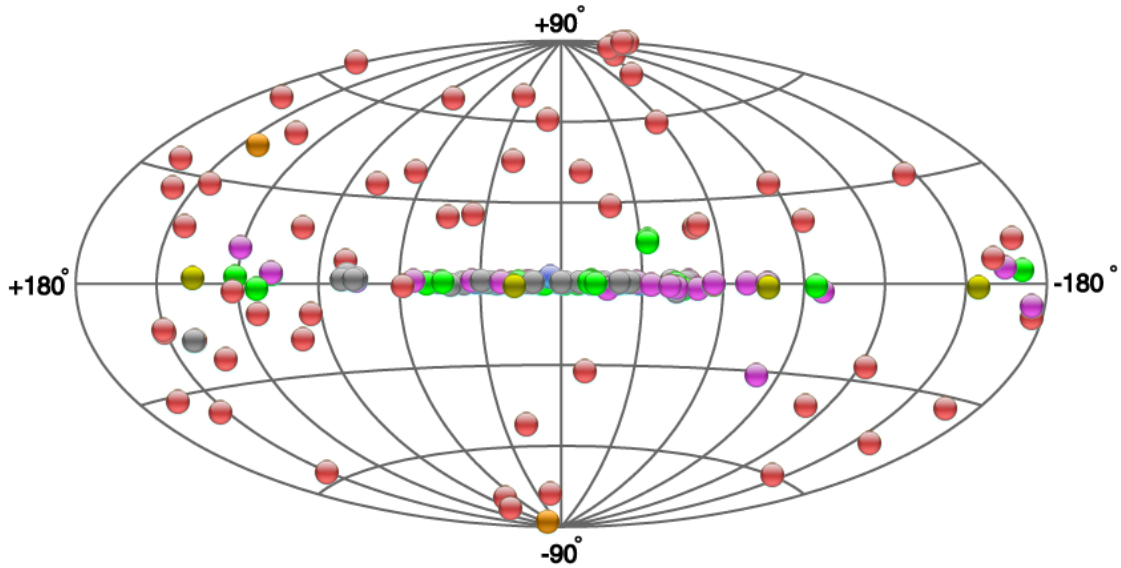
Figure 1.2: Distribution of very high-energy gamma-ray sources (E > 100 GeV) represented in galactic coordinates. Yellow circles represent gamma-ray binaries. Image courtesy of Scott Wakely and Deirdre Horan. An up-to-date plot can be found at `http://tevcat.uchicago.edu/` (latest update is 01-2014)

the following subsections. We denote the interacting particle energy by its Lorentz factor γ and the emitted photon energy by ϵ.

1.2.1 Bremsstrahlung

A charged particle, an electron for instance, traveling within a medium populated with nuclei will interact with their electric fields. This interaction will cause a change in the velocity of the electron, thus an acceleration, which results in the emission of a photon. This radiation was called "braking-radiation", or in German, *Bremsstrahlung* emission. The process is identical to the so called *free–free* emission because is related to the transition between unbound states of the electron in the field of the nucleus. To see the complete mathematical treatment to derive the next expressions for the Bremsstrahlung radiation, we refer to Longair (2011).

The Bremsstrahlung low-frequency radiation spectrum of a high-energy but non relativistic electron is given by

$$I(\nu) = \frac{Z^2 e^6 N}{12\pi^3 \epsilon_0^3 c^3 m_e^2} \frac{1}{\text{v}} \ln \Lambda \tag{1.1}$$

where Z is the atomic number of the interacting nuclei, N is the number density of nuclei (in cm^{-3}), v is the electron's velocity in the observer's reference frame, ϵ_0 is the permittivity of free space, and $\Lambda = b_{\text{max}}/b_{\text{min}}$ is the ratio of the maximum and minimum impact

parameters of the electron. Depending on the velocity of the electron, the parameter Λ can be approximated by

$$\Lambda = \begin{cases} \frac{4\epsilon_0 m_e \mathrm{v}^3}{Ze^2\nu} & \text{for low velocities} \\ \frac{2m_e \mathrm{v}^2}{h\nu} & \text{for high velocities} \end{cases} \tag{1.2}$$

The energy loss-rate of the electron can be computed by integrating expression 1.1 over all frequencies:

$$-\left(\frac{\mathrm{d}E}{\mathrm{d}t}\right) \approx \int_0^{\nu_{\max}} I(\nu)\mathrm{d}\nu \approx \frac{Z^2 e^6 N\mathrm{v}}{24\pi\epsilon_0 c^3 m_e \hbar} \ln\Lambda \tag{1.3}$$

To derive the spectrum of Bremsstrahlung radiation of a thermal plasma at temperature T, the expression for low-frequency spectral emissivity of one electron should be integrated over the collision parameters and over the Maxwellian distribution of velocities of the plasma

$$N_e(\mathrm{v})\mathrm{d}\mathrm{v} = 4\pi N_e \left(\frac{m_e}{2\pi k_B T}\right)^{3/2} \mathrm{v}^2 \exp\left(\frac{m_e \mathrm{v}^2}{2k_B T}\right)\mathrm{d}\mathrm{v} \tag{1.4}$$

where k_B is Boltzmann's constant.

The approximate resulting spectral emissivity of a plasma of electrons with number density N_e in the low-frequency limit is

$$I(\nu) = \frac{Z^2 e^6 N N_e}{12\sqrt{3}\pi^3 \epsilon_0^3 c^3 m_e^2} \left(\frac{m_e}{k_B T}\right)^{1/2} g(\nu, T) \tag{1.5}$$

where $g(\nu, T)$ is the Gaunt factor. It is worth noting that the low-frequency spectrum is more or less independent of frequency, being this dependence only present in the Gaunt factor. Finally, the total energy loss rate of the plasma may be found by integrating over all frequencies.

$$-\left(\frac{\mathrm{d}E}{\mathrm{d}t}\right) = (\text{constant})Z^2 T^{1/2} N N_e \bar{g} \tag{1.6}$$

Detailed calculations give the following expression for the spectral emissivity of the plasma

$$I(\nu) = \frac{1}{3\pi^2} \left(\frac{\pi}{6}\right)^{1/2} \frac{Z^2 e^6}{\epsilon_0^3 c^3 m_e^2} \left(\frac{m_e}{k_B T}\right)^{1/2} g(\nu, T) N N_e \exp\left(-\frac{h\nu}{k_B T}\right) \tag{1.7}$$

At frequencies $h\nu \ll k_B T$, the Gaunt factor has only logarithmic dependency on frequency. The approximate expressions for radio and X-rays are:

$$\text{Radio,} \quad g(\nu, T) = \frac{\sqrt{3}}{2\pi}\left[\ln\left(\frac{128\epsilon_0^2 k_B^3 T^3}{m_e e^4 \nu^2 Z^2 \hbar}\right) - \xi^2\right] \tag{1.8}$$

$$\text{X-rays,} \quad g(\nu, T) = \frac{\sqrt{3}}{\pi}\ln\left(\frac{k_B T}{h\nu}\right) \tag{1.9}$$

where $\xi = 0.577$ is the Euler's constant. For frequencies $h\nu \gg k_B T$ the Gaunt factor can be approximated by $g(\nu, T) \approx (h\nu/k_B T)^{1/2}$.

1.2.2 Relativistic Bremsstrahlung

When the electron velocity reaches the relativistic limit, some considerations must be taken into account. The cross section for the relativistic case is given by (Lang 1999)

$$\sigma_{Br}(\gamma, \epsilon) = \frac{4\alpha r_e^2 Z^2}{\epsilon} \phi(\gamma, \epsilon) \tag{1.10}$$

where $r_e = e^2/m_e c^2$ is the classical radius of the electron and $\alpha \approx 1/137$ is the fine structure constant. The function $\phi(\gamma, \epsilon)$ takes different forms, depending on whether the electron interacts with a screened nucleus or with a naked nucleus. For a completely screened nucleus

$$\phi(\gamma, \epsilon) = \left[1 + \left(1 - \frac{\epsilon}{\gamma m_e c^2} \right)^2 - \frac{2}{3} \left(1 - \frac{\epsilon}{\gamma m_e c^2} \right) \right] \ln \left(\frac{191}{z^{1/3}} \right) + \frac{1}{9} \left(1 - \frac{\epsilon}{\gamma m_e c^2} \right) \tag{1.11}$$

and for a naked nucleus

$$\phi(\gamma, \epsilon) = \left[1 + \left(1 - \frac{\epsilon}{\gamma m_e c^2} \right)^2 - \frac{2}{3} \left(1 - \frac{\epsilon}{\gamma m_e c^2} \right) \right] \left[\ln \frac{2(\gamma m_e c^2 - \epsilon)}{m_e c^2} - \frac{1}{2} \right] \tag{1.12}$$

The cross section of this interaction is known for the reference frame where the target particles are at rest.

The intensity of the relativistic Bremsstrahlung emission of an electron population can be calculated by integrating over all the electron energies:

$$I_{Br}(\epsilon) = \int_\epsilon^\infty n_{\text{nuc}} \sigma_{Br}(\gamma, \epsilon) P_e(\gamma) \mathrm{d}\gamma \tag{1.13}$$

where $P_e(\gamma)$ is the electron energy distribution and n_{nuc} is the number density of target nuclei.

The relativistic Bremsstrahlung losses for relativistic electrons that encounter an atom nucleus are huge: the electron gives almost all of its energy to the emitted photon. The losses can be calculated as follows:

$$-\left(\frac{\mathrm{d}\gamma}{\mathrm{d}t} \right)_{Br} = c n_{\text{nuc}} \int_0^{m_e c^2(\gamma - 1)} \epsilon \sigma_{Br}(\gamma, \epsilon) \mathrm{d}\epsilon \tag{1.14}$$

In the case of a fully ionized plasma the losses result

$$-\left(\frac{\mathrm{d}\gamma}{\mathrm{d}t} \right)_{Br} = 4 n_{\text{nuc}} r_e^2 \alpha c Z^2 \left[\ln(2\gamma) - \frac{1}{3} \right] \gamma \tag{1.15}$$

and in the case of full screening

$$-\left(\frac{\mathrm{d}\gamma}{\mathrm{d}t}\right)_{Br} = 4n_{\mathrm{nuc}}r_e^2\alpha cZ^2 \left[\ln\left(\frac{183}{Z^{1/3}}\right) - \frac{1}{8}\right]\gamma \tag{1.16}$$

The energy losses for both cases are linearly dependent on the electron's energy and, in the case of the naked nucleus, there is also an additional small, logarithmic dependence on the electron's energy. If the injected electron population follows a powerlaw with spectral index p, the emitted photons will display a photon index p as well. Thus, the relativistic Bremsstrahlung losses do not modify the spectral index of the injection.

1.2.3 Synchrotron

Charged particles traveling with velocity $\mathbf{v}$ interact with the ambient magnetic field $\mathbf{B}$ and this interaction is driven by the Lorentz force. An accurate description of this emission channel is given in Ginzburg & Syrovatskii (1964). The charged particle will spin around the magnetic field line and start radiating due to the centripetal acceleration. The relativistic expression for the total power radiated by a charged particle in a magnetic field is

$$P = \frac{2}{3}\left(\frac{m_e}{m}\right)^2 cr_e^2\gamma^2 B^2 \sin^2\phi \tag{1.17}$$

where ϕ is the angle between the velocity vector of the charged particle and the magnetic field, known also as *pitch angle*. The dependency of the emitted power on the particle mass implies that these losses will be much more important for electrons than for protons, since the ratio of masses is $m_p/m_e = 1836$. The energy loss per time unit is obtained from the expression for the power. Introducing the Thompson cross section

$$\sigma_{\mathrm{T}} = \frac{8\pi}{3}\left(\frac{e^2}{m_ec^2}\right)^2 = \frac{8\pi}{3}r_e^2 \tag{1.18}$$

and averaging over the angle ϕ assuming an isotropic emission, the synchrotron losses can be expressed as

$$-\left(\frac{\mathrm{d}\gamma}{\mathrm{d}t}\right)_{sync} = \frac{4}{3}\left(\frac{m_e}{m}\right)^2 c\sigma_{\mathrm{T}}\omega_{\mathrm{mag}}\gamma^2 \tag{1.19}$$

where $\omega_{\mathrm{mag}} = B^2/8\pi$ is the magnetic energy density.

The spectral energy distribution of a particle emitting synchrotron radiation in an isotropic magnetic field is given by

$$P(\gamma,\epsilon,\phi) = \frac{\sqrt{3}e^3 B\sin\phi}{hmc^2}x\int_x^\infty K_{5/3}(\zeta)\mathrm{d}\zeta \tag{1.20}$$

where ϵ is the energy of the emitted radiation, $x = \epsilon/E_c$, $K_{5/3}(\zeta)$ is the modified Bessel

function of order 5/3, and E_c is the characteristic energy, defined as

$$E_c = \frac{3}{4\pi} \frac{hBe\sin\phi}{mc} \gamma^2 \tag{1.21}$$

An aproximation that is commonly used is

$$F(x) = x \int_x^\infty K_{5/3}(\zeta)\mathrm{d}\zeta \simeq 1.85 x^{1/3} e^{-x} \tag{1.22}$$

The uncertainty introduced by this simplification is only of a few per cent up to photon energies of $10E_c$ and is accepted for the purposes ot this thesis.

For a distribution of particles with a certain spectral energy distribution, the radiation emitted by all of them can be computed by integrating the power emitted by a single particle over the parent particle distribution:

$$j(\epsilon) = \int_{\Omega_\phi} \int_{\gamma_{min}}^{\gamma_{max}} P(\gamma, \epsilon, \phi) \, n(\gamma, \phi) \, \mathrm{d}\gamma \mathrm{d}\Omega_\phi \tag{1.23}$$

For an isotropic powerlaw distribution of particles, $n(\gamma, \phi)\,\mathrm{d}\gamma = K_0 \gamma^{-p}\mathrm{d}\gamma$, the power spectrum of the synchrotron radiation will be another powerlaw, $j(\epsilon) \propto \epsilon^{-\alpha}$, where

$$\alpha = \frac{p-1}{2} \tag{1.24}$$

There is a self-absorption process that affects the synchrotron emission, producing a range of frequencies in which we enter in a high-opacity regime. This self-absorption is given by (Pacholczyk 1970):

$$\kappa(\epsilon) = \frac{\sqrt{3}e^3 h^2 B \sin\phi}{8\pi\epsilon^2 m^2 c^2} \int_{\gamma_{min}}^{\gamma_{max}} \gamma^2 \frac{\mathrm{d}}{\mathrm{d}\gamma}\left(\frac{n(\gamma)}{\gamma^2}\right) F(x)\mathrm{d}\gamma \tag{1.25}$$

The total intensity of the radiation emitted by a population of relativistic electrons in a region of thickness s is given by the solution of the transfer equation

$$\frac{\mathrm{d}I(s)}{\mathrm{d}s} = j(\epsilon) - \kappa(\epsilon) I(s) \tag{1.26}$$

The solution, taking into account that $\kappa\mathrm{d}s = \mathrm{d}\tau$, where τ is the optical depth at a given frequency, is then

$$I(\tau) = \frac{j(\epsilon)}{\kappa(\epsilon)}\left(1 - e^{-\tau}\right) \tag{1.27}$$

For an optically thin source ($\tau < 1$) the slope of the intensity is $\alpha = \frac{p-1}{2}$. In the range of frequencies corresponding to the high-opacity regime ($\tau > 1$) the slope of the distribution of the radiated photons changes to $\frac{5}{2}$.

1.2.4 Inverse Compton

In the astrophysical environments that we treat throughout this thesis we find young massive stars that have strong winds and strong photon fields. Relativistic particles present in the environment, such as electrons, may have higher momentum than the ambient photons, and collisions between them may occur. The electrons will give to the photons part of their energy and thus produce high-energy gamma radiation, up to few tens of TeV. This process is known as *inverse Compton scattering* because in this case is the electron the particle which loses energy and the photon the particle that gains energy. The differential cross-section of the process over all the directions is given by the following formula (Blumenthal & Gould 1970):

$$\frac{\mathrm{d}\sigma_{IC}(\epsilon_0, \epsilon, \gamma)}{\mathrm{d}\epsilon} = \frac{3\sigma_{\mathrm{T}}}{4\epsilon_0\gamma^2}\left[2x\ln x + x + 1 - 2x^2 + \frac{(4\epsilon_0\gamma x)^2}{2\left(1 + 4\epsilon_0\gamma x\right)}\left(1 - x\right)\right] \tag{1.28}$$

where $x = \epsilon/\left[4\epsilon_0\gamma^2\left(1 - \epsilon/\gamma\right)\right]$. This expression is valid for the Thompson regime ($\epsilon_0\gamma \ll 1$) and also for the Klein-Nishina regime ($\epsilon_0\gamma \gg 1$).

With the cross-section one can calculate the emissivity of a distribution of photons scattered by a population of electrons isotropicaly distributed in the emitting region

$$J_{IC}\left(\epsilon\right) = m_e c^2 \int_{\gamma_{min}}^{\gamma_{max}} \int_{1/4\gamma^2 \leq x \leq 1}^{\infty} \epsilon_0 n_e\left(\gamma\right) u_{\mathrm{ph}}\left(\epsilon_0\right) \frac{\mathrm{d}\sigma_{\mathrm{IC}}\left(\epsilon_0, \epsilon, \gamma\right)}{\mathrm{d}\epsilon}\mathrm{d}\epsilon_0\mathrm{d}\gamma \tag{1.29}$$

where u_{ph} is the target photon density.

The energy loss-rate of relativistic electrons in a monoenergetic field of photons with energy ϵ_0 and a number density n_{ph} is given by (Aharonian & Atoyan 1981)

$$-\left(\frac{\mathrm{d}\gamma}{\mathrm{d}t}\right) = \frac{3\sigma_{\mathrm{T}}cn_{\mathrm{ph}}}{4\epsilon_0 b}\left[\left(6 + \frac{b}{2} + \frac{6}{b}\right)\ln(1 + b) - \ln^2(1 + b) - \right.$$
$$\left. 2L_{\mathrm{i}}\left(\frac{1}{1 + b}\right) - \frac{(11/12)b^3 + 8b^2 + 13b + 6}{(1 + b)^2}\right] \tag{1.30}$$

where $L_{\mathrm{i}} = \int_x^1 (1 - y)^{-1}\ln y \mathrm{d}y$ and $b = 4\epsilon_0\gamma$. In the Thompson and Klein-Nishina regimes this losses can be expressed as the known expressions (Aharonian 2004):

$$-\frac{\mathrm{d}\gamma}{\mathrm{d}t} = \begin{cases} \frac{4}{3}\sigma_{\mathrm{T}}m_e c^3 \epsilon_0 & \text{Thompson regime} \\ \frac{3}{8}\sigma_{\mathrm{T}}m_e c^3 \frac{n_{\mathrm{ph}}}{\epsilon_0}\left[\ln\left(4\epsilon_0\gamma\right) - \frac{11}{6}\right] & \text{Klein} - \text{Nishina regime} \end{cases} \tag{1.31}$$

1.2.5 *pp* collisions

Protons can travel long distances and carry important information about the regions they pass through during their trip or about the place where they were accelerated. Protons

accelerated up to relativistic energies can interact with the surrounding matter and decay through different channels producing neutral and charged pions:

$$
\begin{aligned}
p + p &\rightarrow p + p + a\pi^0 + b(\pi^+ + \pi^-) \\
p + p &\rightarrow p + n + \pi^+ + a\pi^0 + b(\pi^+ + \pi^-) \\
p + p &\rightarrow n + n + 2\pi^+ + a\pi^0 + b(\pi^+ + \pi^-)
\end{aligned}
$$

where a and b are integers. The produced pions decay into other particles, depending on their electric charge: charged pions decay into muons that in turn can produce electron-positron pairs and neutrinos. These secondary pairs can contribute to the observed spectrum through the processes reviewed above (synchrotron, IC and relativistic Bremsstrahlung). Neutral pions are, however, the main channel of conversion of proton kinetic energy into gamma rays. For this channel to work, protons need to carry a kinetic energy above a certain threshold $E_{th} = 2m_\pi c^2(1 + m_\pi/4m_p) \approx 280$ MeV. The spectrum of the emitted radiation from neutral pion decay peaks at $\epsilon = 67.5$ MeV. If neutral pions are injected with an emissivity $q_\pi(\gamma_\pi)$, then the emissivity of the gamma rays produced during their decay is

$$
q_\gamma(\epsilon) = 2 \int_{\gamma_\pi^{min}} \frac{q_\pi(\gamma_\pi)}{\sqrt{\gamma_\pi^2 - 1}} \mathrm{d}\gamma_\pi \tag{1.32}
$$

where $\gamma_\pi^{min}(\epsilon) = \epsilon + m_\pi^2 c^4/4\epsilon$. The pion emissivity is given by (using the approximation from Aharonian & Atoyan (2000))

$$
q_\pi(\gamma_\pi) = cn_p \int N_p(\gamma_p)\delta(\gamma_\pi - kE_{kin})\sigma_{pp}(\gamma_p)\mathrm{d}\gamma_p \tag{1.33}
$$

being σ_{pp} the total cross section for the production of a π^0 with energy Lorentz factor γ_π by a proton of energy Lorentz factor γ_p in a pp interaction, and n_p is the number density of target protons. k is the fraction of the proton's kinetic energy ($E_{kin} = m_p c^2(\gamma_p - 1)$) which is given to the leading neutral pion. It is known from experiments that for a wide range of energies, above the GeV, $k \sim 0.17$. The total cross section can be derived as

$$
\sigma_{pp}(\gamma_p) = 30 \left[0.95 + 0.06 \ln\left(\frac{E_{kin}}{GeV}\right)\right] \tag{1.34}
$$

Taking into account the inelasticity coefficient (Aharonian & Atoyan 1996) the losses for this interaction can be derived from the cross section given above

$$
-\left(\frac{\mathrm{d}\gamma_p}{\mathrm{d}t}\right) = 4.5 \times 10^{-16} N_p \left[0.95 + 0.06 \ln\left(\frac{\gamma_p}{1.1}\right)\right] \gamma \tag{1.35}
$$

1.2.6 Photoelectric absorption

The X-ray observations presented in this thesis were carried out in the 0.2-10 keV band. In this band it is important to take into account the effect of photoelectric absorption. This process consists in the absorption of a photon by an atom and the release of an electron. For this process to take place the incident photon must have an energy above the ionization energy of the electron shell that is going to loose the electron. The probability of the interaction is maximum for photon energies equal to the ionization energies of a given electron shell, and decreases as ϵ^{-3} for photon energies above the ionization energy.

The cross section of photoelectric absorption (σ_{ph}) depends on the energy of the photon (see Morrison & McCammon 1983). In the case of interstellar matter, the optical depth of the process may be expressed as

$$\tau_{ph} = \exp\left(\sigma_{ph}(\epsilon)n_{\mathrm{H}}\right) \tag{1.36}$$

where n_{H} is the neutral hydrogen column density over the line-of-sight. The effect of photoelectric absorption is of major importance for energies below $\sim$1 keV.

1.2.7 Coulombian losses

When a relativistic nucleus with charge Ze, mass m_{N} and energy $E = \gamma m_{\mathrm{N}}c^2$ travels within a medium, it ionizes the medium and thus, the nucleus loses energy. This loss of energy, per unit length, is given by the Bethe-Bloch formula (Lang 1999):

$$-\left(\frac{\mathrm{d}\gamma}{\mathrm{d}x}\right)_i = \frac{2\pi Z^2 e^4 n_e}{m_e \mathrm{v}^2}\left[\ln\left(\frac{2m_e\mathrm{v}^2\gamma^2 W_m}{I^2}\right) - 2\beta^2 + f\right] \tag{1.37}$$

where v is the nucleus velocity, $\beta = \mathrm{v}/c$, n_e is the free electron number density, I is the ionization energy and W_m is the maximum energy that the nucleus can give to a free electron. The factor f is a correction that takes into account effects affecting the effective density, such as the polarization of the medium.

For a non-relativistic nucleus traveling across the medium and ionizing it, the energy loss by Coulombian interactions is given by

$$-\left(\frac{\mathrm{d}\gamma}{\mathrm{d}x}\right)_i = 4.07 \times 10^{-31} n_e c\left[\ln\left(\gamma\right) - \ln(n_e) + \ln\left(\frac{m_e^3 c^4}{\hbar^2 e^2}\right) - 1\right] \tag{1.38}$$

The effect of this loss mechanism will be of special importance in Chapter 5 where we model the emission of a young stellar object and consider them when solving the transport equation.

1.3 Particle acceleration

The relativistic particles that produce the emission described in the previous sections, cannot be accelerated by means of thermal mechanisms. Hence, the acceleration of particles to energies above 1 MeV must be explained by a mechanism that may be able to accelerate them beyond the thermal tail.

The systems studied throughout this thesis involve the presence of shocks. Shocks can be created by the collision of the relativistic wind of a pulsar with the strong wind of a massive star, or by the interaction of the jet of a MYSO with the parent molecular cloud. In all these scenarios, the shock propagates into the medium and particles can be accelerated by means of the *Fermi first order mechanism* or *diffussive shock acceleration* (DSA). Particles with high velocities travel from upstream (unshocked medium) to donwstream (shocked medium) regions, and eventually cross the shock and diffuse to the shocked region. The rate at which particles may be lost downstream of the shock is

$$r_{\rm loss} = nV_{\rm S}/R \ {\rm m}^{-2}{\rm s}^{-1} \tag{1.39}$$

where n is the number density of the accelerated particles, $V_{\rm S}$ is the velocity of the shock as seen from the upstream region, and R is the compression ratio of the shock. Assuming an isotropic distribution of particles upstream of the shock with velocity v, the rate at which they cross from upstream to downstream is

$$r_{\rm cross} \simeq nv/4 \ \ {\rm m}^{-2}{\rm s}^{-1}. \tag{1.40}$$

Once in the shocked region, these particles can diffuse back into the unshocked region by interacting with the magnetic field present in the medium. In this interaction, the particle may gain a certain amount of kinetic energy. This process can occur several times, and in each crossing the particle gains energy, until it reaches the relativistic limit. For relativistic particles the gain in energy can be approximated by

$$\frac{\Delta E}{E} \simeq \frac{4}{3} \frac{(R-1)}{R} \frac{V_{\rm S}}{c} \tag{1.41}$$

where $V_{\rm S}$ is the velocity of the shock.

There is a certain probability for the particles with velocity v in the reference frame where the surface of discontinuity is at rest, to escape from the region after one crossing

$$P_{\rm escape} = r_{\rm loss}/r_{\rm cross} \simeq 4V_{\rm S}/Rv \tag{1.42}$$

The probability of returning back upstream after crossing to the downstream region is

$$P_{\rm return} = 1 - P_{\rm escape} \tag{1.43}$$

Hence the probability of crossing the shock m times is $P_{\mathrm{cross}\geq\mathrm{m}} = (1 - P_{\mathrm{escape}})^m$. The energy of the particle after m crossings will be

$$E = E_0 \left(1 + \frac{\Delta E}{E} \right)^m \tag{1.44}$$

where E_0 is the initial particle energy.

The number of particles with energy greater than E will be a powerlaw distribution $Q(\geq E) \propto (1 - P_{\mathrm{escape}})^m$, where now $m = \ln(E/E_0)/\ln(1 + \Delta E/E)$. After some manipulation of these expressions one arrives at the final expression for the spectrum of accelerated particles in the shock (see Protheroe 1999 for details on the mathematical treatment)

$$Q(\geq E) \propto E^{-(\Gamma - 1)} \quad \text{(integral form)}$$
$$Q(E) \propto E^{-\Gamma} \quad \text{(differential form)}$$

where $\Gamma = (R + 2)/(R - 1)$. For strong shocks $R = 4$ and thus $\Gamma = 2$.

Part I

Young Stellar Objects

2
Introduction

2.1 Star-forming regions

The disk of the Milky Way is populated with large amounts of gas clouds. The chemical composition of these clouds consists mainly of hydrogen in its molecular form, H_2, thus the clouds are called molecular clouds. Heavier elements are also present due to the enrichment of the medium by the stars that have gone beyond the main sequence. The typical densities of molecular clouds range between $10^{-2} - 10^6$ cm^{-3} and the temperature is usually of a few tens of K.

Eventually, the hydrostatic equilibrium of the molecular cloud is perturbed (by a supernova explosion, for instance) and the gravitational force is no more balanced with the gas pressure. This perturbation might trigger the collapse of the most dense regions giving birth to protostars and finally, to new stars.

As the protostar continues accreting matter from the progenitor cloud, the core is heated by the gravitational contraction and the potential energy is released in the form of radiation. The core will collapse isothermally until it is not able to cool down efficiently. The process makes the cloud optically thick to its own radiation and the excess of radiation generated by the contraction cannot be released anymore. The temperature increases up to ~ 2000 K and the H_2 molecule is dissociated. The dissociation absorbs the excess of energy present in the protostellar core, the cloud becomes optically thin again and the contraction can go on until all the H_2 is dissociated. At this point, the dust starts to radiate in the infrared. This radiation escapes from the system due to the low opacity. Depending on the availability of gas and on the total mass of the molecular cloud, this will form high-mass or low-mass stars.

Figure 2.1: Hubble Space Telescope image of the Carina Nebula. Opaque dust and gas clouds are seen as well as two bipolar jets driven by two YSOs.

2.2 High energy emission from star-forming regions

2.2.1 High-mass protostars

Massive young stellar objects (MYSOs) have been suggested to be gamma-ray sources in the last years (Araudo et al. 2007; Romero 2008; Bosch-Ramon et al. 2010). Massive stars are formed in dense cores of cold clouds. The processes which takes place during the formation of the star are mostly unknown. There are two main scenarios that are thought to be at work in the massive star-formation: the monolitic accretion onto a massive protostar, and the coalescence of several low-mass protostellar cores becoming one high-mass protostar.

The first one, is an upscaled version of the main paradigm for low-mass star formation, but trying to solve the problem of the radiation pressure that would halt the infall of matter onto the protostar. Some theoretical works solve this problem by the formation of a cavity due to a jet and a wider outflow. The radiation would then be able to escape and the infall of mass would be able to go on. The jets and outflows observed in several MYSOs (Rodríguez et al. 1989; Martí et al. 1993; Garay et al. 2003) support this scenario.

The second scenario is based on the fact that massive stars are mostly formed in clusters. The coalescence will require high protostellar densities and the most massive protostars to be located at the center of the cluster. Then a massive protostar would be able to merge with some low-mass protostellar objects and increase its mass beyond the limit permitted by the monolitic accretion.

Figure 2.2: Sketch of a MYSO jet interacting with the surrounding medium (from Bosch-Ramon et al. (2010)).

It is clear, however, that the formation of massive stars involves outflows (Garay & Lizano 1999; Reipurth & Bally 2001). The accumulation of material around the core of the cloud would generate a massive protostar which starts to accrete material from the environment. The accretion is expected to have angular momentum leading to the formation of an accretion disk. The rotation would twist the strong magnetic fields present in the progenitor cloud around the disk, where a magnetic tower can be formed giving rise to collimated outflows or jets, as simulations predict (Banerjee & Pudritz 2006, 2007). The observational evidence for the existence of outflows comes from methanol masers and from the direct detection of thermal radio jets. These jets propagate along distances of a fraction of a parsec (Martí et al. 1993). At the jet termination region, interaction with the external medium creates two shocks: a bow shock moving in the interstellar medium (ISM), and a reverse shock in the jet. These shocks can accelerate particles that, in turn, can produce gamma rays trough inverse Compton (IC) scattering of infrared (IR) photons, relativistic Bremsstrahlung, or inellastic proton-proton collisions, if protons are accelerated as well (see Figure 2.2). In some cases non-thermal radio lobes and jets have been observed, indicating the presence of relativistic electrons that produce synchrotron radiation (Garay et al. 2003; Carrasco-González et al. 2010; López-Santiago et al. 2013).

2.2.2 Low-mass protostars

The case of low-mass protostars emitting at high energies has also been addressed in the last years (del Valle et al. 2011). In this case, the high-energy emission is not produced by shocks at the jet-end, but by magnetic reconnection events near the protostar surface. The kind of sources that can lead to this processes are T-Tauri stars. These are low-mass protostars ($M < 3M_\odot$), with spectral types K–M and $T_{\text{eff}} \sim 3000 - 5000$ K (Montmerle &

André 1989). T-Tauri stars drive strong winds with mass-loss rates $\dot{M} \sim 10^{-8} M_\odot$ year^{-1} and velocity ~ 200 km s^{-1} (Feigelson & Montmerle 1999). At X-rays these protostars are found to be variable sources displaying intense flares in the keV band. Their luminosities can be as high as $10^{31} - 10^{33}$ erg s^{-1}. These flares are thought to occur in magnetic tubes, as upscaled versions of solar flares, and can last as long as $10^3 - 10^4$ s. The temperature of the emitting plasma can reach up to 10^8 K (Tsuboi et al. 1998). Magnetic reconnection is an important process that allows the release of energy from the system. It consists in a topological reconfiguration of the magnetic field by changes in the connectivity of the field lines. When this happens, the system releases large amounts of magnetic energy. The ejected plasma can be shocked then and the acceleration of particles up to relativistic energies can occur through the Fermi mechanism.
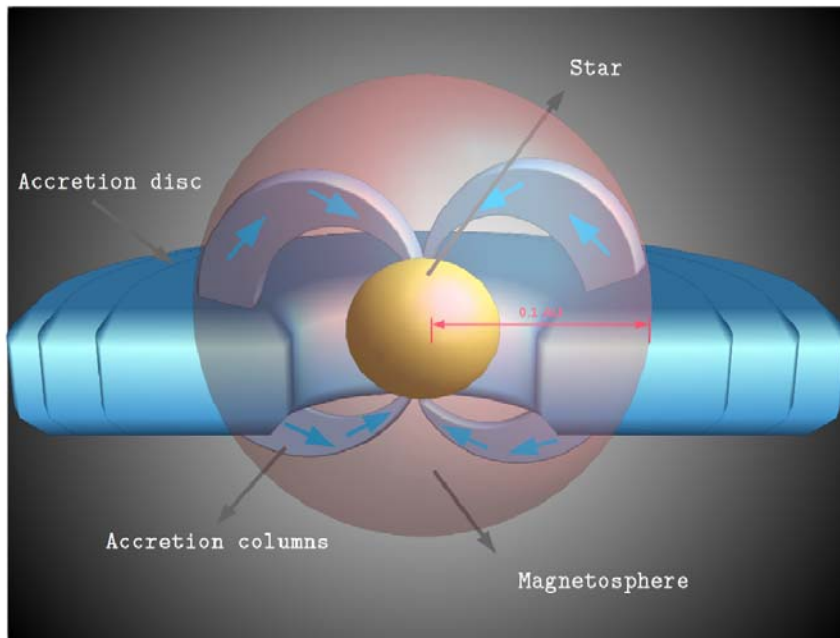
Figure 2.3: Sketch of a T-Tauri star from Feigelson & Montmerle (1999).

2.2.3 Other high-energy emitting sources

Other possible scenarios have been suggested for the gamma-ray production involving young stars, such as the case of the massive stars with strong winds. In this scenario, gamma-rays could be produced by the interaction between the supersonic winds and the ISM. The terminal shock can accelerate particles and ions up to high energies which might interact with the ambient matter producing gamma-rays. Whereas the luminosity produced by a single massive star wind should be low, collective effects might be important

(Torres et al. 2004).

Gamma-rays can also be produced in the wind interaction region of a binary of two massive stars (Benaglia & Romero 2003). In this case, the acceleration region is located between the two components of the binary system and is exposed to strong photon fields where IC cooling of the electrons can generate a significant amount of HE non-thermal emission. A source of this class, η-Carinae, has been detected at $E > 100$ MeV by *AGILE* (Tavani et al. 2009).

Of-type stars have strong winds with velocities larger than the escape velocity, which implies an important mass-loss rate ($10^{-6} - 10^{-5}$ M$_\odot$ yr^{-1}). The action of this wind in the interstellar medium can create hot gas bubbles with expanding boundaries of swept-up material, which might produce gamma rays in a similar way as in the case of WR stars. The case of gamma-ray emission in Of-type stars has been discussed in the past, e.g. by Voelk & Forman (1982). The predicted luminosity, however, is still below the current sensitivity of gamma-ray instruments.

Finally, OB associations are tracers of a number of galactic objects that can produce gamma rays, such as neutron stars, massive stars with strong winds, YSOs, etc. They are also thought to be places where acceleration of a significant fraction of galactic cosmic rays (CRs) might occur (e.g. Binns et al. 2008).

The aim of the first part of this thesis is to find evidence supporting the presence of HE emission coming from massive YSOs, amongst other young galactic sources. We address this goal by studying the spatial coincidences between *Fermi*/LAT sources and catalogs of young objects (YSOs, WR stars, Of-type stars and OB associations). We calculate the probability of chance coincidences by using Monte Carlo simulations (see Chapter 3). Besides, we have studied individual sources that might be non-thermal high-energy emitters, such as the cases of the star-forming region Monoceros R2 (see Chapter 4) and IRAS 16547-4247 (see Chapter 5), by analyzing archival data and modelling its emission.

3

Exploring the association of *Fermi* sources with young galactic objects

3.1 Introduction

Massive protostars have associated bipolar outflows which can produce strong shocks when interact with the surrounding medium. At these shocks particle acceleration up to relativistic energies can occur. Relativistic electrons and protons can then produce gamma-ray emission, as some theoretical models predict.

In this chapter we try to find evidence supporting the presence of HE emission coming from massive YSOs and other young galactic sources[1]. To attain this goal we study the spatial coincidence between gamma-ray sources detected by *Fermi* and samples of young objects, such as YSOs, WR stars, Of-type stars and OB associations. We also estimate the probability of chance coincidences by using Monte Carlo simulations and we provide a list of counterpart candidates of the gamma-ray sources.

3.2 Cross-correlation of the First Fermi Catalog with massive young galactic objects

There is not observational evidence for a YSO emitting gamma-rays so far. The *Fermi* satellite with its unprecedented sensitivity in the GeV domain allows us to explore the SFRs to search for gamma-ray emitters. In order to identify those young objects that

---

[1]Published in Munar-Adrover, P., Paredes, J.M., Romero, G.E., 2011, A&A, 530, A72.

might be emitting gamma rays, we have taken first the First *Fermi* Catalog (Abdo et al. 2010) by the *Fermi* Collaboration and excluded all known firm identifications, getting a list of 1392 sources. Then we have crossed this list with catalogs of confirmed and well characterized YSO's and other type of young stars. We have also made a Monte Carlo study to determine the probability of pure chance coincidences between the crossed catalogs.

3.2.1   Catalogs

The catalogs used in this study are listed in Table 3.1. Here we describe in more detail each one.

- The *Fermi Large Area Telescope* First Catalog (Abdo et al. 2010) contains the detected sources during the first 11 months of the science phase of the mission, which began on 2008 August 4. This catalog contains 1451 gamma-ray sources detected and characterized in the 100 MeV to 100 GeV range with a typical position uncertainty of $\sim 6'$. Excluding the firm identifications from the original sample we get 1392 sources. Most of them are located on the galactic plane (see Figure 3.1).
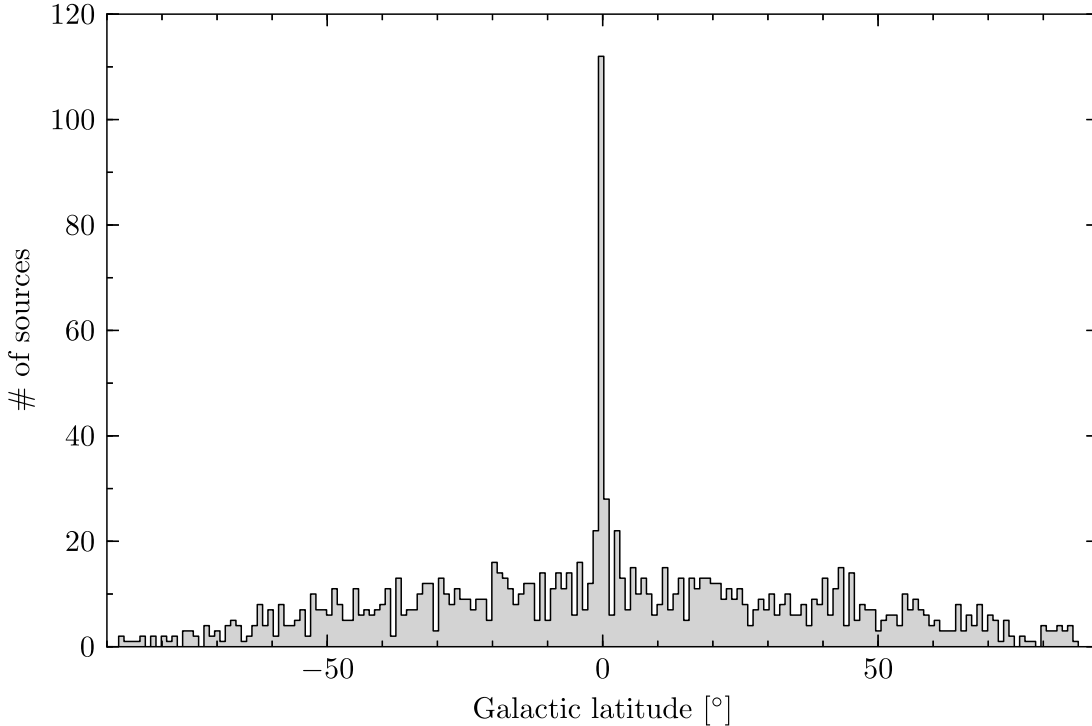

Figure 3.1: Distribution of unidentified First *Fermi* Catalog sources in galactic latitude.

- The Red *MSX* Source (RMS) survey is an ongoing multi-wavelength (from radio to infrared) observational program with the objective of providing a well-selected sample of MYSOs in the entire Galaxy (Urquhart et al. 2008). About $\sim$2000 MYSO candidates have been identified by comparing the colours of *MSX* and 2MASS point sources (at 8, 12, 14 and 23 μm) with those of well known MYSOs. The survey also uses high resolution radio continuum observations at 6 cm obtained with the VLA in the northern hemisphere, and at 3.6 cm and 6 cm with ATCA in the southern hemisphere, that help to distinguish between genuine MYSOs and other types of objects, such as ultra compact HII regions, evolved stars or planetary nebulae, that contaminate the sample. In addition to these targeted observations, archival data of previous VLA survey of the inner Galaxy has been used. This ongoing program has provided a sample of 637 well-identified MYSOs which have been used in our work.

- The VIIth catalog of Population I WR stars (van der Hucht 2001) contains 227 stars, with spectral types and *bv* photometry. In recent years, the number of WR stars has increased in 71 new stars, respect to the VIth catalog and also the coordinates have been improved. The position uncertainty is of the order of a fraction of an arcsecond.

- The catalog of Of-type stars is the one of Cruz-González et al. (1974), which contains 664 stars. The catalog provides for each source m_v, B–V, spectral type, radial velocity, radial component of the peculiar velocity, possible multiplicity of the object, and other characteristics. The typical uncertainty in the star position is $\sim 1'$.

- Finally, the catalog of OB associations is the one of Mel'Nik & Efremov (1995). This catalog contains 88 associations and provides distances to the association, number of stars and size of the association along the galactic latitude and longitude axes. The typical value of the size is $\sim 20 - 30$ pc.

3.2.2 Spatial coincidences

We have crossed the *Fermi* catalog with the catalogs of young galactic objects mentioned above. We calculate the distance between two sources using the statistical parameter S (Allington-Smith et al. 1982):

$$S = \sqrt{\frac{(\Delta\alpha \cos\delta)^2}{\sigma_{i_\alpha}^2 + \sigma_{j_\alpha}^2} + \frac{\Delta\delta^2}{\sigma_{i_\delta}^2 + \sigma_{j_\delta}^2}}$$

where $\Delta\alpha$ and $\Delta\delta$ are the difference between the right ascension and the declination of the two compared sources, respectivelly, σ_{a_b} is the uncertainty in the position of the source, and (i, j) represent the two sources, respectively. The error in the position of the *Fermi* sources is taken as the 95% confidence ellipse. The error in the position of the other compared

Object type	Catalog	# of sources
γ-ray sources	First *Fermi* Catalog[a]	1392[f]
YSO	RMS Survey[b]	637
WR	VIIth Catalog of Galactic Wolf-Rayet stars[c]	227
Of-type	A catalog of galactic O stars and the ionization of the low density interstellar medium by runaway stars [d]	664
OB associations	A new list of OB associations in our Galaxy[e]	88

Table 3.1: List of the catalogs used in the study. [a]Abdo et al. (2010), [b]Urquhart et al. (2008), [c]van der Hucht (2001),[d]Cruz-González et al. (1974), [e]Mel'Nik & Efremov (1995); [f]number of gamma-ray sources after excluding the firm identifications.

sources is the precision in the coordinates, for YSOs, WR stars and Of-type stars, and the angular size of the association in the case of OB associations. If S is lower or equal to the unit, it means that the source position (YSO, WR, Of-type or OB associations) is inside the 95% uncertainty ellipse of the *Fermi* source, within its own position uncertainty, and that case is considered as a coincidence. Massive YSO and protostar are point-like objects when compared with the confidence contours of *Fermi* sources. The same is valid for WR and Of star, either in binary systems or isolated. Only OB association are large systems that can contain more than a single gamma-ray source. We note that our study is based on two-dimensional coincidences, since we are comparing the equatorial coordinates of the sources.

3.2.3 Monte Carlo analysis

To determine the chance coincidences we have used the Monte Carlo method for simulating sets of synthetic gamma-ray sources starting from the *Fermi* Large Area Telescope First Catalog. We have followed a similar criteria to that used by Romero et al. (1999) to search for the possible association of unidentified *EGRET* sources with other type of celestial objects. In this algorithm, the galactic coordinates of a gamma-ray source (l, b) are moved to new ones (l', b'). The new galactic longitude coordinate is calculated by doing $l' = l + R_1 \times 360°$, where R_1 is a random number between 0 and 1 that never repeats neither from source to source nor from set to set. Since the distribution of *Fermi* sources is almost constant in galactic longitude, we do not impose any constraint to this coordinate in the simulations. The sources in the *Fermi* catalog have a certain distribution in galactic latitude (see Figure 3.1). In order to constrain the simulations with this distribution, the galactic latitude coordinate is calculated by doing $b' = b + R_2 \times 1°$ where again R_2 is a random number between 0 and 1. Here, if the integer part of b' is greater than the integer

part of b or the sign of b' is different than the sign of b, then b' is replaced by $b' - 1°$.

We have simulated 1500 sets of synthetic *Fermi* sources and each set has been compared with a fix set of different kind of objects: YSOs, WR stars, Of-type and OB associations. In each simulation, we calculate the distance between the two sources using the statistical parameter S.

For each kind of compared objects we have calculated the average number of coincidences and its standard deviation after all Monte Carlo simulations. We have calculated the chance coincidence probability using the actual number of coincidences for each type of object and assuming a Gaussian distribution in the simulations. This probability allows to know the reliability of our study. We have repeated this process moving the *Fermi* sources in 2°-bins in galactic latitude also, i.e. replacing the galactic latitude coordinate by $b' = b + R_2 \times 2°$ and if the integer part of b' is greater than the integer part of b or the sign of b' is different than the sign of b, then b' is replaced by $b' - 2°$. This binning allows us to keep the initial distribution in galactic latitude as well.

Object type	Coincident γ-ray sources	Simulated $1° - bin$	Probability $1° - bin$	Simulated $2° - bin$	Probability $2° - bin$
YSO	12	4.4±2.0	1.8×10^{-4}	3.6±1.8	5.6×10^{-6}
WR	2	1.3±1.1	2.9×10^{-1}	1.2±1.1	2.9×10^{-1}
Of-type	5	2.9±1.7	1.1×10^{-1}	2.9±1.7	1.1×10^{-1}
OB assoc.	107	72.5±8.0	4.2×10^{-6}	72.8±8.0	5.5×10^{-6}

Table 3.2: Statistical results obtained from simulations. Latitude galactic coordinate has been constrained while galactic longitude remains free.

3.3   Results

The results from our statistical study are shown in Table 3.2. In this table we list, from left to right, the object type, the number of coincidences between the each compared catalog and the original *Fermi* catalog, the simulated average number of coincidences and the chance coincidence probability for each binning in galactic latitude. We find 12 gamma-ray sources spatially coincident with YSOs, 2 with WR stars, 5 with Of-type stars and 107 with OB associations.

From the Monte Carlo analysis we see that there is a strong correlation between gamma-ray sources and YSOs: the catalog cross-check returns 12 coincidences between gamma-ray sources and YSOs. The Monte Carlo simulations, for the case of displacing the *Fermi* sources in 1°-bins, returns an average of coincidences of 4.4±2.2 sources, which is the number of chance coincidences. This means that 7.6 of the 12 coincident *Fermi* sources ($\sim 63\%$ of the total coincidences with a $\sim 4\sigma$ confidence level) should be associated with a probability of chance coincidence of 1.8×10^{-4}. Similarly, in the case of displacing the

Fermi sources in 2°-bins, we obtain an average of coincidences of 3.6±1.8. That result indicates that 8.4 of the 12 coincident sources ($\sim 70\%$ of the total coincidences with a $\sim 5\sigma$ confidence level) should be associated with a probability of 5.6×10^{-6} of being chance coincidences. In a similar way, the association of *Fermi* sources with WR and Of-type stars is unclear since the number of actual coincidences and the results of the Monte Carlo simulations are too much similar and thus the probability of chance coincidence is too high (0.29 and 0.11 for WR stars and Of-type stars, respectively). Notice that the results for WR and Of-type stars are different from those obtained by Romero et al. (1999) for *EGRET* sources. The probability of chance coincidences has increased as the number of candidates decreased in the case of WR stars. In the case of Of-type stars the probability of chance association has increased as the number of coincidences increased as well. The probability of chance coincidence with OB associations is as low as $\sim 10^{-6}$. In this case, however, the nature of the gamma-ray emission is not clear, as it is commented in Subsection 3.3.3

3.3.1   Young stellar objects

The association of gamma-ray sources and massive YSOs has been suggested in the last years after studying a reasonable scenario for the production of non-thermal emission (Araudo et al. 2007). However, this is the first time that the study of YSOs as gamma-ray sources is carried out in a statistical way, taking advantage of the *Fermi* catalog.

The results of our cross-check, shown in Table 3.3, indicate that 12 gamma-ray sources are positionally coincident with 23 YSOs. In this table we present, from left to right, the *Fermi* source name, its J2000 equatorial coordinates, its positional uncertainty, the spectral γ-ray index, the energy flux (E>100 MeV), the YSO name, its J2000 equatorial coordinates, the angular distance between the two compared sources, the distance to the YSO, its IR luminosity and the mass of the star forming region where it is embedded.

In what follows we present a case by case discussion of the gamma-ray fields:

- 1FGL J0541.1+3542. This source is coincident with three YSOs: G173.6328+02.8604, G173.6339+02.8218 and G173.6882+02.7222. Their luminosities are below $4.8\times10^4 L_\odot$. The three objects belong to the G173.6036+02.6237 complex (in the RMS Survey notation), which is situated at a distance of 1.6 kpc. We also find two Herbig Haro like objects: GGD 5 and GGD 6 (Gyulbudaghian et al. 1978) within the error ellipse of the *Fermi* source. Outside the *Fermi* error box the complex also harbors three more YSOs and a HII region.

- 1FGL J0647.3+0031. The YSO G212.0641-00.7395 is the only coincidence with this source. Its kinematic distance is 6.4 kpc and it has a luminosity of $2.5\times10^4 L_\odot$. This source belongs to the G211.9800-00.9710 complex, together with another YSO that lies outside the error box of the gamma-ray source.

- 1FGL J1256.9−6337. We find G303.5990-00.6524 within the error ellipse of this gamma-ray source. It is a YSO with a bolometric luminosity of $8.3 \times 10^3 L_\odot$ and located at a kinematic distance of 11.3 kpc. It belongs to the G303.5670-00.6253 complex that also harbors a HII region.

- 1FGL J1315.0−6235. This source is coincident with G305.4840+00.2248 which is a YSO with a luminosity of $3.8 \times 10^3 L_\odot$ and located at a distance of 3.6 kpc.

- 1FGL J1651.5-4602. The source G339.8838-01.2588 is coincident with this gamma-ray source. It is a YSO with a bolometric luminosity of $2.1 \times 10^4 L_\odot$. It is located at 2.6 kpc from the Earth. This source has been detected in radio at 8.6 GHz with an integrated flux of 2.6 mJy (Walsh et al. 1998). There is no indication of whether the radio flux is non-thermal or not.

- 1FGL J1702.4−4147. This source is coincident with two YSOs: G344.4257+00451B and G344.4257+00451C, which form the G344.4120+00.0492 complex, together with two HII regions. They are located at 5 kpc from the Earth and both have a bolometric luminosity of $1.5 \times 10^4 L_\odot$. These gamma-ray source is also near to a cluster of stars (see Dutra et al. 2003) and a molecular cloud (see Russeil & Castets (2004)).

- 1FGL J1846.8−0233. We find a coincidence with the source G030.1981-00.1691. It has a bolometric luminosity of $2.9 \times 10^4 L_\odot$ and is located at 7.4 kpc. Within the error ellipse of the *Fermi* source there are several other sources, such as dark nebulae and HII regions.

- 1FGL J1848.1−0145. This source is coincident with two YSOs: G030.9726-00.1410 and G030.9959-00.0771, located at 5.7 kpc and with bolometric luminosities of $3.9 \times 10^3 L_\odot$ and $5.1 \times 10^3 L_\odot$, respectively. Both are part of the G031.1451+00.0383 complex, which hosts five more YSOs (outside the *Fermi* error box), five diffuse HII regions and ten HII regions. Within the error ellipse of the gamma-ray emission there is an unidentified very high energy gamma-ray source, HESS J1848-018 (Chaves et al. 2008), which is probably the most suitable very high energy candidate counterpart to the *Fermi* detection.

- 1FGL J1853.1+0032. This source has the biggest error ellipse ($\Delta\theta_{95\%} \sim 0.5°$). For that reason, there is a high number of sources within its location error box, including pulsars, supernova remnants and X-ray sources. The cross-match of the catalogs yields 6 coincidences. These 6 YSOs belong to 3 different complexes with different distance to the Earth: G032.8205-00.3300 and G033.3891+00.1989 belong to the G033.1844-00.0572 complex, located at 5.1 kpc. The luminosities of these two sources are 1.7 and 1.1 $\times 10^3 L_\odot$, respectivelly; G033.3933+00.0100 and G33.5237+00.0198 belong to the G033.6106+00.0464 complex, located at a distance of 6.8 kpc and the luminosity is $7.9 \times 10^3 L_\odot$ for both sources; G034.0126-00.2832 and G034.0500-00.2977

belong to the G034.0313-00.2904 complex. The distance to these objects is 13.3 kpc and their bolometric luminosities are $3.4\times10^4 L_\odot$ and $2.4\times10^4 L_\odot$, respectively.

- 1FGL J1925.0+1720. Two YSOs are coincident with it: G052.2025+00.7217A and G052.2078+00.6890. The bolometric luminosities are $1.5\times10^4 L_\odot$ and $2.0 \times10^4 L_\odot$, respectivelly. They belong to the G052.2052+00.7053 complex which is located at 10.2 kpc, and hosts also a HII region.

- 1FGL J1943.4+2340. There is spatial coincidence with the source G059.7831+00.0648, located at 2.2 kpc. It has a bolometric luminosity of $6.8\times10^4 L_\odot$. This YSO has been detected in radio at 8.6 GHz with an integrated flux of 1.0 mJy (Sridharan et al. 2002). The infrared counterpart of this YSO is IRAS 19410+2336. It was observed by Chandra in 2002, finding hard X-ray emission from a number of sources within this high-mass star forming region (Beuther et al. 2002a). The region has two cores where star formation takes place, with masses of 840 $M_\odot$ and 190 $M_\odot$ (Sridharan et al. 2002; Beuther et al. 2002b). In the latter paper, it is proposed that the X-ray emission is produced by magnetic reconnection effects between the protostars and their accretion disks. The interaction of several molecular outflows, where the YSO from the RMS survey is located, and the combined effects of the stellar winds, are a good scenario that might result in particle acceleration up to relativistic energies.

- 1FGL J2040.0+4157. There is spatial coincidence with G081.5168+00.1926. This YSO is located at 1.7 kpc and shows a bolometric luminosity of $7.04\times10^2 L_\odot$. There is a galaxy (2MASX J20395796+4159152) located at $2.3''$ from the position of that YSO.

Table 3.3: Positional coincidence of *Fermi* sources with MYSOs.

Fermi Name (1FGL)	RA (°)	Dec (°)	95% Semi Major Axis (°)	Spectral Index Γ ($F \propto E^{-\Gamma}$)	Flux(E≥100 MeV) $\times 10^{-11}$ erg cm^{-2} s^{-1}	MSX Name	RA (°)	Dec (°)	Δθ (°)	Distance* (kpc)	L_{bol}* ($\times 10^3 L_\odot$)	Mass ($M_\odot$)
J0541.1+3542	85.2805	35.7091	0.1397	2.41±0.13	1.6±0.5	G173.6328+02.8064	85.27929	+35.82633	0.12	1.6[a]	4.8[d]	
						G173.6339+02.8218	85.29592	+35.83380	0.13	1.6[a]	3.2[e]	
						G173.6882+02.7222	85.22758	+35.73558	0.05	1.6[a]	–	
J0647.3+0031	101.8417	0.5289	0.2150	2.41±0.11	1.9±0.5	G212.0641−00.7395	101.80567	+00.43514	0.10	6.4[b]	25[f]	
J1256.9−6337	194.2474	−63.6212	0.1955	2.26±0.12	4.9±1.1	G303.5990−00.6524	194.35546	−63.51650	0.12	11.3[b]	8.3[f]	
J1315.0−6235	198.7635	−62.5971	0.1860	2.31±0.12	6.9±0.0	G305.4840+00.2248	198.40016	−62.53708	0.18	3.6[b]	3.8[f]	
J1651.5−4602	252.8831	−46.0340	0.2258	2.21±0.07	13.9±3.4	G339.8838−01.2588[1]	253.01942	−46.14267	0.14	2.6[b]	21.0[f]	
J1702.4−4147	255.6039	−41.7859	0.0800	2.39±0.07	8.7±2.0	G344.4257+00.0451B	255.53674	−41.78303	0.05	5.0[b]	15.0[f]	
						G344.4257+00.0451C	255.53587	−41.78617	0.05	5.0[b]	15.0[f]	
J1846.8−0233	281.7001	−2.5628	0.1262	2.21±0.06	9.3±2.3	G030.1981−00.1691	281.76274	−2.51003	0.08	7.4[b]	29.0[f]	
J1848.1−0145	282.0470	−1.7605	0.0859	2.23±0.04	9.5±3.2	G030.9726−00.1410	282.09178	−1.80842	0.07	5.7[b]	3.9[f]	1.9×10^{3g}
						G030.9959−00.0771	282.04516	−1,75808	0.0044	5.7[b]	5.1[f]	1.9×10^{3g}
J1853.1+0032	283.2884	0.5366	0.5207	2.18±0.07	5.7±1.7	G032.8205−00.3300	282.04436	−1.75703	0.34	5.1[b]	17.0[f]	
						G033.3891+00.1989	282.89092	+0.49750	0.40	5.1[b]	11.0[f]	
						G033.3933+00.0100	283.06109	+0.41528	0.26	6.8[b]	7.9[e]	
						G033.5237+00.0198	283.11179	+0.53569	0.34	6.8[b]	7.9[e]	
						G034.0126−00.2832	283.60437	+0.83239	0.43	13.3[b]	34.0[f]	
						G034.0500−00.2977	283.63454	+0.85914	0.47	13.3[b]	24.0[f]	
J1925.0+1720	291.2748	17.3485	0.1443	2.28±0.12	2.4±1.0	G052.2025+00.7217A	291.24933	+17.42169	0.08	10.2[b]	15.0[f]	
						G052.2078+00.6890	291.28553	+17.41317	0.07	10.2[b]	20.0[f]	
J1943.4+2340	295.8667	23.6815	0.1118	2.23±0.11	2.6±0.7	G059.7831+00.0648[2,3]	295.79680	+23.73433	0.08	2.2[a]	6.8[f]	840-190[h]
J2040.0+4157	310.0154	41.9533	0.1970	2.66±0.06	7.9±1.2	G081.5168+00.1926	309.99066	+41.98739	0.04	1.7[c]	0.704[f]	

[1]Detected in radio at 8.6 GHz with integrated flux of 2.6 mJy; [2]Detected in radio at 8.6 GHz with integrated flux of 1.0 mJy. [3]Observed in the X-ray with *Chandra* (Beuther et al. 2002a); Distances: [a]distance to the complex, taken from the literature, [b]kinematic distance determined from the systemic velocity of the complex,[c]distance has been taken from the literature. Luminosities: [d]*IRAS* fluxes, [e]*MSX* fluxes, [e]*MSX* 21 μm band flux using a scaling relationship determined from a comparison with sources where spectral energy distribution (SED) fits have been possible. [f]SED fit to the available infrared fluxes (*2MASS, MSX, MIPSGAL/IGA*) and literature (sub)millimetre fluxes. [*]data obtained from http : //www.ast.leeds.ac.uk/cgi − bin/RMS/RMS.DATABASE.cgi. Masses: [g]from Ragan et al. (2006), [h]mass of the 2 cores identified in Beuther et al. (2002b)

3.3.2 WR and Of-type stars

We have found two *Fermi* sources coincident with 15 WR stars in the Galactic Centre Cluster and 9 WR stars in the Quintuplet Cluster. Some of these stars (see van der Hucht 2006) show variability and have been detected at X-rays with evidence of non-thermal emission. The results of our study are shown in Table 3.4. We cannot state that these two coincidences correspond to physical associations given the high chance association probability obtained from the Monte Carlo study. The first one is in the direction of the galactic centre, and there are several other sources that introduce confusion. The second one was suggested as potential association with the Pistol Star in Abdo et al. (2010) and it is situated in a very crowded field.

In the case of Of-type stars, which are the evolved state of O stars, and precursors of WR stars, our results show that five *Fermi* sources are coincident with 5 stars (see Table 3.5). The probability of chance coincidence is too high to state a physical association. The sources 1FGL J1315.0-6235 and 1FGL J1853.1+0032 show also positional coincidence with YSOs (see Table 3.3). The case of association with YSOs has a much lower value for the chance probability. The source 1FGL J1112.1-6041 is coincident with HD 97434, a multiple star system. 1FGL J1315.0-6235 is located in a regions that harbors dark nebulae and molecular clouds. The Of star coincident with this source is HD 115071 which is a spectroscopic binary. Finally, 1FGL J2004.7+3343 is coincident with HD 227465 and there is also the source G70.7+1.2 inside the error box of the *Fermi* detection, which might contain a Be star and an X-ray-emitting B star pulsar binary (Cameron & Kulkarni 2007).

Fermi Name (1FGL)	RA (°)	Dec (°)	95% Semi Major Axis (°)	Γ ($F \propto E^{-\Gamma}$)	Flux(E>100 MeV) $\times 10^{-10}$ erg cm^{-2} s^{-1}	Star	RA (°)	Dec (°)	Δθ (°)	Distance (kpc)
J1745.6-2900	266.420	−29.014	0.019	2.26±0.03	7.1±0.7	WR 101a[1]	266.41454	−29.00950	0.01	8.0
J1746.4-2849	266.618	−28.818	0.10	2.2±0.5	4.6±0.0	WR 102c[2]	266.54667	−28.81822	0.06	8.0

[1]WR stars 101 b, c, d, e, f, g, h, i, j, k, l, m, n, o, belonging to the Galactic Center Cluster lie at distances less than 20″ and are also within the error box of the gamma-ray source; [2]WR stars 102 d, e, f, g, h, i, j, k belonging to the Quintuplet Cluster lie at distances less than 1′ and are also coincident with the gamma-ray source.

Table 3.4: Positional coincidence of *Fermi* sources with WR stars.

Fermi Name (1FGL)	RA (°)	Dec (°)	95% Semi Major Axis (°)	Γ ($F \propto E^{-\Gamma}$)	Flux(E>100 MeV) $\times 10^{-12}$ erg cm^{-2} s^{-1}	Star	RA (°)	Dec (°)	Δθ (°)	Distance[1] (kpc)
J0005.1+6829	1.2841	68.4883	0.4427	2.58±0.12	1.7±0.5	BD+67 1598	1.225	68.167	0.32	1.07
J1112.1-6041	168.0486	−60.6929	0.0461	2.12±0.05	14.1±1.6	HD 97434	167.975	−60.683	0.04	2.67
J1315.0-6235	198.7644	−62.5971	0.1860	2.31±0.12	6.9±0.0	HD 115071	199.000	−62.583	0.11	0.74
J1853.1+0032	283.2887	0.5369	0.5207	2.18±0.07	5.7±1.7	BD-0 3584	283.400	0.567	0.12	2.18
J2004.7+3343	301.1855	33.7171	0.1320	2.28±0.08	5.2±0.8	HD 227465	301.125	33.700	0.05	3.48

[1]distances from Cruz-González et al. (1974)

Table 3.5: Positional coincidence of *Fermi* sources with Of stars.

3.3.3   OB associations

Our study yields 107 *Fermi* sources positionally coincident with 35 OB associations, which represents ∼ 41% of the sample. We list the results in Table C.1 in Appendix C. We get this large number of gamma-ray sources due to the size of the OB associations. Most of them have angular sizes of the order of ∼ 1° in diameter or higher. Our results extend those of Romero et al. (1999), where they found 26 coincidences between *EGRET* sources and OB associations. Most of the OB associations that they found are present in our results, plus other new candidates, as expected from the higher sensitivity of *LAT*. Although the number of sources has increased, the probability of chance associations is approximately the same as in Romero et al. (1999).

Most of the OB associations have less than 5 *Fermi* sources within their error boxes. There are 7 OB associations with 5 or more *Fermi* sources within their error boxes. There are 4 associations with a number of gamma-ray coincidences between 5 and 10 (Ori 1 B, Ori 1 C, Car 2, and Cyg 1,8,9), located at short distances from the Earth (less than 1 kpc) and located at galactic latitudes of ∼ |15°| (association centroid position). There is an exception, Car 2, which is located at 2.2 kpc and has a galactic latitude of −0.13°. The OB associations with the major number of gamma-ray coincidences (> 10) are those from Scorpius (Sco 2 A, Sco 2 B and Sco 2 D). Those associations are located at ∼ 170 pc on average and have very important angular sizes (∼ 9.5° on average).

There are five *Fermi* sources that are coincident with OB associations and YSOs at the same time: 1FGL J1256.9-6337, 1FGL J1315.5-6235, 1FGL J1702.4-447, 1FGL J1943.4+2340 and 1FGL J2040.0+4157. In all cases the OB association overlaps both the *Fermi* source and the YSO. In all cases but one, however, the distances to the YSO and the OB association are too much different.

3.4   Discussion

The fact that there are five *Fermi* sources coincident with both YSOs and OB associations makes us consider which is the chance probability of having coincidence of *Fermi* sources with YSOs alone. Using the Monte Carlo algorithm again, but taking into account this constrain, we obtain a mean value of coincidences of 2.8 ± 1.7 and the chance probability for the seven *Fermi* sources coincident only with YSOs is ∼ 1.6%.

The brightest IR YSOs have more molecular mass available for proton-proton collisions and Bremsstrahlung interactions than those that are faint. It is expected then that the brightest IR YSOs would show the highest gamma-ray luminosity. To test such a trend, we have plotted in Figure 3.2 the IR luminosity versus the gamma-ray luminosity of the brightest YSOs coincident with each *Fermi* source. The gamma-ray luminosity has been calculated from the gamma-ray flux (see Table 3.3) assuming that the distance to the gamma-ray source is equal to the distance to the corresponding YSO. We see that under this assumption, there is a trend of increasing the gamma-ray luminosity as the IR
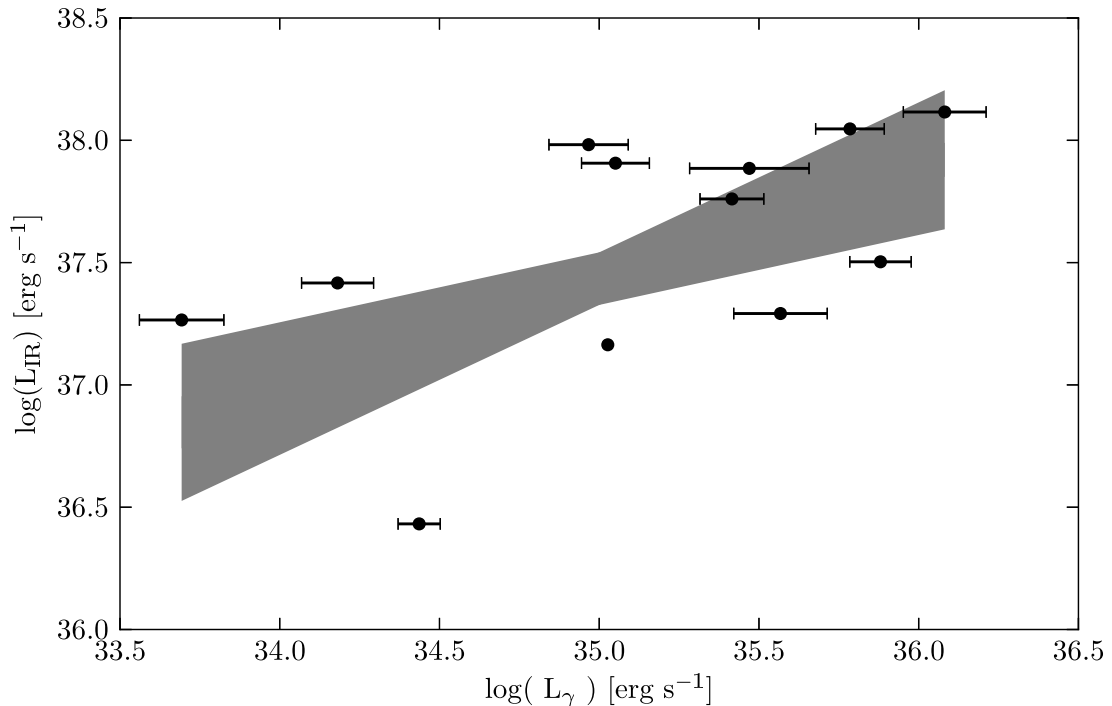
Figure 3.2: IR luminosity versus gamma-ray luminosity above 100 MeV of the brightest YSOs coincident with each *Fermi* source. The shaded area represents the 1-σ confidence interval of a least squares fit taking 1000 samples of 8 randomly selected points each. It can be roughly seen that the higher the gamma-ray luminosity the higher the IR luminosity.

luminosity increases too. This trend, however, is obtained using the whole data set, and according to the results from our Monte Carlo simulations we should have four chance coincidences out of the 12 candidates. To see how this could affect the trend, we have selected eight data points randomly and fitted them to a straight line by least squares. We have repeated this process one thousand times, getting an average least square fit within one standard deviation. The limits of this fit are plotted as the gray area in Figure 3.2. The increasing trend in the data is clearly visible, although with a significant dispersion. This is not surprising taking into account the broad approach.

The association of WR stars with gamma-ray sources has been discussed in the past by Kaul & Mitra (1997) and Romero et al. (1999). In both cases, the authors studied the positional coincidence between WR stars and unidentified EGRET sources. In the latter work, they found that two WR stars are of special interest: WR 140 and WR 142. The first one is a binary system, composed by a WC 7 plus an O4-5 star where the region of collision of the winds seems to be a good place for particle acceleration and high energy emission. It should be mentioned, however, that WR 140 is a long period binary with variability expected on time scales of years (Williams et al. 1987). In the second one,

WR 142, the hard X-ray emission and fast wind may indicate a colliding wind shock that could be explained by a companion close to this star (Sokal et al. 2010). None companion, however, has been reported so far. In our work none of these mentioned WR stars appear to be coincident with any *Fermi* source. The poor statistical correlations found from the simulations does not allow us to be confident with any of the coincidences found.

The case of Of-type stars is also unclear since the probability of chance association is high.

Finally, our results for the OB associations are not conclusive. The probability of chance coincidence is negligible ($\sim 10^{-6}$), but we get several gamma-ray sources for each OB association. Thus, is very difficult to assign a specific counterpart to the gamma-ray emission.

3.5 Conclusions

We have studied the two dimensional coincidence between unidentified *Fermi* sources and catalogs of galactic young objects, such as YSOs, WR stars, Of stars and OB associations. We have found a statistical correlation between gamma-ray sources and YSOs. The correlation with the early type stars with strong winds remain unclear, since the candidates are located in crowded fields with many other alternatives to the gamma-ray emission and the probability of chance association is high. In the case of OB associations the probability of chance association is negligible. However, we cannot assign a specific counterpart to the gamma-ray emission because of the high angular size of most of OB associations. What we have presented here is the first statistical evidence for gamma-ray emission from massive YSOs.

4

Gamma-rays from Star-Forming Regions: the case of Monoceros R2

4.1 Introduction

Monoceros R2 (hereafter Mon R2) is named after the second association of reflection nebulae in the constellation of Monoceros, i.e. the Unicorn, following the nomenclature established in early original studies (van den Bergh 1966). More precisely, this designation usually refers to a complex of active massive star formation embedded in a nearby (≤ 1 kpc), dense molecular core well below the galactic plane (l=213°7, b=$-$12°6). Strong thermal emission is likely associated with it in coincidence with the bright radio source NVSS J060746$-$062303, previously detected in many other radio surveys. A highly absorbed stellar cluster also exists here in coincidence with NVSS J060746$-$062303. It lies close to the radio source's peak and next to the centre of a giant CO outflow (Bally & Lada 1983; Wolf et al. 1990). The distance to Mon R2 that we will use throughout this work is ~ 830 pc Herbst & Racine (1976). This value is based on the distance modulus resulting from fitting the zero age main sequence in colour-colour diagram of Mon R2 stars.

The Mon R2 central cluster content has been studied in detail in the near infrared by Carpenter et al. (1997). According to these authors, it extends about 1.1 pc × 2.1 pc and contains ≥ 475 stars. The estimated central density amounts to ~ 9000 stars pc^{-3}, with an average visual extinction $A_V \sim 33$ mag. The most likely value for the ratio of low-mass (0.1 to 1 $M_\odot$) to high-mass (1 to 10 $M_\odot$) is about 0.11 and agrees well with expectations from a Miller-Scalo Initial Mass Function. Most spectral classifications of cluster members correspond to late types (G, K and M). They often exhibit infrared
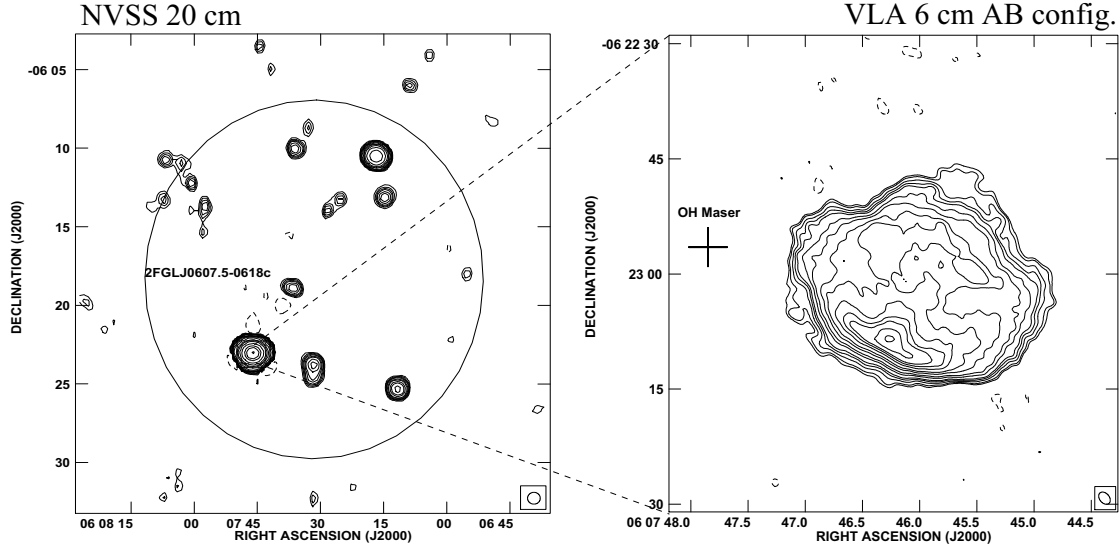
Figure 4.1: **Left.** Radio map of the Mon R2 region from the NRAO VLA Sky Survey at the 20 cm wavelength. The restoring beam is a circular $45''$ Gaussian. Contours shown correspond to -3, 3, 5, 6, 8, 10, 15, 20, 30, 50, 100, 200, 300, 500, 1000, 2000, 3000 and 5000 times 0.7 mJy beam^{-1}, the rms noise. The 95% confidence ellipse for the gamma-ray source detected in the Mon R2 direction is plotted as provided by two year *Fermi* LAT catalog. Mon R2 is the brightest and most relevant radio source consistent with it. **Right.** Zoom of the Mon R2 central region as observed with the VLA at the 6 cm wavelength. This high resolution map has been selfcalibrated using the OH maser in the field (cross) and computed with pure uniform weight. Contours shown correspond to -3, 3, 4, 6, 8, 10, 15, 20, 30, 40, 60, 80, 100, 140 and 180 times 0.7 mJy beam^{-1}, the rms noise. The restoring beam is shown at the panel bottom right corner as $1''80 \times 1''25$ ellipse, with position angle $41°$.

excesses in the near infrared K-band suggestive of a significant population of low-mass pre-main-sequence stars, i.e., mostly classical T Tauri stars. There is some indication that the most massive cluster stars ($\sim 10\ M_\odot$) should be located close to the centre. The earliest spectral type spectroscopically identified corresponds to a B1 star (Carpenter et al. 1997) although, as discussed later in this paper, at least one O-type star could be present as well based on the flux of ionizing photons required to account for the observed radio spectrum. An additional comprehensive review about the physical properties of the Mon R2 complex was published a few years ago by Carpenter & Hodapp (2008). We refer the reader to this work and references therein for further details.

The source known as IRS3 was discovered during historic infrared observations in the 70s (Beckwith et al. 1976) and proposed to be a MYSO. It is the brightest infrared source in the Mon R2 field ($L_{1-25\mu m} \sim 3 \times 10^3\ L_\odot$) and currently considered a likely candidate to drive the giant CO outflow in the region. However, in modern high-angular

resolution observations (Preibisch et al. 2002) IRS3 does not appear to be a single object but resolved into several YSO components, three of them having estimated masses in the 5 to 15 $M_\odot$ range. Based on their variable X-ray emission as detected by the *Chandra* satellite, the same authors infer indirect evidence for magnetic interaction between two of these components and their respective surrounding disks. Mon R2-IRS3 has been also reported to produce highly variable and flaring maser emission. In particular, spectacular maser flares of the hydroxyl (OH) molecule at the 4765 MHz frequency have been recorded with two orders of magnitude changes in brightness, and time scales of few weeks to double in intensity (Smits et al. 1998).

Our interest about Mon R2 comes from theoretical models predicting gamma-ray emission associaed with YSOs under different physical scenarios. As stated in previous Chapters, bipolar outflows from massive YSOs can produce strong shocks when they interact with the surrounding medium and accelerate relativistic particles (Araudo et al. 2007; Bosch-Ramon et al. 2010). Similarly, acceleration of relativistic particles can occur as well in magnetic reconnection events in T-Tauri stars (del Valle et al. 2011). These new kinds of sources could broaden the domain of high-energy astrophysics beyond the study of traditional, well-known gamma-ray sources in the Galactic plane such as pulsars, pulsar wind nebulae, supernova remnants, molecular clouds, gamma-ray binaries, etc. In this context, a systematic cross-identification of gamma-ray sources from the 2 year *Fermi* Large Area Telescope (LAT) catalog, hereafter 2FGL (Nolan et al. 2012), with known star forming regions yielded Mon R2 as a potential gamma-ray source candidate where some of these new physical scenarios could be realized. The following sections are devoted to this purpose by assessing the observational evidence in the Mon R2 case[1].

4.2 Fermi observational data

The unassociated *Fermi*/LAT gamma-ray source 2FGL J0607.5−0618c lies in the direction of the Mon R2 complex and it was included as 1FGL 0608.1−0630c in the previous *Fermi*/LAT catalog. In the left panel of Fig. 4.1, this coincidence is illustrated by plotting the location of its 95% confidence ellipse onto a wide field radio image of the Mon R2 region retrieved from the NRAO VLA Sky Survey, hereafter NVSS (Condon et al. 1998). Preliminary studies, based on the first year *Fermi* catalog only, raised doubts about this source being a possible spurious *Fermi* detection (Mahony et al. 2010). The same authors strongly supported a galactic origin in the alternative case of being a true source. The fact that the 2FGL catalog continues to include this detection, and without any classification flag warning, strongly suggests that this is the case. Nevertheless, the observational parameters are still to some extend affected by the difficulties of accurate background modeling. Based on the 2FGL catalog, the source currently appears detected

[1]The analysis and results explained in this Chapter were published in Martí, J., Luque-Escamilla, P. L., Muñoz-Arjonilla, A. J., Sánchez-Ayaso, E., Munar-Adrover, P., et al., 2013, A&A, 556, A131.

at the 7.6σ significance level. Its variability index is 33.75, a value that does not reach the 41.64 threshold to be considered variable at the 99% confidence level. Significant fluxes are measured in the following energy bands: $F_{100-300\ \mathrm{MeV}} = (1.4 \pm 0.4) \times 10^{-8}$ ph cm^{-2}s^{-1}, $F_{300-1000\ \mathrm{MeV}} = (6.75 \pm 1.4) \times 10^{-9}$ ph cm^{-2}s^{-1}, and $F_{1-3\ \mathrm{GeV}} = (1.2 \pm 0.3) \times 10^{-9}$ ph cm^{-2}s^{-1}. The corresponding spectrum is well represented by a power-law with spectral index $\gamma = 2.39 \pm 0.25$.

4.3 Fermi/LAT data analysis

Fermi is a gamma-ray space telescope launched in June 2008. It carries two instruments: the Large Area Telescope (LAT) and the Gamma-ray Burst Monitor (GBM). The LAT works in the 20 MeV to 300 GeV energy range and has a bigger collection area than any other past mission with more than 8000 cm^2. Also its angular resolution is much better than previous gamma-ray telescopes, being less than $0°.15$ for energies below 10 GeV. *Fermi*/LAT operates in scanning mode observing continuously the whole sky and thanks to its wide field of view covers the full celestial sphere every few hours. We have reanalyzed all the *Fermi*/LAT data of Mon R2 region available since the beginning of the mission (2008 August 5: MJD 54683) until 2012 April 13 (MJD 56030) which implies an observation time of 3 years and 8 months. We took into account all the photons around a $25°$ circle centered on 2FGL J0607.5$-$0618c with our main goals being to obtain an updated light-curve and spectrum of our target source. This almost doubled the observation time as compared to the present 2FGL catalog. For this purpose, we used the *Fermi Science Tools* provided by the *Fermi* satellite team. The version of the Science Tools used was `v9r27p1` with the P7SOURCE_V6 instrument response function (IRF). The reader is referred to *Fermi* instrumental publications for further details about IRFs and other calibration details (Ackermann et al. 2012). We have adopted the current Galactic diffuse emission model (`gal_2yearp7v6_v0`) in a likelihood analysis and `iso_p7v6source` as the isotropic model, and the second point source catalog `gll_psc_v07` has been used[2]. In the modelisation of the data, the galactic background and diffuse components remained fixed. We selected Pass7 Diffuse class events with energies between 0.2 and 300 GeV. Among them, we limited the reconstructed zenith angle to be less than $105°$ to greatly reduce gamma rays coming from the limb of the Earth's atmosphere. We selected the good time intervals of the observations by excluding events that were taken while the instrument rocking angle was larger than $52°$.

To get both the light-curve and spectrum, we used a power-law model based on the 2FGL catalog for all sources within a $25°$ radius around the position of our target 2FGL J0607.5$-$0618c. Centered on it, we also define a closer region of interest (ROI) covering only $10°$. The data reduction procedure is always based on a likelihood analysis in two steps. The first one used the Minuit optimizer to fit both the amplitudes and

---

[2]`http://fermi.gsfc.nasa.gov/ssc/data/access/`

spectral indices of sources within the 10° ROI, and only the amplitudes for those outside it. The second step involved the Newminuit optimizer for fitting only the spectral indices for those sources inside the ROI, while the rest of parameters remained fixed. At all times, the central target source 2FGL J0607.5−0618c kept all its parameters free.

To obtain the light-curve we have divided our data sample into 60 day bins and performed a full unbinned likelihood analysis on each of them. On the other hand, to get the source spectrum we divided our sample in energy bins and carried out a binned likelihood analysis for each bin.

4.4 Results

The final results of these analysis can be seen in Figs. 4.2 and 4.3 for the light-curve and spectrum, respectively. In Figure 4.2, errors in flux and in the spectral index Γ are calculated through the covariance matrix of all the free parameters in the model. The likelihood analysis gives also a Test Statistic (TS) value, whose square root is similar to the significance of the signal that we get from the position of the source. There are only 9 bins out of 21 with a $\sqrt{TS} > 4.0$. The spectral fitting yields a spectral index $\gamma = -2.73 \pm 0.09$, steeper than the one in the 2FGL catalog, and an energy flux of $F(E > 200\text{MeV}) = (2.20 \pm 0.25) \times 10^{-8}$ ph cm^{-2} s^{-1}, (TS=154.25, equivalent to 12.42σ). At the Mon R2 distance of 830 pc, this is equivalent to a gamma-ray luminosity $L_\gamma = 1.2 \times 10^{33}$ erg s^{-1}. The source is not detected at energies above ~3 GeV (see Figure 4.3).

All errors quoted up to this stage are statistical only. Systematic errors are a delicate issue to assess and their calculation may be complicated. The *Fermi* collaboration uses bracketing IRFs which vary in effective area and from them they calculate the systematic effect on the analysis results. Unfortunately, these IRFs are not public and we cannot estimate the systematic errors in this way. Typically, the systematic uncertainty is found to follow more or less the statistical one and is of the same order (Nolan et al. 2012), i.e., being larger for fainter sources in relative terms. More precisely, the dispersions of flux and spectral index are 0.8σ for sources with Galactic latitude $|b| < 10°$ (2FGL 0607.5−0618c is at Galactic latitude $b = -12°6$). The systematic error in the flux calculation depends on $x = \log(E/\text{MeV})$ and amounts to 10% for $x = 2$, 5% for $x = 2.75$ and 20% for $x = 4$ (Abdo et al. 2009). We have linearly interpolated these values to account for the systematic uncertainty in the spectral points shown in Fig. 4.3 (black error bars).

In addition, we have produced a gamma-ray image of the region containing the source 2FGL J0607.5−0618c (see Fig. 4.4). The centroid of its counts excess has been estimated using the `gtfindsrc` function. The source best fitted position is now RA=$06^h08^m10.87^s$ and Dec=$-06°29'32.8''$ with an error circle of 0.19°, which is displaced 0.25° from the original 2FGL position. Mon R2 is still well inside our new error circle. To study possible deviation from the point-like source we have used the `gttsmap` function to generate two TS-maps of the ROI, one of them with a model containing 2FGL J0607.5−0618c and the
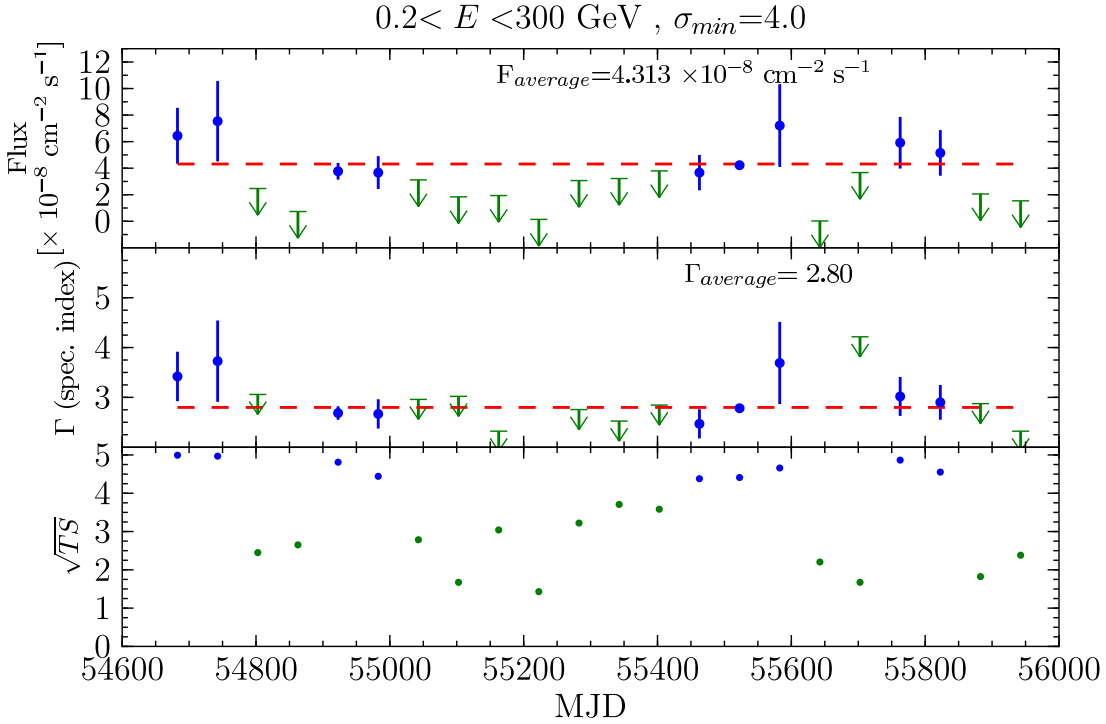
Figure 4.2: Light-curve of 2FGL J0607.5–0618c in the 0.2–300GeV energy range. Upper pannel: *Fermi*/LAT light curve of 2FGL J0607.5–0618c sampled with 60 day bin intervals. Middle pannel: fitted spectral index Γ for each light-curve bin. Lower pannel: value of $\sqrt{TS}$ value for each light-curve bin. Bins with $\sqrt{TS} < 4.0$ (σ_{min}) are represented as upper limits. Horizontal dashed lines represent average values.

other without it. The residuals after subtracting these two TS-maps show that our source is not extended. We also checked for extension by producing a model map using the `gtlike` task with the output model from the binned likelihood analysis, and subtracting it from a counts map generated with `gtbin`. Again, the residuals map indicates no signal of extension for 2FGL J0607.5−0618c.

4.5 Discussion

We have analyzed 3 years and 8 months of *Fermi*/LAT data and the gamma-ray source 2FGL J0607.5−0618c has been confirmed with higher confidence (12σ) as compared to the not so significant detection in the 2FGL catalog. While the spectral properties remain comparable to those anticipated by the 2FGL catalog, the light curve resulting from the whole *Fermi* database analysis is consistent with a steady level of emission. The source fades into non-detectable levels for energies above 2 GeV.

The region within the *Fermi* error ellipse is populated with several young sources.
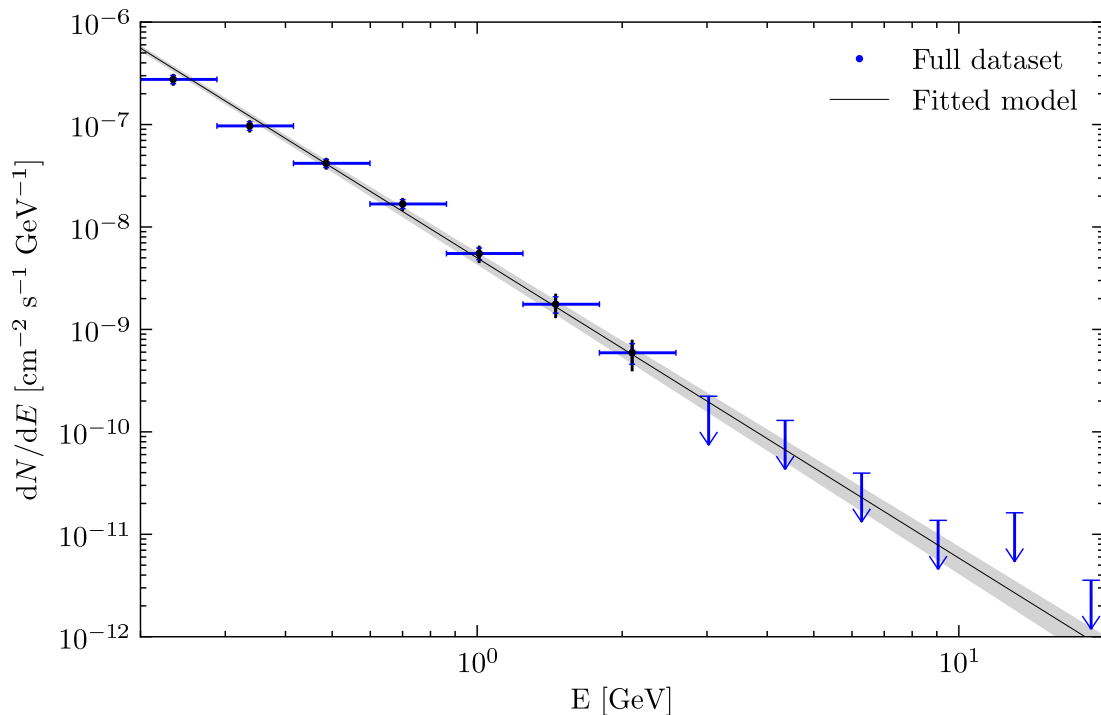
Figure 4.3: *Fermi*/LAT spectrum of 2FGL J0607.5−0618c resulting from our binned likelihood analysis. Shaded region represents the final power-law fit and its uncertainty resulting from this work. Black error bars display the estimated systematic error.

The gamma-ray photons detected by *Fermi* may come from one or more of the low energy sources found in this region. We explore in the next subsections different possible counterparts of 2FGL J0607.5−0618c.

4.5.1 Gamma rays coming from a massive YSO

In Monoceros R2 there is a radio and IR source known as IRS3. This source splits into at least 6 components when observed at high angular resolution (Preibisch et al. 2002). The brightest components of IRS3 might be two MYSOs powering collimated outflows, as they are consistent with measurements of OH maser emission in the IR.

As seen in Chapter 2, MYSO outflows produce strong shocks when collide with the surrounding molecular cloud and in these shocks particles can be accelerated via the Fermi mechanism up to relativistic energies. In a dense medium, relativistic Bremsstrahlung is the dominant emission process, while IC would be negligible. *pp*-interactions are the second main contribution in the gamma-ray domain. The timescales for electrons for synchrotron, IC and relavisitic Bremsstrahlung are (Bosch-Ramon et al. 2010):
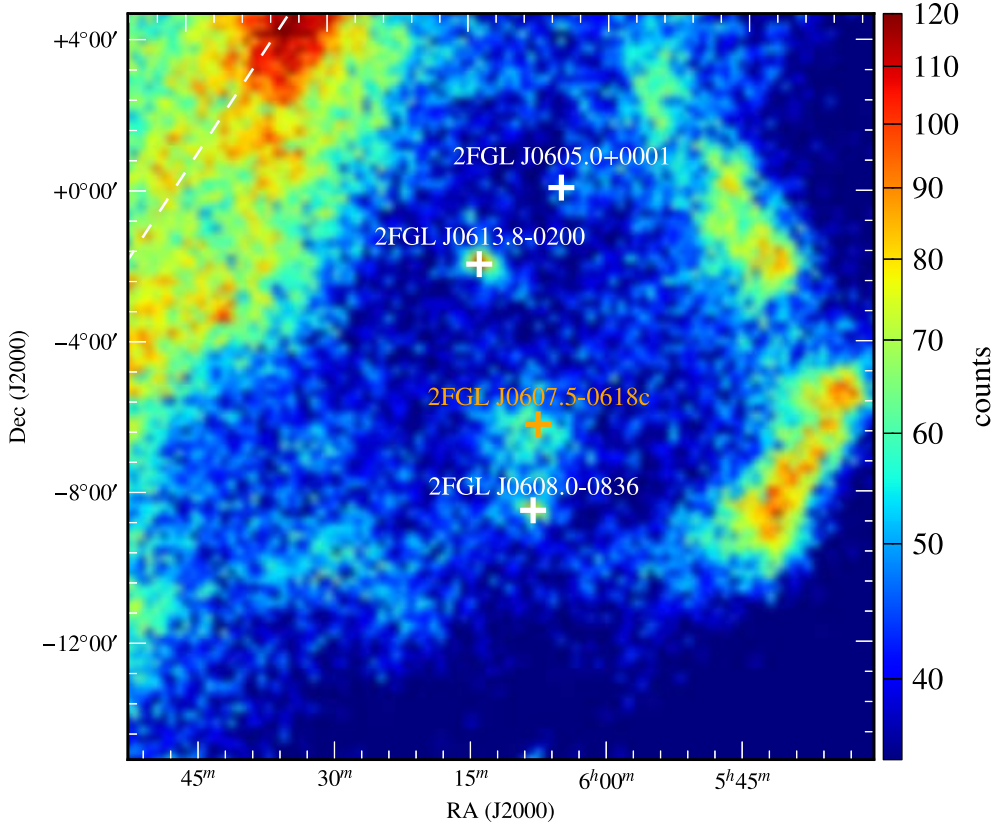
Figure 4.4: Image of the 2FGL J0607.5−0618c field resulting from the *Fermi*/LAT data processed in this work. The image has been smoothed with a 2-pixel Gaussian kernel. The target centroid position is marked at the center with an orange cross. Other sources from the 2FGL catalog are also marked as white crosses for image completeness. The white dashed line indicates the location of the Galactic plane.

$$t_{\mathrm{syn}} \simeq 4 \times 10^{11} B_{-3}^{-2} E_{\mathrm{GeV}}^{-1} \ \mathrm{s}$$
$$t_{\mathrm{IC}} \simeq 1.6 \times 10^{13} u_{\mathrm{IR}-9}^{-1} E_{\mathrm{GeV}}^{-1} \ \mathrm{s}$$
$$t_{\mathrm{Brem}} \simeq 3.5 \times 10^{11} n_3^{-1} \ \mathrm{s}$$

where B_{-3} is the magnetic field in mG, $u_{\mathrm{IR}-9} = u_{IR}/10^{-9}$ erg cm^{-3} is the energy density of the IR photon field and n_3 is the number density of the shock region in units of 10^3 cm^{-3}. Then, the predicted emission from relativistic Bremsstrahlung is of the order of the inferred gamma-ray luminosity $L_\gamma = 1.2 \times 10^{33}$ erg s^{-1}.

4.5.2   T-Tauri stars in Monoceros R2 as possible gamma-ray sources

Monoceros R2 is populated with a number of young stars from which almost one hundred are identified as T-Tauri stars. They have been detected in the IR and X-rays (Nakajima et al. 2003).

As stated in Chapter 2, T-Tauri stars are possible gamma-ray emitters (del Valle et al. 2011) with expected luminosities of the order of 10^{31}–10^{32} erg s^{-1}. This emission is expected to arise from turbulent magnetic reconnection events in the magnetosphere of the protostar. The production of gamma rays in this scenario requires a relatively high magnetic field, allowing for a maximum energy of the particles beyond 100 GeV. Based on the X-ray activity of T-Tauri stars (Feigelson & Montmerle 1999) suggest that the magnetic field can be as high as $\sim 10^2$ G. The emission would be produced by the ejected protons which interact with the matter in the environment of the protostar (del Valle et al. 2011).

In the case of Monoceros R2, assuming that each of the T-Tauri stars contribute with a luminosity of $\sim 5 \times 10^{31}$ erg s^{-1}, a hundred of them would inject a total luminosity of $\sim 5 \times 10^{33}$ erg s^{-1} at energies above 200 MeV, which is compatible with the value of the gamma-ray luminosity found in our analysis of *Fermi* data.

4.5.3   Considering other origin for the gamma-ray emission

Although the detected gamma-ray emission is compatible with the expectations from MYSOs as well as with the T-Tauri population present in the Monoceros R2 region, other sources of gamma-ray emission must be considered since the error circle that we obtained through our analysis of *Fermi*/LAT data is big enough to contain other possible candidate counterparts.

We searched in the *Fermi*/LAT 95% confidence circle for objects that could be counterparts to the high-energy emission which were also unrelated to the Monoceros R2 SFR. We centered our attention to the NVSS catalog (Condon et al. 1998). In the left pannel of Figure 4.1 we see that there are few radio sources compatible with the 2FGL source. Among them, we find NVSS J060716−061030, a relatively radio bright source with a non-thermal spectrum compatible with being a blazar, although no other information at X-rays or optical is available. There is also NVSS J060757-061347, which is coincident with a 2MASS source with X-ray emission, compatible with being an YSO (Nakajima et al. 2003). This is the only radio source in the region, except for the mentioned inside the Monoceros R2 region, with an X-ray counterpart. Other bright radio sources appear within the error circle of the *Fermi* detection, such as NVSS J060728−061359 and NVSS J060731−062356, but lack of information about their radio spectrum and lack of X-ray coverage of the region does not allow us to classify these sources as possible high-energy emitters.

4.6 Conclusions

We have analyzed 3 years and 8 months of *Fermi* data of the Monoceros R2 SFR and our results improved those from the 2FGL. We confirmed 2FGL J0607.5−0618c as a gamma-ray source with higher confidence level than the 2FGL, obtaining a signifficance of 12σ. The light curve analysis indicates that the source is steady up to two-month timescales, while our spectral fitting is consistent with a powerlaw with a softer photon index, compared to the 2FGL, with the source detected only up to 2 GeV.

We have explored the possible candidate counterparts in the error circle that we derived from our analysis and we found that given the gamma-ray luminosity that we obtain, the detected gamma-ray emission is compatible with being produced by the collective effects of the emission from MYSOs and T-Tauri stars present in the Monoceros R2 region.

We also considered other possible counterparts unrelated to those in Monoceros R2, but lack of information about the radio sources present inside the *Fermi* error circle prevent us to stablish other clear explanation to the gamma-ray emission.

5

Studying the non-thermal lobes of IRAS 16547–4247 through a multi-wavelength approach

5.1 Introduction

Massive young stellar objects have turned out to be a possible population of high-energy emitters (Araudo et al. 2007; Romero 2008; Bosch-Ramon et al. 2010), and several attempts to identify gamma-ray candidates have been carried out by various authors (Munar-Adrover et al. 2011; Araudo & Rodríguez 2012; Martí et al. 2013). It is still unclear how massive stars form, although it is clear that outflows, in particular jets of high speed and high kinetic power, are involved in the process (Garay & Lizano 1999; Reipurth & Bally 2001; Garay et al. 2003).

The jets of MYSOs can propagate through the molecular cloud that hosts the protostar and even break its boundaries. At the jet-end point, strong shocks are expected to form that lead to non-thermal emission. Non-thermal synchrotron emission has been identified in a few sources, for instance IRAS 16547–4247 (Garay et al. 2003), Serpens (Rodríguez et al. 1989), W3(OH) (Wilner et al. 1999), and HH 80-81 (Martí et al. 1993; Carrasco-González et al. 2010). It has been recently reported possible non-thermal X-ray emission arising from HH 80-81 lobe (López-Santiago et al. 2013), being it the first time that non-thermal emission coming from the lobe of a MYSO is detected. Among these sources, IRAS 16547-4247 seems a particularly good candidate to produce high-energy emission (Araudo et al. 2007; Bosch-Ramon et al. 2010). This source is likely a young O-type

protostar and has an associated highly collimated outflow. Located at a distance of 2.9±0.6 kpc, this protostar was associated with a triple radio-continuum source consisting of a compact central object and two lobes located symmetrically from the central source in the northwest-southeast direction at a projected distance of 0.14 pc (Garay et al. 2003). The radio emission from the central object has a spectral index of $\alpha = 0.49$ ($F \propto \nu^\alpha$), consistent with free-free emission from a thermal jet, and the north and south lobes have spectral indexes of -0.61 and -0.33, respectively, characteristic of non-thermal emission. Infrared (IR) data show that IRAS 16547–4247 is one of the most luminous ($\sim 6.2 \times 10^4 L_\odot$) protostellar objects associated with an outflow known so far. The high IR luminosity of IRAS 16547–4247 implies a photon field with an energy density $u_{ph} \sim 2 \times 10^{-9}$ erg cm^{-3} in the region. The total jet luminosity of IRAS 16547–4247 has been estimated to be on the order of 10^{36} erg s^{-1}. The size of the core in which IRAS 16547–4247 is embedded is 0.38 pc and has a density of $n_c \simeq 5 \times 10^5$ cm^{-3} (Garay et al. 2003), giving a high hydrogen column density $N_H = 3.0 \times 10^{23}$ cm^{-2}. In X-rays, IRAS 16547–4247 was observed by *XMM-Newton* in 2004 and only upper limits were obtained (Araudo et al. 2007; Bosch-Ramon et al. 2010), although preliminary results of a more detailed analysis have recently been published (Munar-Adrover et al. 2012).

In this Chapter, we present the final results of a deeper analysis of *XMM-Newton* archival data from 2004 and revisit the modeling at high energies, taking into account Coulombian losses that were not considered in previous modeling[1]. The reliable X-ray detection and the impact of the Coulombian losses imposes strong constraints on the multi-wavelength modeling. The main conclusions of this work are the likely thermal Bremsstrahlung origin of the X-ray emission, and the strengthening of the prediction that gamma-ray radiation indeed takes place under reasonable physical conditions of the jet termination region.

5.2 A physical model for IRAS 16547–4247

IRAS 16547–4247 displays a thermal jet with non-thermal radio lobes at its termination region. The action of the jet onto the surrounding medium leads to two shocks: a forward shock (FS) that moves through the molecular cloud, and a reverse shock (RS) that moves inside the jet itself. These shocks can accelerate electrons and protons, which leads to the observed non-thermal radio spectrum through DSA (Fermi first order) (Drury 1983).

We consider here the emission coming from the RS only, since the FS is expected to have a very low velocity and no significant energetics (Bosch-Ramon et al. 2010). From now on, *pre-shock* and *post-shock* refer to the RS. We assumed that the mass density in the non-thermal emitter associated to the RS region is higher than the one given by the Rankine-Hugoniot conditions. This is a consequence of the mixing of RS and FS material at the contact discontinuity between the two shocked regions. This increase in density

---

[1]Published in Munar-Adrover, P, Paredes, J.M., Bosch-Ramon, V., Iwasawa, K., 2013, A&A, 559, A13.

affects the intensity of the high-energy radiation produced in the RS non-thermal emitter, since the emission mechanisms relevant here depend strongly on the density, for instance relativistic Bremsstrahlung for electrons.

The RS is expected to produce thermal and non-thermal emission through different processes. We used a one-zone model to compute the non-thermal emission of the RS, taking into account synchrotron, relativistic Bremsstrahlung, inverse Compton (Blumenthal & Gould 1970), and pp-collisions (Kelner et al. 2006), as well as particle escape on a timescale t_{esc}, meaning that we solved the transport equation (Ginzburg & Syrovatskii 1964) for a homogeneous emitter. We added to the physics of the model used by Bosch-Ramon et al. (2010) by introducing Coulombian losses (Lang 1999)

$$\begin{aligned}
\frac{dE_{Coul}}{dt} &= -\frac{2\pi e^4 Z^2 n_c}{m_e c^2} c \left[\ln\left(\frac{E}{m_e c^2}\right) - \ln(n_c) + \ln\left(\frac{m_e{}^3 c^4}{\hbar^2 e^2}\right) - 1 \right] \\
&\simeq -5 \times 10^{-19} n_c \text{ erg s}^{-1},
\end{aligned} \tag{5.1}$$

where E is the energy of the relativistic particles and n_c is the medium number density. Introducing these losses has the effect of reducing the relativistic Bremsstrahlung luminosity at X-ray energies compared with previous results.

The parameters used in the model are summarized in Table 5.2, where they are listed in three different groups, depending on whether they come from the observational data or are required to explain the non-thermal or thermal emission.

The FS velocity is expected to be low, so the RS velocity is assumed to be equal to the jet velocity: $v_{RS} \sim v_j = 10^8$ cm s^{-1}. Non-thermal particles (electrons and protons) accelerated by the DSA mechanism have an uncooled energy distribution $Q(E) \propto E^{-\Gamma}$ with $\Gamma \sim 2$. The kinetic energy flux, in terms of luminosity (in erg s^{-1}), injected in the form of accelerated particles, electrons and protons separately, is taken as $10\%^2$ of the RS luminosity: $L_s = \frac{1}{2} S_s \rho v_{RS}^3$, where $S_s = \pi R_j{}^2$ is the shock surface. For simplicity, we have adopted a model in which electrons and protons have the same injection luminosity. We note that with the same energy budget, explaining the radio data through synchrotron emission from pp-electron/positron secondaries in the proton-dominated case will require an increase in the magnetic field to explain the radio data with a somewhat lower gamma-ray flux for the same target density. More detailed studies of different proton-to-electron ratios can be found in Araudo et al. (2007) and Bosch-Ramon et al. (2010).

We also considered that the RS can emit through thermal Bremsstrahlung. The temperature of the plasma in the RS is given by

$$T_{RS} = \frac{3}{32} \frac{m_p v_{RS}^2}{k_B} \simeq 1.1 v_{RS8}^2 \text{ keV} \tag{5.2}$$

---

[2]The adopted fiducial value of 10% for the kinetic energy of the shock that enters non-thermal particles is similar to the efficiency of supernova-remnant shocks that accelerate cosmic rays (e.g. Ginzburg & Syrovatskij (1967), for an early discussion).

for a fully ionized hydrogen plasma, where k_B is the Boltzmann constant and $v_{RS8} = v_{RS}/10^8$cm s^{-1}. This temperature determines the maximum of the thermal emission from the RS. Given expected RS velocity conditions in IRAS 16547-4247, the peak of the thermal Bremsstrahlung emission is at $\sim$1 keV.

The thermal Bremsstrahlung luminosity is given by

$$L_{Br} = \varepsilon_{Br}(n^2, T_{ps}) \cdot V, \tag{5.3}$$

where ε_{Br} is the Bremsstrahlung emissivity (in erg cm^{-3} s^{-1}), which depends on the density of the targets (mainly ionized hydrogen nuclei) and on the post-shock temperature, $V = S_s X$ is the volume of the shocked region, and X the depth of the shocked region. The value of X can be estimated within a factor of a few using the following reasoning: the escape time of the region is

$$t_{esc} \sim \frac{R_{RS}}{v_{esc}}, \tag{5.4}$$

where $v_{esc} \sim v_{RS} \sim v_j$. The shocked material has a mass

$$M_s = S_s \cdot \rho_s \cdot v_{RS} \cdot t_{esc}, \tag{5.5}$$

which can also be expressed as

$$M_s = X \cdot S_s \cdot \rho_s, \tag{5.6}$$

from where it is possible to determine X, which is $\sim R_{RS}$. If the value of X was such that implied $L_{Br} \gtrsim L_s$, the RS would be radiative, and the thermal Bremsstrahlung luminosity should be $L_{Br} = L_s$, since it cannot exceed the RS luminosity. Otherwise, if X is such that $L_{Br} < L_s$, the shock is adiabatic, and the Bremsstrahlung luminosity will be roughly

$$L_{Br} = \varepsilon_{Br} \cdot X \cdot S_s \sim \varepsilon_{Br} \cdot R_{RS} \cdot S_s. \tag{5.7}$$

As mentioned, we considered a mixing of the material of the FS region with material downstream the RS because of the formation of complex structures in the two-shock contact discontinuity (Blondin et al. 1989). This mixing increases the effective density downstream the RS at a certain distance from the shock itself through the presence of matter clumps from the FS region. Although a detailed treatment is beyond the scope of this work, note that for clump filling factors (f) and sizes (R_c) at least $f \cdot R_j > R_c$ (spherical clumps), the relativistic electrons/protons have high chances to enter these denser regions, and in general the populations lose most of their energy through relativistic Bremsstrahlung/pp-collisions. This is the reason why we adopted a density higher than the post-shock value for the non-thermal emitter. However, for the thermal emitter we adopted the post-shock density because this component of the RS material has enough temperature to emit X-rays, whereas in the denser clumps the temperature will be much lower. Given that the volume is mostly filled by normal shocked material, most of the
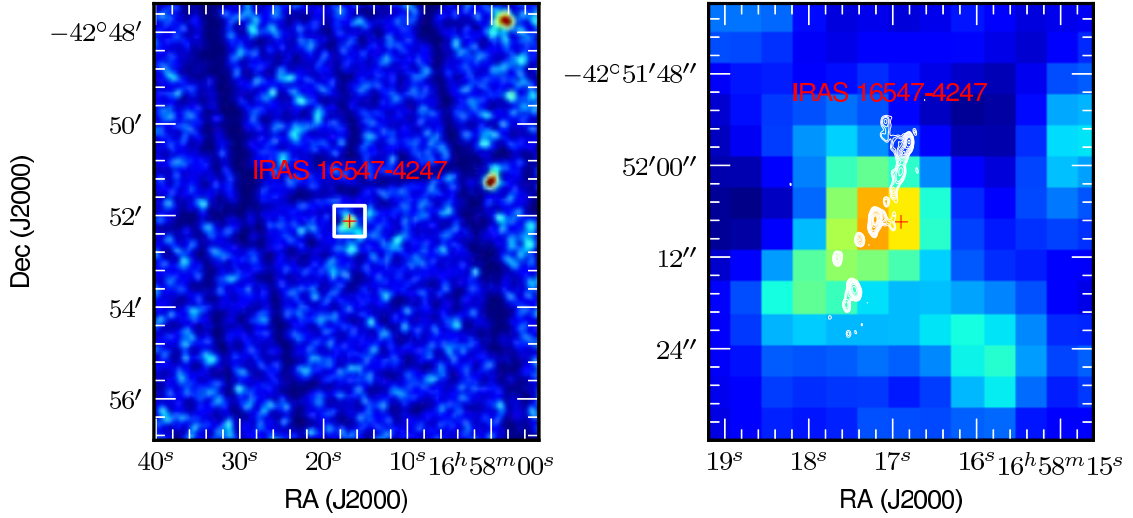
Figure 5.1: EPIC-pn camera image at the position of IRAS 16547−4247 in the 4.5−12.0 keV energy band. Left: surrounding field region to enable a comparison of the source with the surrounding background. Right: zoomed region of IRAS 16547−4247 (white box on left) overlapped with white radio contours (Rodríguez et al. 2008). The red cross marks the nominal position of IRAS 16547−4247 .

synchrotron emission will come from this medium (assuming the same magnetic field).

5.3 XMM-Newton observations and analysis

We analyzed archival data of the sky region surrounding IRAS 16547–4247 taken with the *XMM-Newton*[3] X-ray telescope. Preliminary results of this analysis were published in Munar-Adrover et al. (2012). The observation was carried out in pointing mode in 2004 September 24 and lasted for ∼ 29ks. The medium-thickness optical blocking filter and full-frame mode were used in the three EPIC detectors (pn, MOS1, and MOS2) for the imaging observation. The data were analyzed using the *XMM-Newton* Science Analysis System (SAS) version 12.0.1 and the set of `ftools` from HEASARC. In a first step we cleaned the event files of the three EPIC detectors by removing the flaring high-background periods. For this purpose we selected the good time intervals (GTI) in which the count-rate for the most energetic events (E ≥ 10 keV) was below the standard threshold for each detector. After this cleaning process, the observation time that remained in each of the three detectors was 27.7ks, 27.9ks, and 19.9ks for the MOS1, MOS2, and pn, respectively.

We searched for sources using the `edetect-chain` command in SAS. This command concatenates a series of tasks that produce exposure maps, detector mask images, background maps, detected source lists and sensitivity maps. As a result, a list of detected

---

[3]The observation ID is 0200900101

5. Studying the non-thermal lobes of IRAS 16547–4247 through a multi-wavelength approach
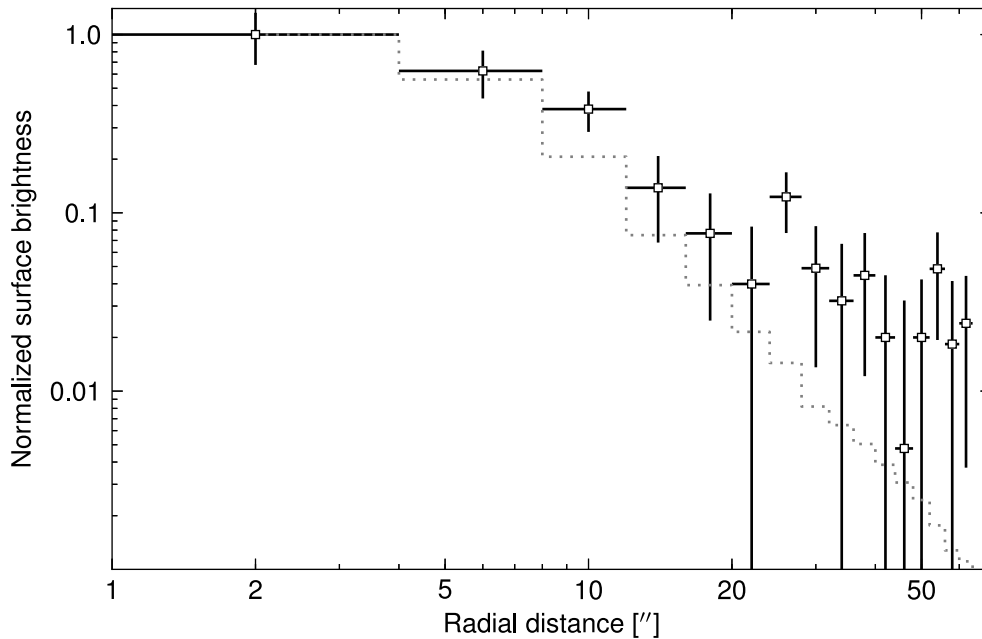

Figure 5.2: Radial profile adjusted to the image of the sum of the three EPIC detectors around the position of IRAS 16547–4247 (squared points) compared to a radial profile of a point-like AGN (dotted line). The PSF of the three EPIC instruments has been taken into account.

sources is obtained containing count-rates, fluxes, and positions for each detected source, among other information. In this observation we detected a total of 22 X-ray sources. Most of them, including the brightest one, are unidentified sources. One source is coincident with a Be star, CD-42 11721.

The detection algorithm revealed for the EPIC-pn detector a source coincident with the position of IRAS 16547–4247 with ~ 34 counts at a confidence level above 4σ, and a flux in the energy range 0.2-12.0 keV of $F_X = (3.79 \pm 0.96) \times 10^{-14}$ erg cm^{-2} s^{-1}. Most of the flux ($\sim 85\%$) is detected in the 4.5-12.0 keV energy band. Figure 5.1 shows the source detected by *XMM-Newton* in this energy range and zooms in, overlapping the radio contours from Rodríguez et al. (2008). The peak of the detected X-ray emission seems to be coincident with the central radio source, although a visual inspection of the counts distribution might indicate a certain extension of the source. The analysis of the other images of the EPIC-pn detector shows no significant excess in the energy range below 4.5 keV at the nominal position of IRAS 16547–4247. Lack of emission below 4.5 keV might be caused by strong photo-electric absorption in the dense environment in which the protostar is located. The source has not been detected in the EPIC MOS1 or in the MOS2 images with the `edetect-chain` meta task, although hints above 2σ are obtained. An analysis of the images with the imaging software XIMAGE v4.5.1 (`http://heasarc.gsfc.nasa.gov/xanadu/ximage/`) produced the results shown in Ta-

ble 5.1. In this table we list the instrument, the energy band, the counts of the source, and the intensity for each energy band, the signal-to-noise ratio (S/N), and a 3σ upper limit for all non-detection cases. The source is only detected in the highest energy band of the EPIC-pn detector.

EPIC instr.	E band [keV]	Counts	Intensity $[\times 10^{-4}\ \text{s}^{-1}]$	S/N	3σ U.L. $[\times 10^{-4}\ \text{s}^{-1}]$
	0.2-0.5	6.7±7.3	5.0±5.4	0.9	24.0
	0.5-0.1	-1.2±5.1	-9.0±3.8	-2.3	16.0
pn	1.0-2.0	7.1±7.1	5.3±5.3	1.0	24.0
	2.0-4.5	19.7±8.3	14.7±6.2	2.4	36.2
	4.5-12.0	35.9±10.0	26.8±7.8	3.4	−
	0.2-0.5	-11.1±1.8	-4.0±0.7	-6.2	5.7
	0.5-0.1	3.7±5.3	1.3±1.9	0.7	8.5
MOS1	1.0-2.0	13.3±8.2	4.8±3.0	1.6	15.0
	2.0-4.5	13.9±8.1	5.2±2.9	1.7	15.1
	4.5-12.0	19.5±9.3	7.0±3.4	2.1	18.4
	0.2-0.5	-1.7±3.4	-6.1±1.2	-5.1	5.2
	0.5-0.1	-3.4±4.4	-1.2±1.6	-7.8	6.1
MOS2	1.0-2.0	-5.2±6.7	-1.9±2.4	-7.8	8.7
	2.0-4.5	18.8±6.5	6.8±2.3	2.9	14.5
	4.5-12.0	20.0±9.1	7.2±3.3	2.2	18.2

Table 5.1: Imaging analysis of IRAS 16547–4247 with XIMAGE.

To determine whether the X-ray emission is extended, as it is observed in the radio band, we adjusted a radial profile to the images of the three EPIC detectors in the 4.5-12 keV band (see Fig. 5.2) where our signal-to-noise ratio is maximum. No clear extension can be inferred when adjusting a radial profile to the sum of the images of the three EPIC cameras or by comparing it with a point-like radial profile from an AGN, NGC 4395 (ObsID 0142830101, observed also on axis and at the same energy band as IRAS 16547–4247), although there are two points at radial distances of $\sim10''$ and $\sim25''$ that slightly depart from a point-like-source radial profile. However, the significance is not enough to claim a deviation from a point-like source. Spectral analysis is not possible because too few counts are detected by *XMM-Newton*, but the detection above 4.5 keV shows that the emission is hard. A deeper observation with better angular resolution is required to elucidate the precise morphology and spectral characterization of IRAS 16547-4247 in X-rays.

5.4 Model results and discussion

5.4.1 Non-thermal high-energy emission

The model we used has an important difference compared with that used in Bosch-Ramon et al. (2010): we included Coulombian losses when computing the distribution of the accelerated particles for the non-thermal emission. This has an effect on the non-thermal radiation. In particular, the relativistic Bremsstrahlung emission is lower by almost one order of magnitude than the emission computed without Coulombian losses in the *XMM-Newton* energy range. This makes the detected X-ray emission of IRAS 16547–4247 higher than the flux predicted by the non-thermal model. In the high-energy range (HE; 100 MeV<E<100 GeV) the model predicts a level of emission of about 10^{33} erg s^{-1}. The main contribution at high energies comes from relativistic Bremsstrahlung, although *pp* interactions contribute slightly at GeV energies. The IC component is negligible at all energy ranges. The spectral energy distribution for one lobe from radio to gamma rays is presented in Fig. 5.3 as dashed lines.

The computed non-thermal emission at high energies for one lobe of the system is still relatively modest. However, the current and projected instruments sensitive to HE and very high-energy (VHE; E > 100 GeV) will not be able to resolve whether the emission comes from one or the other lobe, or if it is the sum of both. For this reason we also computed the non-thermal and thermal emission from the southern lobe and added it to the computed emission of the northern lobe, obtaining the black solid line in Fig. 5.3. This results in a slightly higher level of thermal emission at X-rays within the range of the model uncertainty, and a significant increase in the non-thermal emission at radio and gamma-rays. Accounting for both lobes, the source would be detectable by the current and next generation of Cherenkov telescopes for exposure times ~ 50 h, and even by *Fermi* for exposure times of about six or more years.

5.4.2 Connection with X-ray observations

The former attempt of fitting the X-ray data using only a non-thermal Bremsstrahlung component resulted in an unrealistic set of physical parameters (Munar-Adrover et al. 2012), which even predicted the source to be detectable by *Fermi* in the second source catalog (Nolan et al. 2012). Therefore, to explain the X-ray detection, we introduced a thermal Bremsstrahlung component. Thermal X-rays are expected to originate from the RS region. With the known parameters of the source, one can calculate the post-shock RS temperature with Eq. 5.2, which depends on the velocity of the RS: $v_{RS} \sim v_j = 10^8$ cm s^{-1}. The adopted density is that of the post-shock region, $n_s = 5 \times 10^3$ cm^{-3} (different from the one in the non-thermal emitter, see Section 5.2). The temperature of the RS is $k_B T_{RS} \sim 1$ keV, which is approximately expected to be the peak energy of the thermal component. The resulting thermal Bremsstrahlung has a much higher flux than the detected X-rays
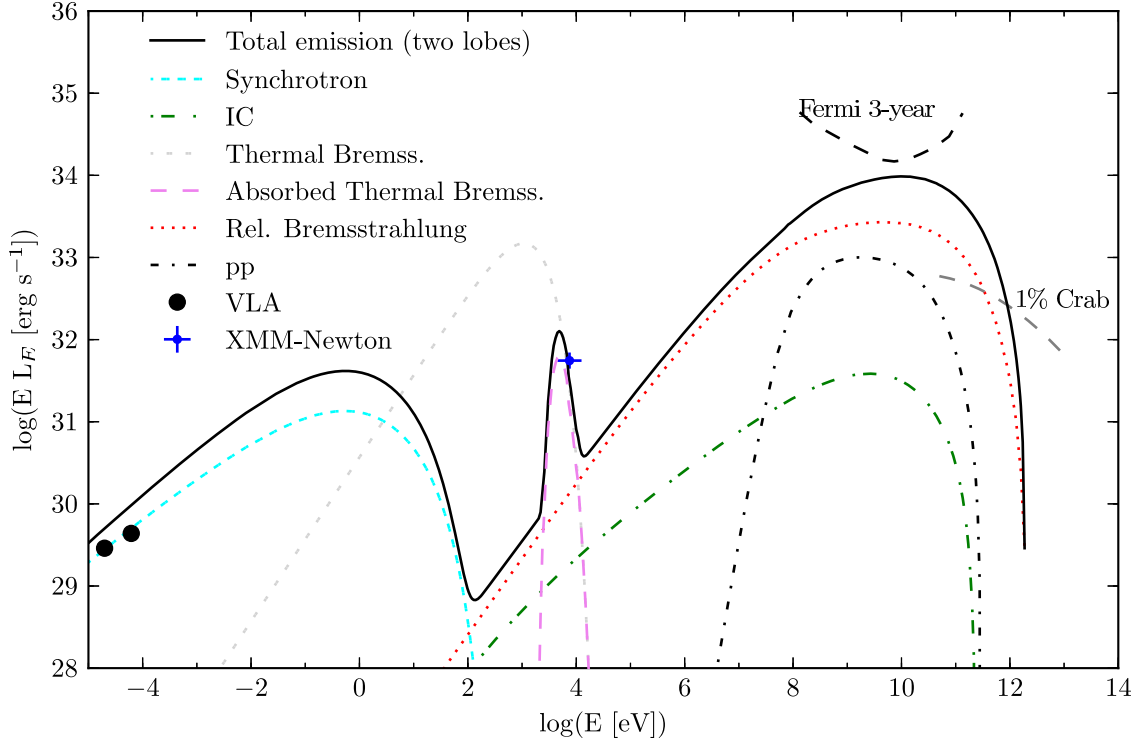
Figure 5.3: Computed non-thermal model including a thermal Bremsstrahlung absorbed component for the IRAS 16547–4247 north lobe. The black solid line represents the total thermal and non-thermal emission from the two lobes of the system. X-ray and radio data-points are also plotted, together with the *Fermi*/LAT three-year (inner Galaxy) 5σ sensitivity curve and the SED for 1% of the Crab Nebula flux, the typical sensitivity of the current Cherenkov telescopes for $\sim$50 h of observation.

and has its peak at lower energies (see the gray solid line in Fig. 5.3). Since the detected emission can be affected by photo-electric absorption at low energies, as expected because the source is embedded in a molecular cloud, we introduced the photo-electric absorption effect (Morrison & McCammon 1983). The column density used to calculate the absorption is shown in Table 5.2, which is obtained from the value of the size and density from Garay et al. (2003). This has the effect of dropping the flux of the thermal Bremsstrahlung emission and displaces the peak to higher energies, making it roughly consistent with the X-ray detection (pink dashed line in Fig. 5.3).

We note that the X-ray emission might also arise from other components of the system. Protostars have accretion disks that emit thermal radiation. The heated material can reach temperatures of up to T$\sim 10^7$ K, and flaring events have been reported involving even higher temperatures, up to T$\sim 10^8$ K (Tsuboi et al. 1998). In low-mass protostars, models show that episodes of magnetic reconnection between the disk material and the protostar

IRAS 16547–4247			
	$L_\star$	[erg s^{-1}]	5×10^{38}
	d	[kpc]	2.9
Observed	n_c	[cm^{-3}]	5×10^5
	N_H	[cm^{-2}]	3×10^{23}
	u_{IR}	[erg cm^{-3}]	2×10^{-9}
	L_j	[erg s^{-1}]	1.5×10^{36}
Non-thermal	Γ		2.0
component	R_j	[cm]	1.6×10^{16}
	v_j	[cm s^{-1}]	10^8
	B	[G]	1.2×10^{-4}
Thermal	T_{RS}	[keV]	1.1
component	n_s	[cm^{-3}]	5×10^3
	X	[cm]	1.6×10^{16}

Table 5.2: IRAS 16547–4247 north observed properties and derived parameters.

lead to X-ray emission and possibly even gamma-ray emission (del Valle et al. 2011). The former might be also occuring in high-mass protostars (Pravdo et al. 2009). Thus, the detected X-ray radiation in IRAS 16547–4247 may come from the central protostar alone, from the RS, or be the sum of the contribution of the RS and the central source. Visual inspection of the source images from the EPIC-pn camera shows a distribution of counts that might indicate a certain extension. As noted, the adjusted radial profile to a point source is consistent with the source being point-like, but there are two points at radial distances of 10″ and 25″ from the centroid of the counts that slightly deviate from the point-like hypothesis. Unfortunately, the spatial resolution of *XMM-Newton* does not allow us to discern wether the emission comes from the central source or from the lobe(s).

5.4.3 Inferring medium conditions from radio data

The observed radio spectrum is consistent with optically thin synchrotron emission. This indicates that the free-free opacity coefficient, τ_{ff}, must be less than 1 in the region:

$$\tau_{ff} = \kappa_{ff} \, l < 1, \tag{5.8}$$

where κ_{ff} is the absorption coefficient (see Rybicki & Lightman 1979) and l is the size of the region. Using this constraint, we can derive an upper limit to the size of the region by estimating the opacity at the observed frequencies. To account for free-free absorption, we adopted a cloud density of $\sim 5 \times 10^5$ cm^{-3} (Garay et al. 2003) and a temperature typical of an HII region, T$\sim 10^4$ K, assuming full hydrogen ionization. Given the characteristics of the emission region, this upper limit results in $l \lesssim 10^{15}$ cm. This indicates that the region where free-free absorption is taking place is a thin shell surrounding the synchrotron
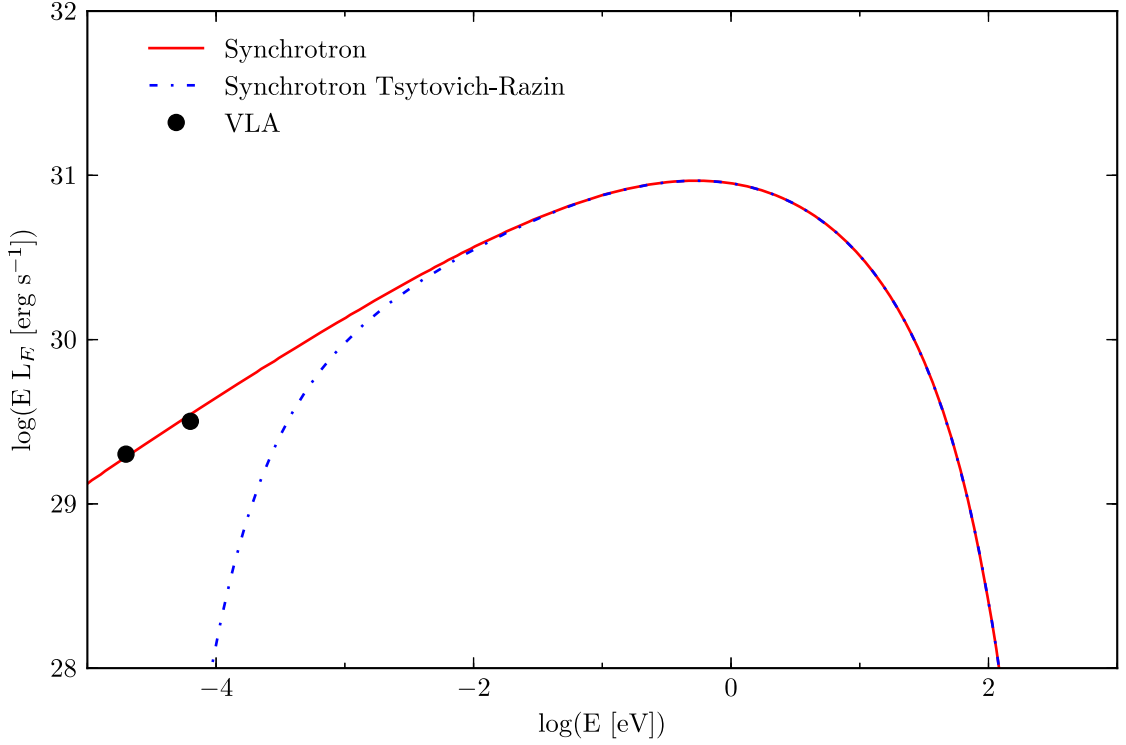
Figure 5.4: Computed synchrotron spectral energy distribution and VLA data points. Two models are shown: one without absorption (except for synchrotron self-absorption) (red solid line) and one accounting for the Tsytovich-Razin effect (blue point-dashed line).

emitter. The thinness of the absorbing region allows the non-thermal radio emission to escape without being significantly absorbed. This fact is consistent with that of strong photo-electric absorption of soft X-rays, as predicted by our model, because this implies that these photons are absorbed within a short distance, ionizing only a thin shell.

The Tsytovich-Razin effect may be also important in the emitting region. This effect produces a suppression of the emission for frequencies below a characteristic cut-off frequency given by

$$\nu_R = 20\frac{n_e}{B},\tag{5.9}$$

where n_e is the number density of free thermal electrons and B is the magnetic field strength (Dougherty et al. 2003). The descent in the level of the emission is due to a change in the refractive index of the medium where the radiation is produced. For the free thermal electron density and magnetic field adopted in our calculations for the non-thermal emitter, $\nu_R \sim 8 \times 10^{10}$ Hz $\equiv 3.5 \times 10^{-4}$ eV. However, the expected decrease in the radio spectrum due to the Tsytovich-Razin effect is not consistent with the VLA data, since the slope of the synchrotron spectral energy distribution (SED) at the detected frequencies is expected to be much harder than the one observed, and the intensity is expected to be

lower (see Fig. 5.4). To be consistent, the density of the region would need to be at least 30 times less dense than the one we adoped in our model to account for non-thermal emission. However, the contact discontinuity between the jet and the cloud shocked material might be very complex. Mixing of the material of the RS with that from the FS is expected and the density excess probably takes the form of clumps. In this complex ambient, electrons can emit in radio through synchrotron radiation in a more diluted medium, and if they enter a clump of dense matter, they will also emit at high energies through relativistic Bremsstrahlung. The probability of entering one clump may be easily on the order of 1, as pointed out in Section 5.2, although we remark that most of the time particles are expected to be in the inter-clump medium.

5.5 Conclusions

We have analyzed archival data of IRAS 16547–4247 observed by the *XMM-Newton* X-ray Telescope. From our analysis we obtained a detection of the source above the 4σ confidence level. Although the spatial resolution of the images is not enough to clarify whether the source is extended or not, the distribution of counts on the detector might indicate an extended nature, similar to the radio images. We were able to roughly explain the X-ray data by thermal Bremsstrahlung plus photo-electric absorption in the cloud. We compared our results and the VLA detections with a one-zone emission model, which improves previous efforts made to study and predict high-energy emission from this system (e.g. Bosch-Ramon et al. 2010) by including Coulombian losses and the two non-thermal radio emitting regions in the calculations. We accounted for mixing of the RS/FS material by adopting an average density $n_{RS} = 5 \times 10^5 \mathrm{cm}^{-3}$ in the RS non-thermal emitter, which enhances the computed gamma-ray flux. Internally, however, there must be clumps of dense material that coexist with a (thermal X-ray emitting) medium at least $\sim$30 times less dense, which probably is the RS post-shock medium. This avoids a strong impact of the Tsytovich-Razin effect on the synchrotron emission at the radio band. Accounting for mixing of the RS-FS material in the non-thermal emitter and the contribution of the two non-thermal lobes, we predicted significant gamma-ray emission above the GeV energy band, which might be detectable by current and future HE and VHE gamma-ray telescopes.

Part II

High-mass X-ray Binaries

6

Introduction

6.1 Binary systems

Stars tend to form in clusters, as it has been stated in Chapter 2. A fragmentation of the progenitor molecular cloud during the collapse phase would produce the formation of a binary or a multiple star system. In fact, a large fraction of the stars in our galaxy are part of multiple star systems.

Binary systems are of major importance for astronomers because the observation of the orbit of a two star system allows to calculate the mass of the components by direct measurements and other indirect properties, such as the radius and the density. Depending on the way they are detected we define diferent kinds of binary systems: spectroscopic, eclipsing, astrometric and visual binaries.

With the advent of new instruments to study the sky at higher frequencies, such as X-rays and gamma rays, other kind of binary systems were defined, depending on their behaviour at these bands of the electromagnetic spectrum. Binary systems consisting in a main sequence optically visible star (of high or low mass), and a compact object were discovered soon in the first times of high-energy astronomy. Depending on the spectral energy distribution at high energies, we find X-ray binaries and gamma-ray binaries.

6.2 X-ray binaries

X-ray binaries are binary systems composed of a normal optically emitting star and a compact object, which can be a neutron star (NS) or a black hole (BH). The companion star may be a low-mass or a high-mass star. Depending on the mass of the companion

star, we can distinguish between low-mass X-ray binaries (LMXBs) and HMXBs. If the system displays bipolar radio jets and an accretion disk it is called a microquasar, due to the similitudes with the actual quasars. Among the class of X-ray binaries we find SS 433 (Abell & Margon 1979; Fabian 1980) and MWC 656 (Casares et al. 2014), which are the first microquasar discovered and the first binary system containing a Be star and a BH, respectively. These two systems have been object of exhaustive studies throughout this thesis.

6.2.1 Low-mass X-ray binaries

In LMXBs the companion star has lower mass than the compact object, being a main sequence star or a red giant. The companion fills the Roche lobe of the system and then part of its matter is transfered to the compact object, which starts to accrete material through an accretion disk. There are several low-mass X-ray binaries containing a BH. These systems have been studied for years in X-rays and in radio and it has been observed that most of the known systems share similar behaviour at these wavelengths, displaying strong outbursts and periods of quiescent activity. There is a unified model that explains the complex behaviour of BH X-ray binaries (BHXBs) (see Fender (2010) for a review). At the beginning of the outburst and during the outburst decay, the source is in a hard state (see Homan & Belloni (2005); Remillard & McClintock (2006) for different nomenclatures). The hard state is characterized by an X-ray spectrum well-modeled by a powerlaw with photon index $\Gamma \sim 1.5$ and a luminosity of less than 0.1 L_{Edd}. This is a jet-active state. The X-ray emission is non-thermal and thought to be due to comptonization in a corona near the BH (Zdziarski et al. 1998; Nowak & Wilms 1999) or to optically thin synchrotron emission from the base of the jet (Markoff et al. 2005). Radio observations show a self-absorbed steady compact jet, resolved in a couple of cases (Stirling et al. 2001; Dhawan et al. 2000), whose power positively correlates with the X-ray luminosity (e.g. Gallo & Fender (2002); Gallo et al. (2012)). This correlation is known as the disk/jet coupling. As the X-ray luminosity increases towards the Eddington limit, the source enters a very-high state where the X-ray spectrum shows also a significant thermal/disk component with $k_B T \approx 1$ keV (Remillard & McClintock 2006). In this state we observe the compact jet quenching and the appearance of transient, discrete, powerful ejections. After that the source enters a soft state, characterized by a spectrum dominated by a thermal/disk component and no radio jet emission. At the end of the outburst the BH X-ray emission decays again to a hard state below 0.01–0.04 L_{Edd} and ultimately to a quiescent state. The detected luminosities of the known systems during the quiescent state range from 5×10^{-9} to 10^{-3} L_{Edd} (Gallo et al. 2012). In quiescence the X-ray spectrum can be fitted with a powerlaw with photon index of $\Gamma = 2.08 \pm 0.07$ (Plotkin et al. 2013). As in the low-hard sate, the emission is of non-thermal origin from the corona or the jet base, but with a slightly softer spectrum. These state changes have been well studied in BH LMXBs, but poorly studied in BH HMXBs due to the low number of sources and the fact that all

known BH HMXB are persistent in X-rays or active all the time.

Recent studies for BH LMXBs reveal that the radio/X-ray correlation described above is bimodal at high X-ray luminosities (Gallo et al. 2012; Corbel et al. 2013). In any case, the upper branch in the $L_{\rm r}$ vs $L_{\rm X}$ plot extends down to quiescence, with $L_{\rm X}$ as low as 10^{31} erg s^{-1} (corresponding to $\sim 10^{-8} L_{\rm Edd}$).

These systems have not been detected in gamma-rays yet.

6.2.2   High-mass X-ray binaries

HMXBs harbour an O or B star as companion with a NS or a BH. In the cases with an O-type star the accretion is driven by Roche lobe overflow and/or due to a strong stellar wind. There are also HMXB containing a Be star, which are fast rotating and have a strong equatorial wind that forms a decretion disk around the star. The accretion onto the compact object is driven by the capture of material from the decretion disk when the compact object interacts with it.

Several of the known HMXBs contain a neutron star, which is known because the pulsations of this object are detected. In the case of BH HMXBs in our Galaxy there was only Cygnus X-1, with an O9-type companion star, which is always emitting at high X-ray luminosities. It is still unknown if the disk/jet coupling found in BH LMXBs also applies in the case of BH HMXBs. Among the HMXB class, only Cygnus X-3 has been clearly detected at gamma-ray energies (Fermi LAT Collaboration et al. 2009), whereas for Cygnus X-1 there is a 4.9σ hint of detection reported by MAGIC (Albert et al. 2007b) and a few low-significance detections by *AGILE* (Sabatini et al. 2010; Bulgarelli et al. 2010) and *Fermi* (Bodaghee et al. 2013).

In the next Chapters of this thesis we will address the case of a new member of the BH HMXBs, MWC 656, which is the first known binary system with a Be star and a BH.

6.3   Gamma-ray binaries

Gamma-ray binaries are systems comprising a massive star and a compact object displaying X-ray and gamma-ray emission with a peak at the gamma-ray energies. They show usually periodicity in their emission form radio to gamma rays. There are currently five known gamma-ray binaries, LS I +61 303, LS 5039, PSR B1259-63, HESS J0632+057 and 1FGL J1018.6-5856. There are two scenarios that try to describe the phenomenology observed in these extreme systems: the microquasar and the binary pulsar scenarios.

In the first one, the detected gamma-ray emission is produced by the relativistic particles accelerated in the jet that arises near the compact object. These particles upscatter the stellar photons from the companion star giving rise to gamma radiation. The first detection of a microquasar candidate by Mirabel et al. (1992) demonstrated the importance of non thermal processes and suggested the production of VHE radiation in binary systems. The broadband variability in the emission of these systems is interpreted as
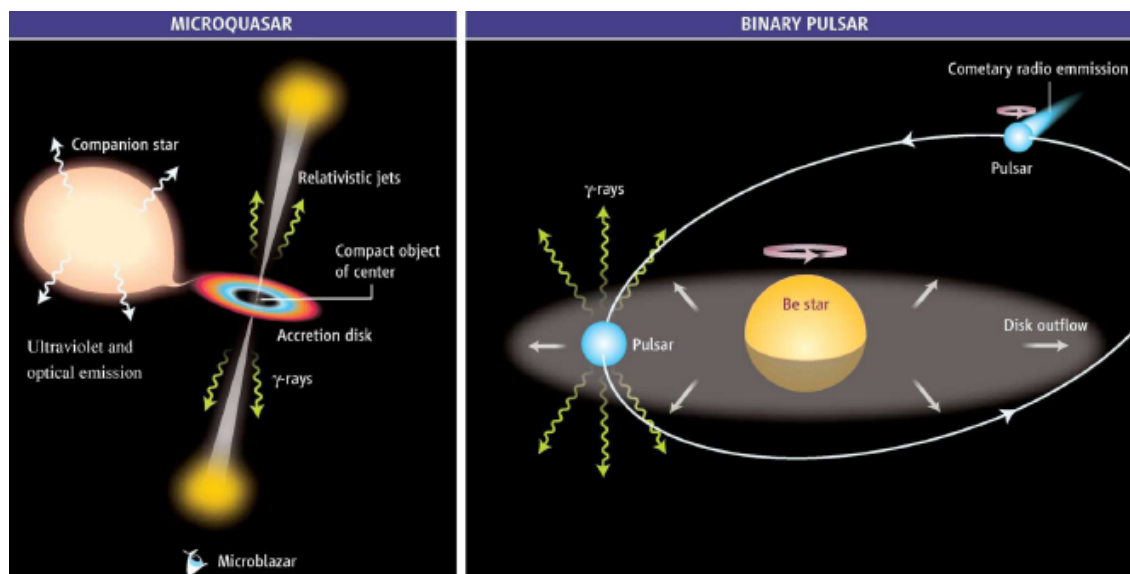
Figure 6.1: Sketch of the two scenarios for gamma-ray binaries. *Left*: the microquasar scenario. *Right*: the binary pulsar scenario. Figure from Mirabel (2006).

changes in the accretion rate onto the compact object which in turn is produced by the orbital motion around the companion star.

The second one, the binary pulsar scenario, was already proposed more than 30 years ago by Maraschi & Treves (1981). In this scenario, the relativistic wind of a young non-accreting pulsar is colliding with the strong stellar wind of the companion. Particles are accelerated at the shocked region between the two winds and radiate as they travel, probably at relativistic velocities. Non thermal radiation is emitted from radio to X-rays by the Synchrotron mechanism, and at higher energies through IC upscattering of stellar photons. The electrons scaping the system would then form a nebula pointing towards the oposite direction of the companion star, which can be compared to a cometary tail, as observed in some systems (Dhawan et al. 2006; Moldón et al. 2012).

In both scenarios the variability can be also produced by geometrical effects on the IC scattering and by the gamma-gamma absorption (see Bosch-Ramon & Khangulyan 2009 and references therein).

One can distinguish between gamma-ray binaries and X-ray binaries that emit in gamma rays (such as Cygnus X-3) by studying their SED: X-ray binaries are characterized by a SED that peaks at X-rays (hence their name), and gamma-ray binaries, as noted, display a SED peaking at gamma rays.

Several years have passed since the discovery of the first gamma-ray binary and there are still a number of open questions about them. Of the five known gamma-ray binaries we only know the nature of the compact object in one case: PSR B1259-63, which contains a fast rotating radio pulsar. In this system the gamma-ray emission is detected when the

neutron wind star interacts with the decretion disk of the donor star during the periastron passage. After this epoch, the system remains quiet in gamma-rays.

The compact objects orbiting the other four gamma-ray binaries are still unknown. In the recent years VLBI studies on LS 5039 and LS I +61 303 have revealed structures that favour the binary pulsar scenario (Dhawan et al. 2006; Massi et al. 2012; Moldón et al. 2012; Moldón 2012). The determination of the nature of the compact object is crucial to determine the physical processes involved in the emission from radio to gamma rays. However, in gamma-ray binaries it has been difficult to elucidate this issue. The detection of radio pulsations would confirm the neutron star nature of the compact object and then it would be possible to find out if it accretes matter from the companion. Unfortunately, the detection of such pulsations has been impossible up to now in systems with close orbits due to free free absorption (see Dubus 2006). Knowing the geometry of the binary systems would also shed light on the nature of the compact object, but to constrain the inclination of the binary is also difficult.

7

Discovery of X-ray emission from MWC 656, the first Be/Black hole system

7.1 Introduction

MWC 656 has been recently discovered as the first Be star orbited by a BH (Casares et al. 2014). This *solves* the problem of the missing Be/BH binaries (Belczynski & Ziolkowski 2009) and opens a window to study the behavior of Be/BH binaries compared to Be/neutron star binaries.

Chronologically, Lucarelli et al. (2010) reported the detection of a new unidentified transient point-like source by *AGILE* at energies above 100 MeV, AGL J2241+4454, with a position uncertainty of 0.6° and a flux $F(E > 100 \text{ MeV}) = 1.5 \times 10^{-6}$ ph cm^{-2} s^{-1}. However, *Fermi*/LAT did not detect emission at HE in subsequent observations. Williams et al. (2010) pointed out the Galactic Be star MWC 656 as the possible optical counterpart. These authors reported an optical photometric periodicity of 60.37±0.04 days for MWC 656, confirmed by Paredes-Fortuny et al. (2012). Casares et al. (2012) established the binary nature of the source through optical spectroscopic observations. In a subsequent work, Casares et al. (2014) presented new data and a double-line solution to the radial velocity curves of the two binary components, allowing them to obtain physical parameters: eccentricity of 0.10±0.04, periastron at orbital phase $\phi_{\text{per}} = 0.01 \pm 0.10$ (phase 0 is defined at the maximum optical luminosity, corresponding to $T_0 = 2\,453\,243.3$ HJD) and mass ratio $M_2/M_1 = 0.41 \pm 0.07$. They also updated the spectral classification of the Be star to B1.5–B2 III, which implies a Be mass in the range 10–16 M$_\odot$ and, therefore, a BH companion of 3.8–6.9 M$_\odot$. This makes MWC 656 the first Be binary with a BH companion. The

system is located at a distance of 2.6 ± 0.6 kpc (Casares et al. 2014).

Flux upper limits of MWC 656 have been obtained at different wavelengths. The source was observed in radio using the European VLBI Network (EVN) at 1.6 GHz on 2011 January 25, February 15 and February 28, at orbital phases 0.82, 0.17 and 0.38, respectively (using the ephemeris reported in Williams et al. 2010). However the target was not detected during this EVN campaign, with 3σ flux density upper limits in the range 30–66 μJy (Moldón 2012).

In the X-ray domain, MWC 656 was observed by *ROSAT* in 1993 July 7–11 at 0.1–2.4 keV energies for a short time ($\sim$3–6 ks each day). Casares et al. (2014) obtained a 90% confidence level (c.l. from now on) flux upper limit of $F_{0.1-2.4 \text{ keV}} < 1.2 \times 10^{-13}$ erg cm^{-2} s^{-1}, assuming a photon index $\Gamma = 2.0$ (typical of BH X-ray binaries (XRBs) in the quiescent state; Plotkin et al. 2013) and an insterstellar hydrogen column density $N_{\text{H}} = 1.4 \times 10^{21}$ cm^{-2}. In addition, two 1-ks *Swift*/XRT observations performed on 2011 March 8 provide a 90% c.l. flux upper limit in the $0.3-10$ keV energy range of $F_{0.3-10.0 \text{ keV}} < 4.6 \times 10^{-13}$ erg cm^{-2} s^{-1} (Casares et al. 2014). The *ROSAT* and *Swift*/XRT observations were carried out at orbital phases 0.63–0.70 and 0.52, respectively.

In the high-energy gamma-ray domain we took all the available *Fermi*/LAT data and analyzed it finding no evidence of a detection and deriving a 95% c.l. upper limit of $F(E > 100 \text{ MeV}) < 7.9 \times 10^{-10}$ ph cm^{-2} s^{-1}. Finally, MWC 656 has been observed at very high energies using the MAGIC Telescopes in 2012 May and June, corresponding to orbital phase intervals 0.83–0.95 and 0.20–0.28, respectively. The source was not detected in any of these observations. Preliminary integral upper limits were set at 95% c.l., assuming an spectral index $\Gamma = 2.5$ at a level of $F(E > 300 \text{ GeV}) < 2.1 \times 10^{-12}$ ph cm^{-2}s^{-1} (López-Oramas et al. 2013).

In this Chapter we show the results obtained from our recent *XMM-Newton* observations. We detect a faint source coincident with the position of MWC 656, making it the first Be/BH binary ever detected in X-rays and thus confirming it as a HMXB. The spectrum can be fitted with a thermal plus a non-thermal component. We discuss our results in the context of wind emission from massive stars, the quiescent state of BH XRBs and the empirical BH radio/X-ray correlation. The analysis and obtained results explained in this Chapter were submitted to Astrophysical Journal Letters[1].

7.2 X-ray observations and analysis

We present here new X-ray observations of MWC 656 performed with *XMM-Newton* for 14 ks[2]. The observations were carried out in pointing mode in 2013 June 4, when the system was at orbital phase 0.08 (close to periastron). The medium thickness optical blocking filter and Full Frame mode were used in the three EPIC detectors (pn, MOS1

---

[1]Munar-Adrover, P., Paredes, J.M., Ribó, M., Iwasawa, K., Zabalza, V., Casares, J., 2014, ApJ Letters, in press.
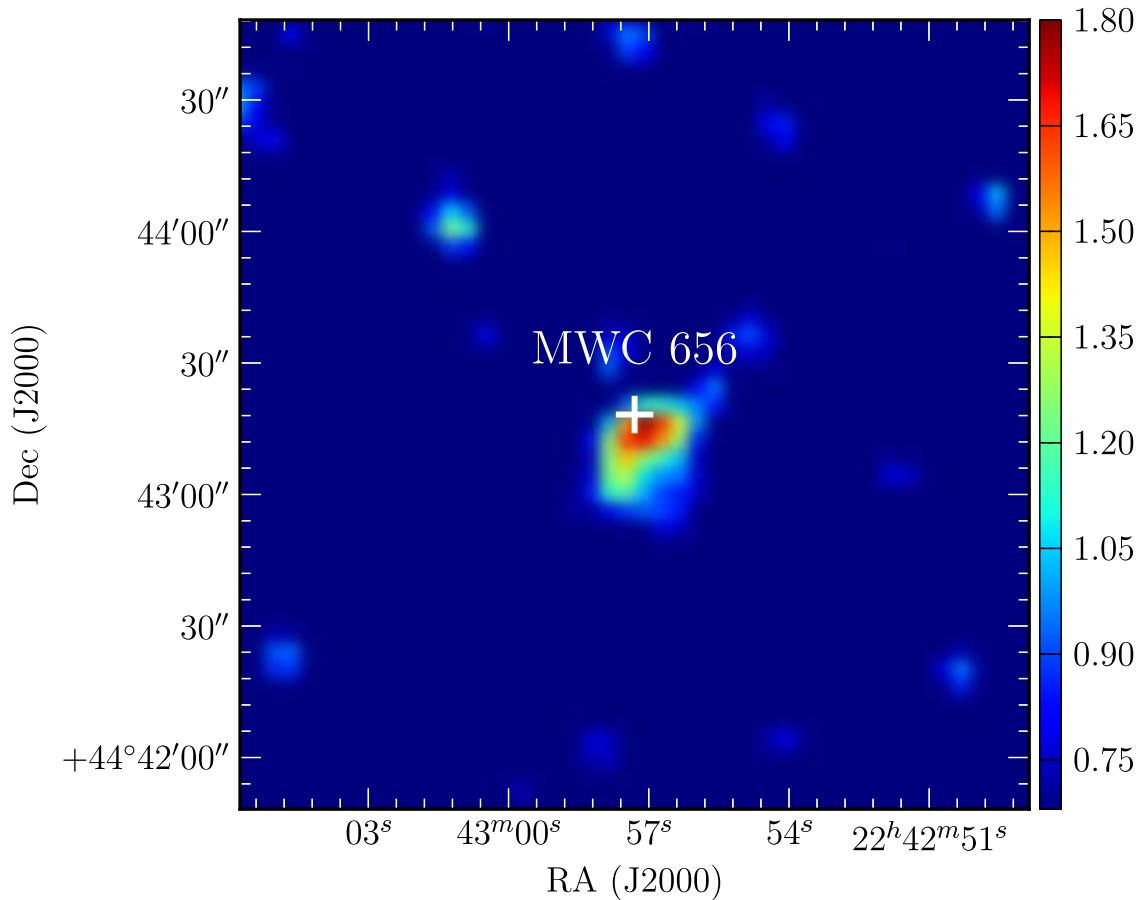
[2]The observation ID is 0723610201

Figure 7.1: EPIC-pn camera image at the position of MWC 656 in the 0.4–5.0 keV energy band smoothed using a gaussian interpolation with a 2″ kernel.

and MOS2) for the imaging observation. The analysis of the data was done using the *XMM-Newton* Science Analysis System (SAS) version 12.0.1 and the set of `ftools` from HEASOFT version 6.14[3]. In a first step we cleaned the event files of the three EPIC detectors removing the flaring high background periods. For this purpose we selected the Good Time Intervals (GTI) in which the count-rate for the most energetic events ($E \geq 10$ keV) was below the standard threshold for each detector. After this cleaning process, the observation time that remained in each of the three detectors was 10.1 ks, 13.4 ks and 13.5 ks for the pn, MOS1 and MOS2, respectively.

A search for sources was performed using the `edetect-chain` command in SAS, which concatenates a series of tasks that produce exposure maps, detector mask images, background maps, detected source lists and sensitivity maps. As a result, a list of detected sources, including MWC 656, was obtained, which contained count-rates, fluxes and po-

---
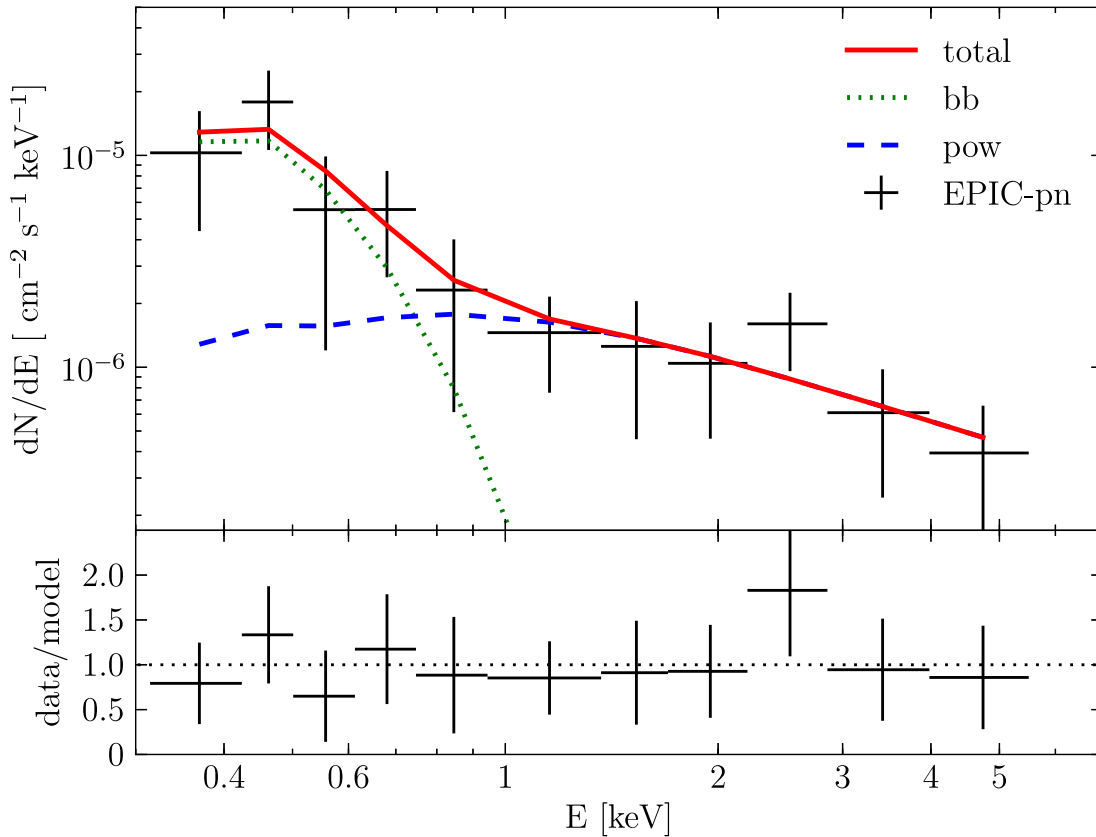
[3]`http://heasarc.gsfc.nasa.gov/`

Figure 7.2: MWC 656 *XMM-Newton* EPIC-pn spectrum in the 0.4–5.0 keV energy range (data points) over-plotted with the fitted absorbed black body (green dotted line) plus a powerlaw (blue dashed line) model. The red solid line represents the total flux. The lower panel illustrates the ratio between the observational data and the total model.

sitions for each detected source, among other information. We used the cleaned event files for spectral analysis. The source spectrum was extracted from a 30″ radius circle centered on the position of MWC 656 whereas the background spectrum was extracted from a source-free region in the same CCD chip, using a circle of 90″ radius. Response and anciliary files were obtained with the SAS tools `rmfgen` and `arfgen`, respectively.

7.3 X-ray results

We detect a faint source at 4.4σ c.l. coincident with MWC 656 (see Figure 7.1). The X-ray position is RA= $22^h42^m57.1^s$, Dec= $44°43'13''$ with a 3σ uncertainty radius of $7''$. This is compatible with the *Hipparcos* position of MWC 656 at 2.4σ. The source is only detected in the low energy range of the EPIC-pn detector, between 0.4 and 5.0 keV. In MOS1 and MOS2 instruments MWC 656 appears as a faint excess below 3σ c.l., probably

Table 7.1: X-ray spectral fit parameters of MWC 656

Model[a]	Parameters		$F(0.4 - 5.0 \text{ keV})/10^{-14}$ (erg cm^{-2} s^{-1})			Comments
	$k_\mathrm{B}T$ [keV]	Γ	thermal	non-thermal	total	
pow	–	1.9 ± 0.8	–	1.5 ± 0.2	1.5 ± 0.2	Not good below 1 keV
bb	0.12 ± 0.07	–	0.49 ± 0.05	–	0.49 ± 0.05	Not good above 1 keV
bb+pow	0.07 ± 0.04	1.0 ± 0.8	0.38 ± 0.06	1.5 ± 0.3	1.9 ± 0.4	Good fit (used in this Chapter)
diskbb+pow	0.09 ± 0.06	1.0 ± 0.8	0.42 ± 0.08	1.5 ± 0.2	1.9 ± 0.5	Good fit

Note. a: models correspond to powerlaw (pow), black body (bb) and multi-temperature disk black body (diskbb)

due to their lower effective area at these energies.

The EPIC-pn spectrum (see Figure 7.2) was conveniently binned so that there were at least 10 counts per bin. The binned spectrum was analyzed using XSPEC version 12.8.1 (Arnaud 1996). The low number of counts required the use of the C-stat statistic in the estimation of best-fit parameters and their associated uncertainties. In all fits we introduced a fixed interstellar photoelectric absorption with $N_\mathrm{H} = 1.4 \times 10^{21}$ cm^{-2} (Casares et al. 2014, based on $E(B - V) = 0.24$ and the relation by Bohlin et al. 1978; this same value is obtained after Dickey & Lockman 1990).

A powerlaw (pow) model fit yields a photon index $\Gamma = 1.9 \pm 0.8$, similar to that found in other BH XRBs. However, the model cannot fit the data below 1.0 keV. A black body (bb) model is also unable to reproduce the observed spectrum above 1.0 keV. For this reason we decided to fit the data with a model including two components: a black body plus a powerlaw. This fit yields $k_\mathrm{B}T = 0.07 \pm 0.04$ keV, photon index $\Gamma = 1.0 \pm 0.8$ and a total unabsorbed flux $F_{0.4-5.0 \text{ keV}} = (1.9 \pm 0.4) \times 10^{-14}$ erg cm^{-2} s^{-1}. The contribution of each of the two components to the total flux is $F_{\mathrm{bb}} = (0.38 \pm 0.06) \times 10^{-14}$ erg cm^{-2} s^{-1} and $F_{\mathrm{pow}} = (1.5 \pm 0.3) \times 10^{-14}$ erg cm^{-2} s^{-1}. A solution swapping the two components, with the powerlaw at low energies and the black body at higher energies, is also possible, although in this case the photon index is unconstrained. On the other hand, a fit using a multi-temperature disk black body (diskbb, Mitsuda et al. 1984) plus a powerlaw gives similar results. We summarize the results of the most relevant fits in Table 7.1, where the fluxes are unabsorbed. The uncertainties are quoted at 1σ level. The total fluxes obtained in the 0.4–5.0 keV energy range in all fits are compatible at 1σ level, resulting in values which are one order of magnitude lower than the upper limits obtained from previous *ROSAT* and *Swift*/XRT observations (Casares et al. 2014). It is clear from the spectral analysis that two components are required to fit our data (see Figure 7.2). The fit with a black body plus a powerlaw is more realistic and simple and we will consider it throughout the next sections.

We searched for a possible extension of the $0.4 - 5.0$ keV point source by adjusting radial profiles to the EPIC-pn image. However, no significant extension was found. We also searched for variability during the observation by obtaining a background subtracted

light-curve of the source region but no significant variability was found.

7.4 Discussion

Our detection of the X-ray counterpart of MWC 656 allows us to classify the Be/BH system as a HMXB, being it the first XRB of this type.

The spectrum is best fit with a model that includes a thermal and a non-thermal component, with the main flux contribution coming from the non-thermal component ($\sim$80%). Given the source distance of 2.6$\pm$0.6 kpc, the total X-ray luminosity is $L_{\mathrm{X}} = (1.5 \pm 0.8) \times 10^{31}$ erg s^{-1} in the 0.4–5.0 keV band. This luminosity represents $(2.8 \pm 2.0) \times 10^{-8} L_{\mathrm{Edd}}$ for the estimated range of BH masses of 3.8–6.9 M$_{\odot}$. The thermal and non-thermal contributions are $L_{\mathrm{bb}} = (3.1 \pm 1.5) \times 10^{30}$ erg s^{-1} and $L_{\mathrm{pow}} = (1.2 \pm 0.6) \times 10^{31}$ erg s^{-1}, respectively.

7.4.1 Origin of the thermal component

The X-ray spectrum in B-type stars is typically represented by a hot thermal component at about 1 keV or by the sum of two thermal components, one around 0.4 keV and another one around 2 keV (Nazé 2009). In our case the best fit yields a temperature of $k_{\mathrm{B}}T = 0.07 \pm 0.04$ keV which is not far from that observed in B-type stars. We can also compare the results of our fit with the correlation $L_{\mathrm{X}} \sim 10^{-7} L_{\mathrm{bol}}$ (see Berghoefer et al. 1997; Cohen et al. 1997), where L_{X} represents the thermal X-ray luminosity. The bolometric luminosity of MWC 656 is 7×10^{37} erg s^{-1}, considering $M_{\mathrm{V}} = -4.1$ and a bolometric correction of -1.8 according to Straizys & Kuriliene (1981). In our case, given the derived thermal X-ray luminosity, we find $L_{\mathrm{X}}/L_{\mathrm{bol}} = 4 \times 10^{-8}$, which places MWC 656 below the correlation quoted above, but still compatible with it given the large scatter. This result suggests that the thermal component of our X-ray spectrum arises from the hot wind of the Be star.

7.4.2 Origin of the non-thermal component

BH LMXBs display a positive correlation between the radio and X-ray luminosities which is thought to be due to an accretion disk-jet coupling. This coupling is invoked to explain the different state transitions observed in BH binary systems (Fender 2010). At the beginning of the outburst and during the outburst decay, the source is in a hard state (Remillard & McClintock 2006). This hard state is characterized by a powerlaw spectrum with photon index $\Gamma \sim 1.5$, a luminosity below 0.1 L_{Edd} and the presence of an active jet in the radio domain with an almost flat radio spectrum. The X-ray emission is non-thermal and thought to be due to comptonization in a corona near the BH (Zdziarski et al. 1998; Nowak & Wilms 1999) or to optically thin synchrotron emission from the base of the jet (Markoff et al. 2005). At the end of the outburst the X-ray emission decays again to a
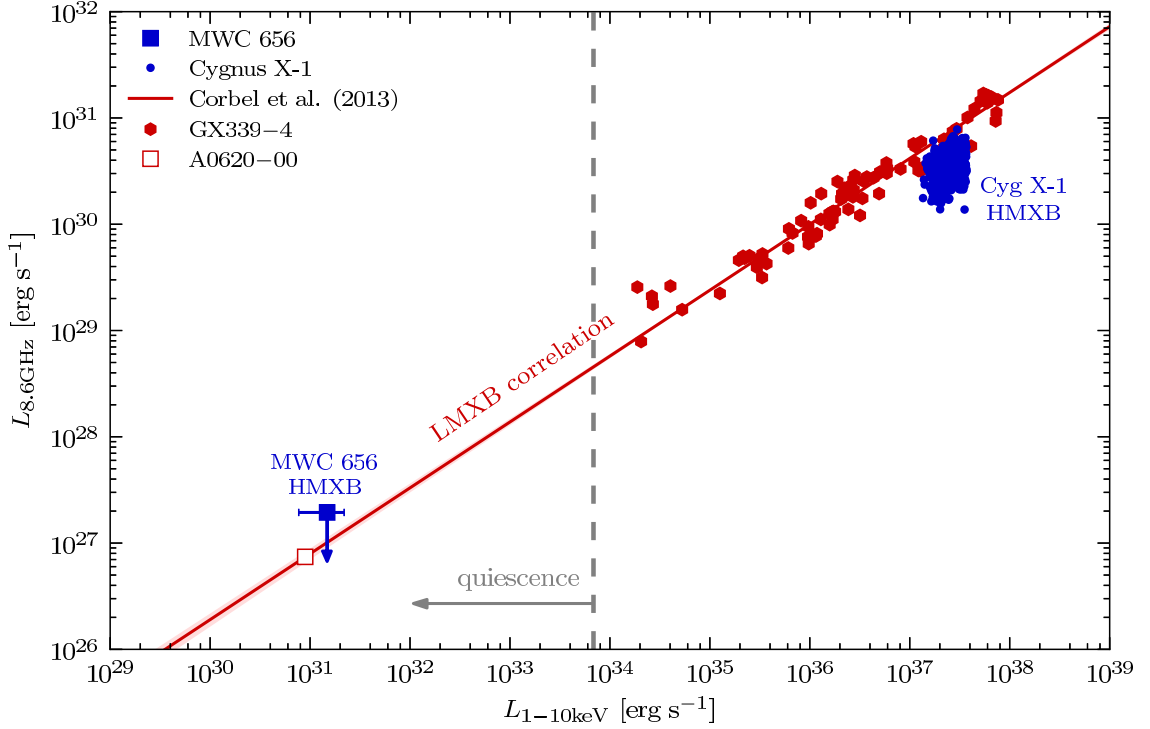
Figure 7.3: Radio versus X-ray luminosity diagram including the position of MWC 656 (blue square) according to non-simultaneous X-ray observation (this work) and the lowest radio flux density upper limit from Moldón (2012). The small blue dots indicate the region of the parameter space where Cygnus X-1 has been detected in the low/hard state (Gallo et al. 2012). We also plot the radio/X-ray correlation for BH LMXBs of Corbel et al. (2013) (red solid line plus light red shadow), together with data on the BH LMXBs GX 339-4 (red hexagons) and A0620-00 (empty red square) to display the luminosity range of real sources. The grey dashed line separates the quiescent state region (left) and the other states (right) according to the threshold set by Plotkin et al. (2013). The position of MWC 656 is very close to the one of the LMXB A0620-00 in quiescence, indicating that the radio/X-ray correlation might also be valid for BH HMXBs down to very low luminosities.

low/hard state below 0.01–0.04 $L_{\rm Edd}$ and eventually to a quiescent state below 10^{-5} $L_{\rm Edd}$ (Plotkin et al. 2013). The quiescent X-ray spectrum is reproduced by a powerlaw with an average photon index $\Gamma = 2.08 \pm 0.07$ (Plotkin et al. 2013). As in the low-hard state, the quiescent spectrum is non-thermal emission from the corona or the jet base, but slightly softer.

The non-thermal X-ray luminosity of MWC 656 in the 0.4–5.0 keV band is $L_{\rm X} = (2.2 \pm 1.5) \times 10^{-8} L_{\rm Edd}$ for the estimated BH mass of 3.8–6.9 $M_\odot$ (Casares et al. 2014). This luminosity is 3 orders of magnitude below the 10^{-5} $L_{\rm Edd}$ threshold from Plotkin et al. (2013), making our results compatible with MWC 656 being in quiescence.

In addition, the best fit model gives a photon index $\Gamma = 1.0 \pm 0.8$ which is roughly compatible with the results of Plotkin et al. (2013) for BH LMXBs in quiescence. Nevertheless, poor statistics in the spectrum prevent us to constrain the photon index of MWC 656.

7.4.3 MWC 656 within the BH radio/X-ray correlation

We can compare the X-ray flux obtained in this paper and the previous radio flux density upper limits with the radio/X-ray correlation from Corbel et al. (2013) (see Figure 7.3). The EVN radio flux density 3σ upper limits are in the range 30–66 μJy (Moldón 2012), although they are not simultaneous nor at the same orbital phase as our *XMM-Newton* observation. Converting the lowest radio flux density upper limit into luminosity we obtain $L_r < 2 \times 10^{27}$ erg s^{-1} at 8.6 GHz assuming a flat radio spectrum. The X-ray luminosity corresponding to the contribution of the powerlaw component of our fit, once extrapolated to the 1.0–10 keV energy band is $L_X = (1.5 \pm 0.7) \times 10^{31}$ erg s^{-1}. MWC 656 is located in the lower-left side of the luminosity diagram (see Figure 7.3), very close to A0620$-$00 and just above the correlation by Corbel et al. (2013). The expected radio luminosity considering our X-ray flux measurement and the Corbel et al. (2013) correlation is $L_r = (9.2 \pm 2.9) \times 10^{26}$ erg s^{-1}, which translates into a radio flux density of $S_\nu = 13 \pm 7$ μJy at 8.6 GHz (or 9 ± 6 μJy using the correlation from Gallo et al. 2012). The quoted uncertainties account for X-ray flux, distance and correlation parameters uncertainties. This result is not far from the upper limits we have obtained up to now.

Gallo (2007) found a significant number of outliers in the original radio/X-ray best-fitting relation (Gallo et al. 2003), indicative that there might be a second track in the high X-ray luminosity region with a steeper slope. Coriat et al. (2011) suggested that these two tracks may collapse into a single track for X-ray luminosities below $3 \times 10^{-4} L_{Edd}$, as it seems to occur in the case of H1743–322. Gallo et al. (2012) studied the case in detail adding newly discovered sources, as well as new data from well-studied ones, and concluded that the two tracks scenario better explains the observational data. The radio flux density upper limits for MWC 656 are consistent with both tracks (assuming the lower one also extends towards lower X-ray luminosities). For the lower track the expected radio luminosity would be undetectable by the current radio telescopes.

So far, the only known HMXB containing a confirmed BH in our Galaxy is Cygnus X-1. This system has an X-ray luminosity in the range $(1.0–7.0) \times 10^{37}$ erg s$^{-1} \equiv (0.8–3.0) \times 10^{-2}$ L_{Edd} for a ~ 15 M$_\odot$ BH in the 1$-$10 keV range (Gallo et al. 2012; but see Zdziarski 2012). Its radio and X-ray fluxes also fulfil the radio/X-ray correlation during the hard state, similar to what is observed in LMXBs (Zdziarski 2012). In contrast, the low X-ray luminosity of MWC 656 makes it comparable to the faintest LMXBs, such as A0620–00 (see Figure 7.3 and Plotkin et al. 2013), allowing to study accretion processes and the accretion/ejection coupling at very low luminosities also for BH HMXBs.

7.5 Conclusions

We have detected the X-ray counterpart of the first BH orbiting a Be star, MWC 656, confirming it to be an XRB and thus classifying it as a HMXB. Due to the low number of counts we cannot fully characterize its spectrum, although a thermal and non-thermal components seem to be required to explain the low-energy and high-energy part of the X-ray spectrum, respectively. These two components are interpreted as the contribution from the hot wind of the Be star and the emission close to the black hole, respectively. The non-thermal X-ray flux translates into a luminosity well below the threshold set by Plotkin et al. (2013) for quiescent BH binaries. Using the EVN radio flux density upper limits and our X-ray luminosity we find that MWC 656 is located in the lower-left side of the luminosity diagram and just above the correlation by Corbel et al. (2013), in a region which may be consistent with it. Consequently, the radio/X-ray correlation might also be valid for BH HMXBs. In this context, MWC 656 will allow the study of accretion processes and of accretion/ejection coupling at very low luminosities for BH HMXBs. Further deep X-ray observations are needed to better characterize the spectrum and constrain the spectral parameters to allow a better interpretation. Deep simultaneous radio observations are needed to study the low luminosity accretion/ejection coupling in BH HMXBs.

8

Search for VHE emission from MWC 656 with the MAGIC Telescopes

8.1 Introduction

MWC 656 (= HD 215227) is the only known binary system formed by a Be star and a black hole (Casares et al. 2014). In Chapter 7 we presented our *XMM-Newton* observations of MWC 656 which allowed us to establish this binary system as the first Be/BH XRB. We studied MWC 656 within the context of the radio/X-ray correlation found for LMXBs (Gallo et al. 2012; Corbel et al. 2013) finding that it displays an X-ray flux that, together with the radio ULs from Moldón (2012), may be compatible with the correlation and comparable to the faintest BH LMXBs.

In this Chapter we present the results of the observations of MWC 656 carried out with the MAGIC Telescopes and compare them to the ones of Cygnus X-1, the only other known HMXB in our Galaxy hosting a BH, which could be a source of VHE gamma rays (Albert et al. 2007b). Our observations do not show any indication of a signal at the position of MWC 656 and flux upper limits are derived.

8.2 Observations

The observations of MWC 656 were performed in wobble mode in two different epochs: in 2012 May-June and in 2013 June, using the MAGIC Telescopes on the Canary island of La Palma (see Appendix A for more details on the telescope), from where MWC 656 is visible at zenith angles greater than 16°..

8.2.1   2012 observations

The observations from 2012 were performed in mono mode, as one of the telescopes was not operational. The integral sensitivity for mono observations above 100 GeV is about 2.5% of the Crab Nebula flux in 50 hours. MWC 656 was observed for a total of 23.4 hours, for zenith angles between 22° and 51° under dark conditions. The observations taken in May comprise the orbital phase range 0.83–0.95 (see Figure 8.1). In June the observations covered orbital phases after the periastron passage, between phase 0.21 and 0.27, which correspond to orbital phases where gamma-ray binaries, as LS I +61 303 or HESS J0632+057 exhibit emission (usually around 0.2–0.45 orbital phases after periastron; Albert et al. 2009; Aleksić et al. 2012a). After a selection of good-quality data, a total of 21.3 hours of effective time remained for the 2012 sample.

8.2.2   2013 observations

The observations of MWC 656 in 2013 were performed between June 3–5, covering a range of orbital phases between 0.05–0.09 (see Figure 8.1), very close to periastron, in stereo mode, which allows us to achieve a sensitivity of 0.7% of the Crab Nebula flux above 100 GeV in 50h (Sitarek et al. 2013). The source was observed for a total of ∼3h during this period in dark conditions covering a zenith angle range between 28° and 45°. The observation on June 4 was taken almost simultaneously with the *XMM-Newton* observation, which results are discussed in Chapter 7. The quality of this data set is good and almost all runs survived the quality selection.

8.3   Data Analysis

The data analysis was performed with the standard MAGIC analysis and reconstruction software, MARS (Bretz et al. 2003), using the appropriate methods for mono and stereo data. See Appendix A for a detailed description of the analysis chain. The optimization of the cuts to apply in the analysis process could not be performed in either of the observation periods as no Crab Nebula data set with similar conditions and telescope configuration was available for them. For non-detections we derived flux ULs using the method in Rolke et al. (2005) with a statistical uncertainty of 30%. Three powerlaw photon indexes have been used to compute the ULs (Γ = 2.0, 2.5, 3.0) although the results do not differ significantly.

8.4   Results

Data from 2012 and 2013 have been analyzed separately and no detection has arisen from any of the observed epochs.
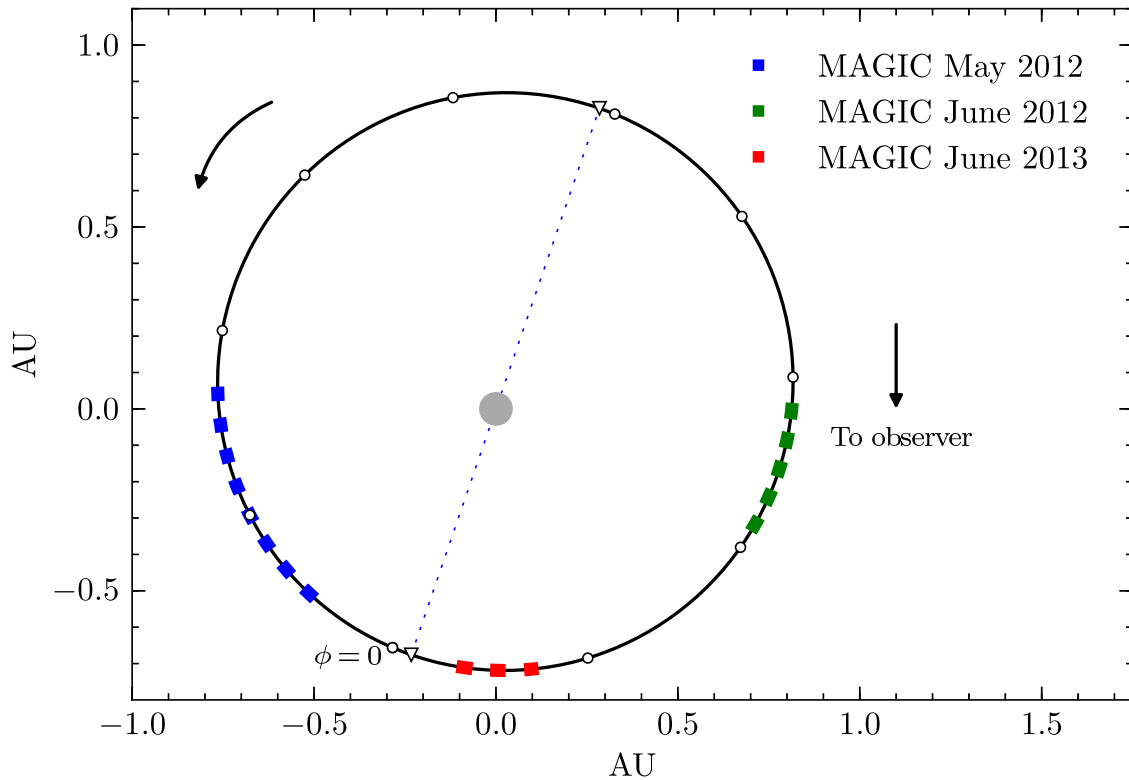
Figure 8.1: Sketch of the orbit of MWC 656. Triangles mark the position of the periastron and the apastron. The MAGIC observations are overplotted on top of the orbit. The orbit, the size of the star and the duration of the observations with MAGIC are scaled to the real values.

For both datasets we have computed differential flux ULs at 95% c.l. in 8 energy bins, from 130 GeV to 7 TeV (see Figure 8.2 and Table 8.1), assuming three different spectral indexes, as we still do not know how this source behaves at VHE. We have also computed integral 95% c.l. flux ULs above 300 GeV. In the case of the 2012 data sample, we have computed three different integral flux ULs: one for the whole dataset, one for May and another for June data. Dividing the 2012 data sample between May and June we obtain two sets of very differentiated orbital phase ranges, from 0.83 to 0.95 and from 0.21 to 0.27, respectively. Integral ULs for the 2013 data sample have been also computed. All the integral ULs have been computed also for 3 different photon indexes and the results are summarized in Table 8.2.

No excess is found and the significance (following the definition of Li & Ma 1983) is about 0.5 σ and 1.2 σ for the 2012 and 2013 samples of MWC 656, respectively. No signal was neither detected in a day-to-day nor in a phase-to-phase analysis, being always the significance less than 1.7σ.
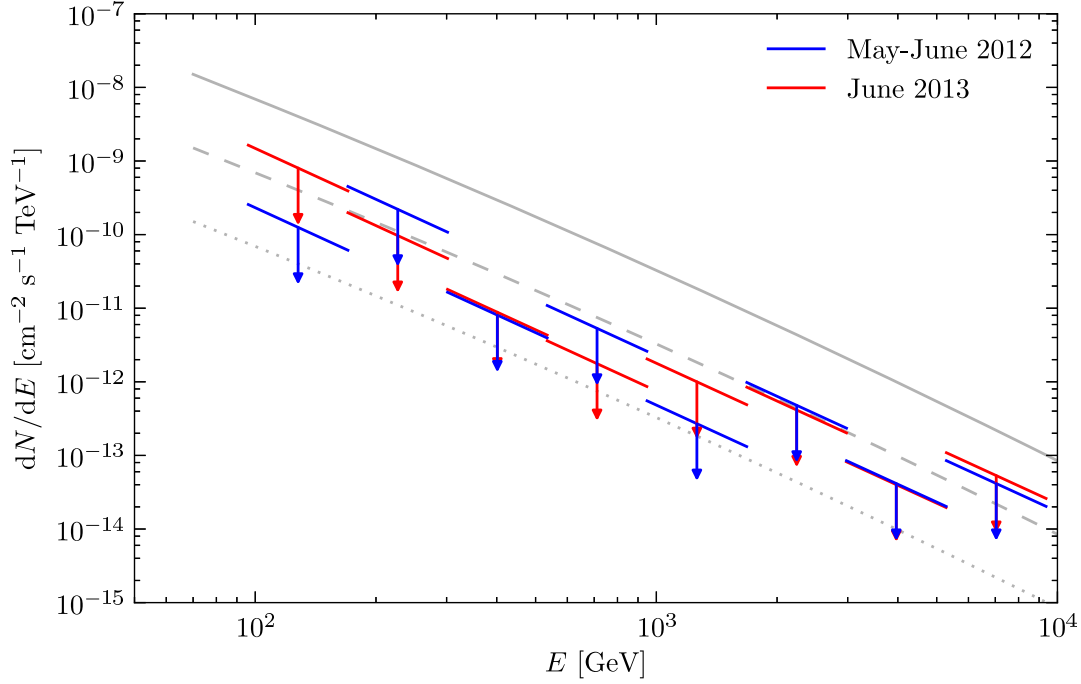
Figure 8.2: Differential ULs spectrum of MWC 656 (95% c.l.). The slope of the bars indicates the assumed power-law photon index $\Gamma = 3.0$ for both data sets. Crab Nebula spectrum is plotted for comparison, as well as its 10% (dashed) and 1% (dotted) fractions.

E_{min} [GeV]	E_{max} [GeV]	Diff. UL [TeV^{-1}cm^{-2}s^{-1}]	
		2012	2013
96.1	170.1	1.3×10^{-10}	8.0×10^{-10}
170.1	301.6	2.2×10^{-11}	9.7×10^{-11}
301.6	534.5	8.1×10^{-12}	8.8×10^{-12}
534.5	948.2	5.3×10^{-12}	1.8×10^{-12}
948.2	1681.5	2.7×10^{-13}	1.0×10^{-12}
1681.5	2978.7	4.8×10^{-13}	4.1×10^{-13}
2978.7	5286.9	4.1×10^{-14}	4.0×10^{-14}
5286.9	9367.3	4.2×10^{-14}	5.3×10^{-14}

Table 8.1: Differential flux ULs (95% c.l.) for the whole 2012 and 2013 data sets. We only show the results for $\Gamma = 3$ as the results for the other two photon indexes are similar.

8.5 Discussion and conclusions

We have not detected MWC 656 in any of the periods in which the system has been observed. We obtained flux ULs for different data subsamples assuming three distinct

| Γ | 2012 | | | | | | 2013 | |
| | All | | May | | June | | June | |
	(cm^{-2} s^{-1})	(%c.u.)	(cm^{-2} s^{-1})	(%c.u.)	(cm^{-2} s^{-1})	(%c.u.)	(cm^{-2} s^{-1})	(%c.u.)
2.0	1.7×10^{-12}	1.4	2.4×10^{-12}	1.9	2.3×10^{-12}	1.8	1.2×10^{-12}	0.9
2.5	1.8×10^{-12}	1.5	2.6×10^{-12}	2.1	2.3×10^{-12}	1.9	1.3×10^{-12}	1.0
3.0	1.8×10^{-12}	1.5	2.6×10^{-12}	2.1	2.3×10^{-12}	1.9	1.3×10^{-12}	1.0

Table 8.2: Integral flux ULs($E > 300$ GeV) of MWC 656 (95% c.l.).

spectral indexes.

The MAGIC observation carried out in 2013 June 4 was scheduled contemporaneously with an *XMM-Newton* observation from which we revealed that MWC 656 is indeed a HMXB. The source was in the quiescent state during the observation (see Chapter 7 for details). We computed flux ULs in 8 energy bins for this night assuming the same three spectral indexes, which are similar to those computed for the overall 2013 data set. The integral flux UL for this night is F($E > 300$ GeV)$< 1.6×10^{-12}$ cm^{-2} s^{-1} (1.3% c.u.). There is no information about the X-ray state of the binary system during the 2012 observation.

As explained in Chapter 7, XRBs in the quiescent state show a hard X-ray spectrum and very faint or undetectable radio emission. The X-ray spectrum of MWC 656 is fitted with a black body plus a powerlaw, with $\sim 80\%$ of the total flux coming from the non-thermal component. The non-thermal X-ray luminosity of MWC 656 is $L_{\mathrm{nt}}(0.4-5$ keV) $= 1.2\times10^{31}$ erg s^{-1} ($\equiv (2.2\pm1.5)\times10^{-8}L_{\mathrm{Edd}}$) and is interpreted as the contribution coming close to the black hole. Given the low X-ray luminosity, it is expected that the energy budget of the system is not enough to accelerate particles that produce detectable VHE emission.

The only other known HMXB in our Galaxy containing a BH is Cygnus X-1. This system was observed by the MAGIC Telescope in mono observation mode in 2006 (Albert et al. 2007b). A hint of signal was found in these observations at a 4.9σ c.l. (4.1σ post-trials), being it the first evidence of VHE gamma-ray emission arising from a BH HMXB. This gamma-ray excess coming from Cygnus X-1 was detected during a hard X-ray flare registered by the *INTEGRAL*, *Swift* and *RXTE* satellites, when the system was at orbital phase 0.91 (being phase 0 the moment when the BH is behind the companion star). It was suggested that the reported hard and soft X-ray photons were produced in different regions of the system, and that hard X-rays and gamma rays could be produced in regions linked by the collimated jet, such as the base of the jet and the interaction region between the jet and the stellar wind, respectively (Albert et al. 2007b). At this orbital phase, however, one would not expect enhanced VHE gamma-ray emission from the vicinity of the compact object due to the expected high absorption in the stellar photon field (Bednarek & Giovannelli 2007). This fact suggested that the hint of detection was originated far from the compact object.

In contrast, the case of MWC 656 is different, as it does not seem to be as active as

Cygnus X-1 in X-rays, displaying a flux ~ 5 orders of magnitude lower than Cygnus X-1. During the simultaneous X-ray and VHE observations MWC 656 was in the quiescent state, at which the accretion disk is truncated at several gravitational radii from the BH. The MAGIC observations took place at orbital phases at which the compact object is almost in front of the companion star and the expected absorption due to the companion's photon field should be low. However, even assuming a flaring state and a ratio between X-rays and VHE gamma rays of $F_{\rm X}/F_{\rm TeV} \sim 8.5$, equal to the one observed in 2006 for Cygnus X-1, the expected VHE emission would be $\sim 0.0005\%$ of the Crab Nebula flux, well below the detectable levels for the current IACTs and even for CTA.

In conclusion, we have observed the first Be/BH binary system with the MAGIC Telescopes and we have not detected it. There is no information about the state of the binary system during the 2012 MAGIC observations. During the 2013 observations, the source was in the quiescent state as stated from the simultaneous X-ray observations. Compared to Cygnus X-1, MWC 656 displays a much weaker X-ray emission and thus the expected VHE emission, if any, will be undetectable by the current and future IACTs.

9

Detection of VHE gamma-rays from HESS J0632+057 during the 2011 February X-ray outburst with the MAGIC Telescopes

9.1 Introduction

The newest generation of IACTs established a new source class, the gamma-ray binaries. Among the few known objects of this class LS I +61 303, LS 5039 and PSR B1259−63 are regularly detected at very high energy (VHE, $E > 100$ GeV) gamma-rays. All of these three systems show variable or even periodic VHE gamma-ray emission, and are spatially unresolvable by the current generation of IACTs (Aharonian et al. 2005b; Albert et al. 2006; Aharonian et al. 2006; Albert et al. 2009).

HESS J0632+057 was discovered as an unidentified point-like VHE gamma-ray source but was considered to be a gamma-ray binary candidate because of its spatial coincidence with the Be star MWC 148 (Aharonian et al. 2007; Hinton et al. 2009). The system was not detected in VHE gamma-rays by VERITAS in an observation campaign from 2006 to 2009 (Acciari et al. 2009). These sparsely sampled measurements yielded flux upper limits (above 1 TeV) significantly below the previous detections, thus suggesting that HESS J0632+057 was variable in VHE gamma-rays. Since all variable galactic VHE gamma-ray sources known to date are associated with binary systems[1], HESS J0632+057 was a very good binary candidate.

---

[1] The Crab Nebula is variable at GeV energies, but no confirmed TeV variability has been measured up to now and thus it is not counted among the variable VHE gamma-ray sources.

9. Detection of VHE gamma-rays from HESS J0632+057 during the 2011 February X-ray outburst with the MAGIC Telescopes

Measurements in soft X-rays with *XMM-Newton* detected an X-ray source (XMMU J063259.3+054801) at the position of MWC 148 (Hinton et al. 2009). The X-ray emission is well described by a hard power-law spectrum with photon index $\Gamma = 1.26 \pm 0.04$, consistent with emission of synchrotron radiation from VHE electrons, although a multi-temperature spectral model can also reasonably describe the data. Furthermore, the X-ray source showed a variable flux, without changing the spectral shape. A similar behavior is seen, e.g., in the gamma-ray binary LS I +61 303 (e.g. Anderhub et al. 2009). From 2009 January to 2009 May extensive X-ray observations with *Swift*/XRT detected the source but at a different flux level and with a softer photon index (Falcone et al. 2010). New X-ray light curves from HESS J0632+057 obtained with *Swift*/XRT from 2009 to 2011 show a periodicity of $P = 321 \pm 5$ days (Bongiorno et al. 2011). These measurements also provided evidence for hardness ratio changes with orbital phase. The periodic X-ray emission was a strong evidence for HESS J0632+057 being a binary system. *Chandra* high time resolution X-ray measurements during the 2011 February X-ray outburst have been used to search for pulsed X-ray emission, but none was detected. Thus the nature of the compact companion of MWC 148 remains unknown (Rea & Torres 2011).

The search for a radio counterpart of HESS J0632+057 started in 2008 with the Very Large Array (VLA) and the Giant Metrewave Radio Telescope (GMRT) at 5 and 1.28 GHz, respectively. These measurements exhibited an unresolved radio source within the position uncertainties of the VHE gamma-ray source and the Be star MWC 148 (Skilton et al. 2009). No extended structures beyond the two arcsecond resolution were detected. A flux increase in the 5 GHz band from 0.19 ± 0.04 to 0.41 ± 0.04 mJy showed the variability of the source on timescales of at least one month. The radio data was well described by a power law spectrum with energy spectral index $\alpha = -0.6 \pm 0.2$ using non-simultaneous data from 1.28 GHz and 5 GHz. During the 2011 February X-ray outburst very high resolution European Very Long Baseline Interferometry Network (EVN) observations revealed a point-like source coincident with the Be star MWC 148 within uncertainties. This point-like source evolved into an extended source 30 days later with a projected size of about 75 AU (assuming a distande of 1.5 kpc) (Moldón et al. 2011). The peak of the emission was displaced 21 AU between runs, being this displacement bigger than the orbit size (semi-major axis ~ 2.4 AU). The brightness temperature of the source was above 2×10^6 K hinting to a non-thermal origin of the particles producing the radio emission. The morphology, size, and displacement on AU scales were similar to those found in the other gamma-ray binaries, supporting a similar nature for HESS J0632+057 (Moldón et al. 2011). Further high resolution measurements will be needed to understand possible morphological changes in the radio structures along with the orbital phase.

Optical radial velocity measurements on MWC 148 yielded no significant variations at that time and simulations yielded a lower limit on the possible period of the system of $P > 100$ days compatible with the period found later in X-rays (Aragona et al. 2010). Finally, radial velocity measurements with the Liverpool telescope obtained from 2008 to

2011 have proven the binary nature of HESS J0632+057/MWC 148. Fixing the orbital period to 321 days as obtained from the X-ray measurements by Bongiorno et al. (2011) these measurements provide for the first time the orbital parameters of the binary system. The compact object orbits MWC 148 on a highly eccentric ($e = 0.83 \pm 0.08$) orbit where the periastron passage occurs at phase $\phi_{\mathrm{per}} = 0.967 \pm 0.008$ using $T_0 = $ MJD 54857.0 (Casares et al. 2012).

In this Chapter, we present the VHE gamma-ray measurements of HESS J0632+057 by MAGIC from 2010 October to 2011 March. In particular we detect VHE gamma-rays during an X-ray outburst in 2011 February and measure for the first time the spectrum down to 140 GeV[2].

9.2 Observations

The observations of HESS J0632+057 were performed using the MAGIC telescopes on the Canary island of La Palma (see Appendix A for more details on the telescope), from where HESS J0632+057 is observable at zenith angles above 22°. We observed HESS J0632+057 between 2010 October and 2011 March for a total of 10.6 hours (see Figure 9.1). All observations were carried out under moonlight conditions and at zenith angles from 22 to 50°. The source was observed for several nights in each month and each of these observation sets are separated by about 20 days. This strategy maximizes the possibility to detect emission from HESS J0632+057 because the long orbital period and the possibility that the system be active only during a short period of its orbit, i.e. one observation cycle. Due to bad weather no data were recorded in 2010 November and 2011 January.

9.3 Data Analysis

The data analysis was performed with the standard MAGIC analysis and reconstruction software MARS (Bretz et al. 2003).

The cuts used for producing the θ^2-plot for the detection were optimized on a Crab Nebula data sample to yield the best sensitivity and have a higher energy threshold compared to the cuts used to produce the spectrum. For the light curve and integral flux calculations we choose a conservative energy threshold of $E_{\mathrm{th}} = 200$ GeV, while the spectrum shows reconstructed signals down to 136 GeV. Note that the systematic uncertainties at the lowest energies dominate the total measurement uncertainties. Using a higher energy threshold, 200 GeV, guarantees smaller systematic uncertainties for the light curve and thus yields a better comparison to measurements from other instruments.

---

[2]The analysis and results detailed in this Chapter were published in Aleksić, J., et al. (2012) (P. Munar-Adrover as corresponding author), ApJ Letters 754, L10.
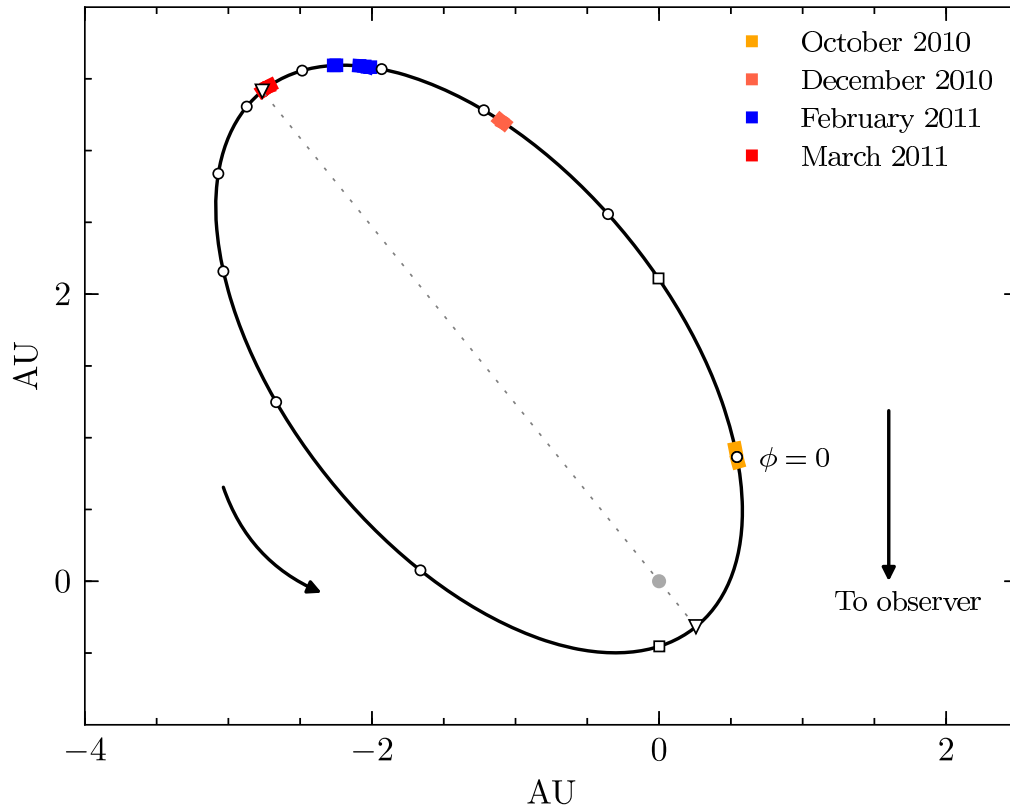
Figure 9.1: Sketch of the orbit of HESS J0632+057 . White circles mark orbital phases in steps of 0.1 . Triangles mark the position of the periastron and the apastron, and squares mark the position of inferior and superior conjunctions. The MAGIC observations are overplotted on top of the orbit. The orbit, the size of the star and the duration of the observations with MAGIC are scaled to the real values.

9.4 Results

We detect VHE gamma-ray emission from the HESS J0632+057 data set recorded in 2011 February, at orbital phase ∼0.3, with a significance (following the definition of Li & Ma 1983) of 6.1σ in 5.6 hours (see Figure 9.2). The VHE gamma-ray source is not resolved by MAGIC and its extension must be smaller than the MAGIC point spread function, whose Gaussian sigma is 0.09 deg above 200 GeV. We obtain an integral flux of $F(E > 200\text{GeV}) = (8.8 \pm 1.7_{\text{stat}} \pm 2.1_{\text{syst}}) \times 10^{-12}$ ph cm^{-2} s^{-1} which corresponds to about 4% of the Crab Nebula flux. Previously reported detections (Aharonian et al. 2007) measured the flux only above 1 TeV but agree well within the statistical uncertainties of our measurements when their spectrum is extended to our lower energy threshold. Thus we conclude that during our observations, HESS J0632+057 exhibited similarly intense VHE emission to the previously detected active VHE gamma-ray episodes (Aharonian
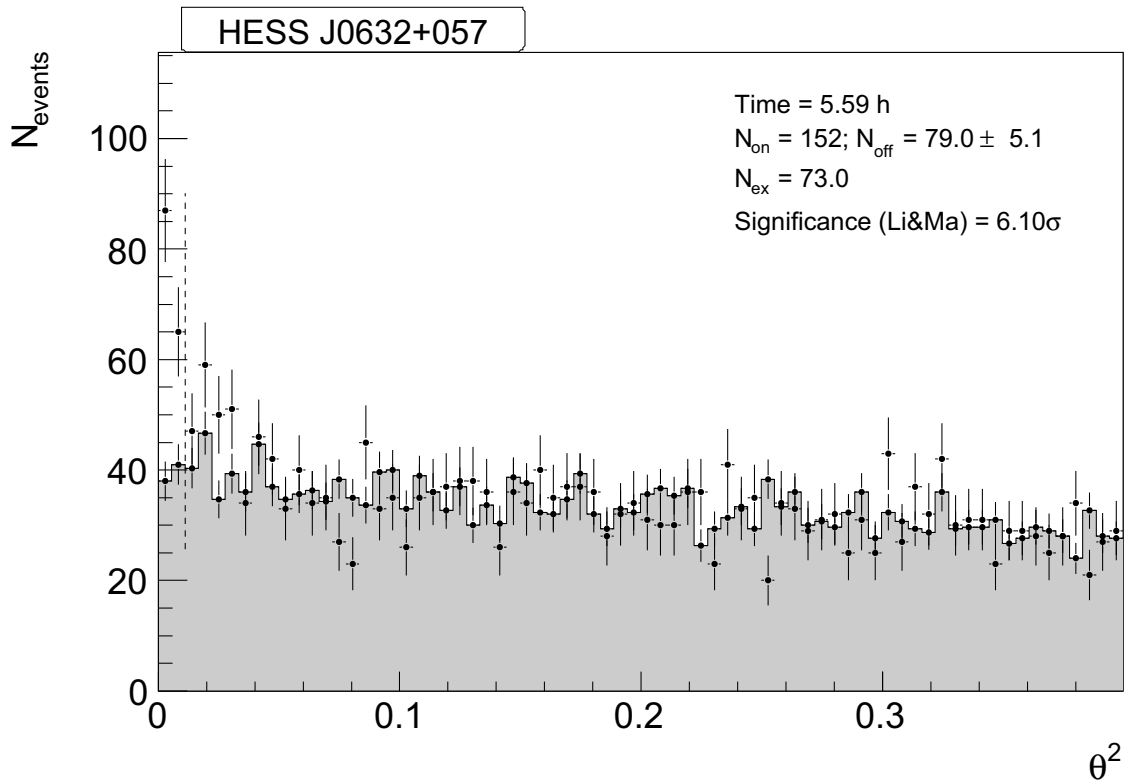
Figure 9.2: The squared angular distance between pointing direction of the shower and the source position (θ^2-plot) for the position of HESS J0632+057 (points) and the simultaneous determined background regions (grey shaded histogram) for the entire 2011 February MAGIC data set. The significance is calculated according to Li & Ma (1983). N_{on} is the number of events at the source position, N_{off} is the number of background events, N_{ex} is the number of excess events ($N_{\mathrm{ex}} = N_{\mathrm{on}} - N_{\mathrm{off}}$).

et al. 2007).

The system was only detected in the 2011 February data during the X-ray outburst observed by *Swift*. No indication of significant emission was found in the data from 2010 October, 2010 December or 2011 March. We denote these three months as the *non-detection period* (NDP). The integration time in the individual months of the NDP is, however, relatively short compared to the 2011 February and we combine the NDP to have the highest possible sensitivity for a baseline VHE flux. We obtain a flux upper limit for the NDP of $F(E > 200\mathrm{GeV}) < 3.7 \times 10^{-12}$ ph cm^{-2} s^{-1} at the 95% confidence level following the method suggested by Rolke et al. (2005). Our flux upper limit excludes a baseline emission down to the level of 1.7% of the Crab Nebula flux. No individual night during the quiescent gamma-ray state shows any indication of a signal.

We show in Figure 9.3 the obtained light curve above 200 GeV of HESS J0632+057 for the nightly averages. The VHE gamma-ray source exhibits variability timescales of about
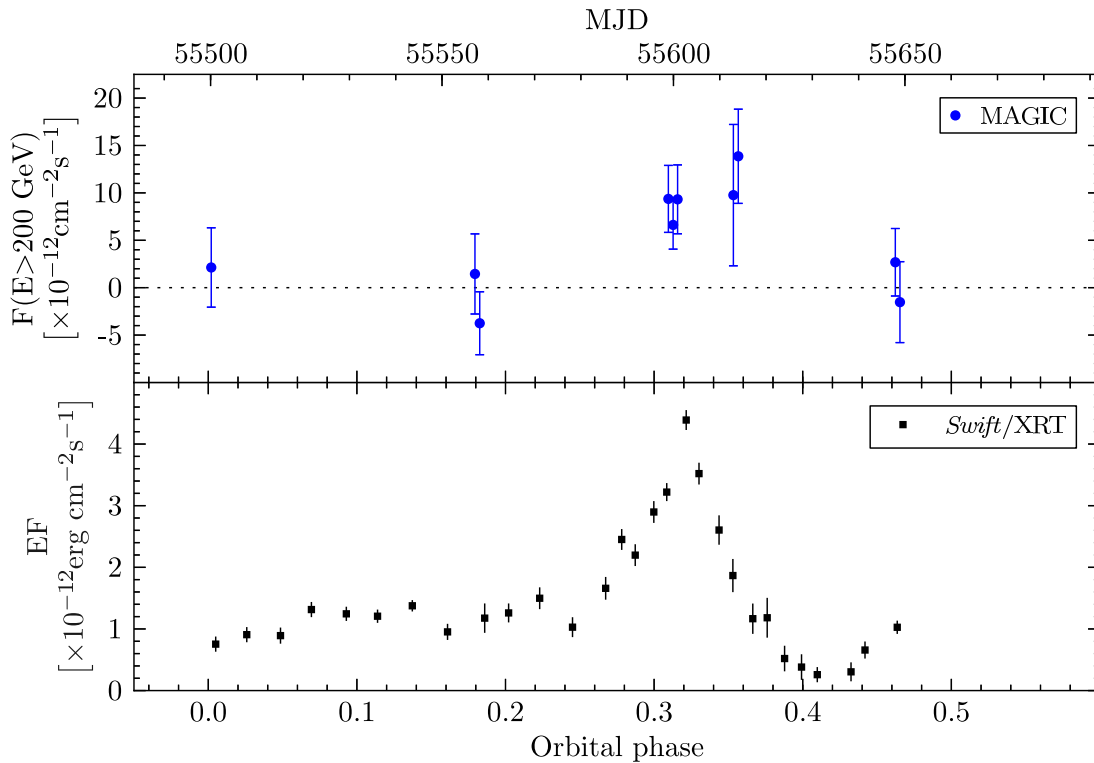
Figure 9.3: The light curve of HESS J0632+057 above 200 GeV is shown in blue for the MAGIC observations (upper panel) and the *Swift*/XRT data between 2 and 10 keV (lower panel) during the same orbital cycle as the MAGIC data in black. Significant emission in VHE is found only in 2011 February for the duration of about one month contemporary to the X-ray outburst. No variability in VHEs is seen during the active state. All error bars show the one-sigma statistical uncertainties.

one month. Faster variability is possible but to detect it a denser sampling of the LC is needed. However, no short timescale (days) variability is observed during the period of gamma-ray activity in 2011 February. Under the assumption that there is no short-time variability in the time period when no VHE gamma-ray emission is detected we conclude that the system shows flux variations of at least a factor of two between its quiescent and active state and that the active state must last between 20 and 80 days in the VHE regime.

A correlation of the VHE gamma-ray emission with the 2011 February X-ray outburst is suggestive but can not be proven statistically with our sparsely sampled light curve. More extensive observations in VHEs are needed for individual night correlation studies. Note that only in the time of high X-ray activity the system was detected by MAGIC. Whereas the X-ray light curve shows a clear peak shape for the outburst, the VHE light curve during the gamma-ray activity is compatible with a constant flux. Whether this constant gamma-ray flux is an artifact of the sparse sampling or a real characteristic of
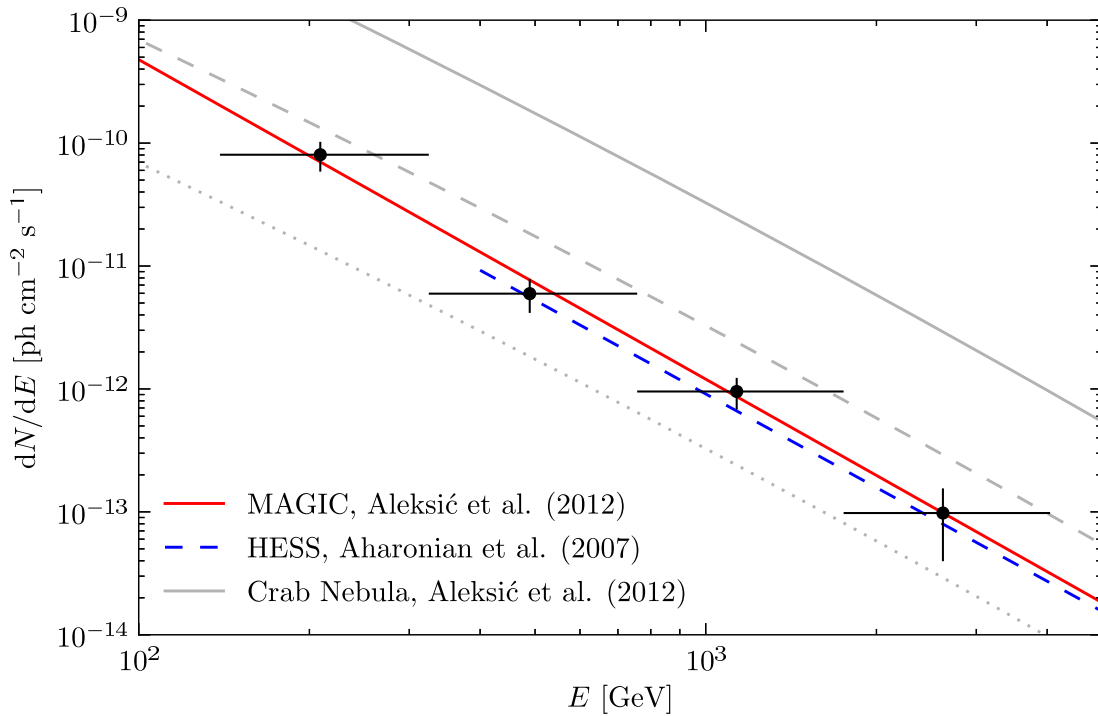
Figure 9.4: Differential energy spectrum of HESS J0632+057 between 136 GeV and 4 TeV. The horizontal error bars represent the bin width whereas the vertical ones show the one-sigma statistical uncertainty. The spectrum is well described by the fitted simple power law with $\Gamma = 2.6 \pm 0.3_{\text{stat}} \pm 0.2_{\text{syst}}$ shown as the red line. The dashed (blue) line is the spectrum obtained by HESS between 2004 March and 2006 March, and is in good agreement with our measurement. Crab Nebula spectrum is plotted for comparison, as well as its 10% (dashed) and 1% (dotted) fractions.

the outburst cannot be determined with these limited data. Note that a similar peak profile as in the X-ray outburst could be present in the VHE light curve.

We obtained a spectrum from the 2011 February data set and it is compatible with a simple power law (see Figure 9.4) with photon spectral index $\Gamma = 2.6 \pm 0.3_{\text{stat}} \pm 0.2_{\text{syst}}$ and normalization $(1.2 \pm 0.3_{\text{stat}} \pm 0.2_{\text{syst}}) \cdot 10^{-12}$ TeV^{-1} cm^{-2} s^{-1}. The measured photon index is in very good agreement with the one previously published by HESS ($\Gamma = 2.53 \pm 0.26_{\text{stat}} \pm 0.2_{\text{syst}}$), although their spectrum was obtained at energies above 400 GeV (Aharonian et al. 2007). No indication of a turnover is found in the newly opened energy range by MAGIC.

9.5   Discussion

The VHE gamma-ray data obtained during the periodic X-ray outburst of HESS J0632+057 that took place during 2011 February suggests that the VHE light curve shows similar out-

9. Detection of VHE gamma-rays from HESS J0632+057 during the 2011 February X-ray outburst with the MAGIC Telescopes

Middle Time (MJD)	Obs. Time (min)	Phase	Significance (pre-trial)	Flux 10^{-12} (ph cm^{-2} s^{-1})
55500.141	45	0.00	0.5	2.1±4.2
55557.102	14	0.181	0.4	1.4±4.2
55558.134	88	0.184	-1.1	-3.8±3.3
55598.880	91	0.311	2.8	9.4±3.5
55599.903	133	0.314	2.7	6.6±2.6
55600.873	61	0.317	2.8	9.3±3.6
55612.920	14	0.355	1.5	9.8±7.5
55613.982	54	0.358	3.0	13.9±5.0
55647.899	112	0.463	0.8	2.7±3.6
55648.900	55	0.467	-0.4	-1.5±4.3

Table 9.1: Observation time, orbital phase, integral flux (above 200 GeV). All errors are statistical only. We estimate an additional systematic uncertainty of about 40%. The systematic uncertainty is only important in case of comparing between different experiments.

bursts like the X-ray light curve. The detection of VHE gamma-ray emission only during the X-ray outburst suggests a common origin although our data are too sparsely sampled to allow night to night correlation studies. The MAGIC detection of the source during the peak of the X-ray outburst yielded a similar flux level and energy spectrum as those obtained by HESS four years before (Aharonian et al. 2007). Similar spectral shape and flux levels indicate that the same processes might be at work during the gamma-ray active states. In case of a periodic modulation with a period of about 321 days, such a behavior would be expected.

For the first time we could measure the spectrum of HESS J0632+057 between 136 and 400 GeV, and find no evidence for a spectral break or a deviation from a simple power law. This is a common feature found in other binaries which exhibit outbursts (e.g. LS I +61 303, Albert et al. 2009). Thus the turnover in the spectrum must lie below the energy threshold of our observations. All currently known gamma-ray binaries show their maximum emission in the high MeV to GeV energy range. This might be the case for HESS J0632+057 although it has not yet been detected by *Fermi*/LAT. The integration time required to detect HESS J0632+057 with *Fermi*/LAT will depend strongly on the source's duty cycle and the spectral properties at MeV to GeV energies. Assuming the shortest duty cycle compatible with our measurements (20 days) and taking the publicly available *Fermi*/LAT integral sensitivity curve [3] we find that there must be a spectral break between 140 GeV and about 10 GeV. However we note that the *Fermi*/LAT sensitivity curve is only available for extragalactic background and we scaled it by a factor of 10 to account for the higher galactic background. Since the galactic background varies

---

[3]available at:
http://fermi.gsfc.nasa.gov/ssc/data/analysis/documentation/Cicerone/Cicerone_LAT_IRFs/LAT_sensitivity.html

depending on the region inside the galaxy, the *Fermi*/LAT sensitivity might be even lower at the position of HESS J0632+057. In case of a 100 times worse sensitivity compared to the extragalactic case we still find that the system should be detectable below 1 GeV by *Fermi*/LAT.

In several recent publications the similarity between HESS J0632+057 and LS I +61 303 was stressed based on their similar multiwavelength emission (e.g. Hinton et al. 2009, Skilton et al. 2009). We note that there might be some differences in the VHE emission. LS I +61 303 shows complex VHE behavior such as variability on timescales as short as one day (e.g. Anderhub et al. 2009), and different VHE gamma-ray flux states (Acciari et al. 2011; Aleksić et al. 2012b). Revealing similar behavior in HESS J0632+057, requires higher sensitivity and better temporal sampled data than available to date and thus the degree of similarity between LS I +61 303 and HESS J0632+057 might be smaller compared to the contemporary view. Interestingly, the orbital phase lag for the detected VHE gamma-ray emission in HESS J0632+057 is quite close to that in LS I +61 303, about 0.3 after periastron passage (Li et al. 2011; Casares et al. 2012). Similar processes might produce both the X-ray and the VHE gamma-ray radiation. However, different spatial- and time-scales of the emitter, given the wider and more eccentric orbit in HESS J0632+057, and different star-emitter-observer geometries (important in the leptonic scenario), make any direct comparison difficult. A proper characterization of the radiation and magnetic fields, and of possible adiabatic losses, is required. Nevertheless, one can check, under the light of the new data (see Hinton et al. 2009 for earlier attempts), whether a leptonic model can still describe the X-ray and VHE emission of HESS J0632+057, as it is the case in LS I +61 303 (Anderhub et al. 2009).

We have assumed an homogeneous (one-zone) emitter located at the position of the compact object and at orbital phase ~ 0.3, adopting system orbital parameters given by Casares et al. (2012). The free parameters are the magnetic field (B), the electron acceleration rate ($\dot{E}$), the electron injection spectrum (Q), and the adiabatic loss timescale (t_{ad}). All these quantities have been fixed through visual comparison with the data. We have taken a magnetic to stellar photon energy density ratio of 4×10^{-4}, $\dot{E} = 0.2 \, q_e B c$, $Q \propto E^{-2}$, and $t_{\mathrm{ad}} = 3 \times 10^4$ s, to compute the radiation through synchrotron emission and inverse Compton (IC) scattering off stellar photons. The IC interaction geometry has been adopted at the orbital phase 0.3, at which gamma-ray absorption is negligible. The computed X-ray and VHE spectral energy distributions (SED) are shown in Fig.9.5, together with the MAGIC and averaged *Swift*/XRT data taken during 2011 February. This simple model provides already a very reasonable description of the data, deviating only $\sim 2\sigma$ from the lowest energy point derived by MAGIC (related to the Thomson-to-Klein-Nishina IC transition). Note however that a hadronic emission origin, although it requires an unrealistic magnetic field to explain the hard X-ray spectrum, cannot be discarded because of an X-ray luminosity in HESS J0632+057 slightly lower than at VHE (unlike LS I +61 303; see Anderhub et al. 2009).
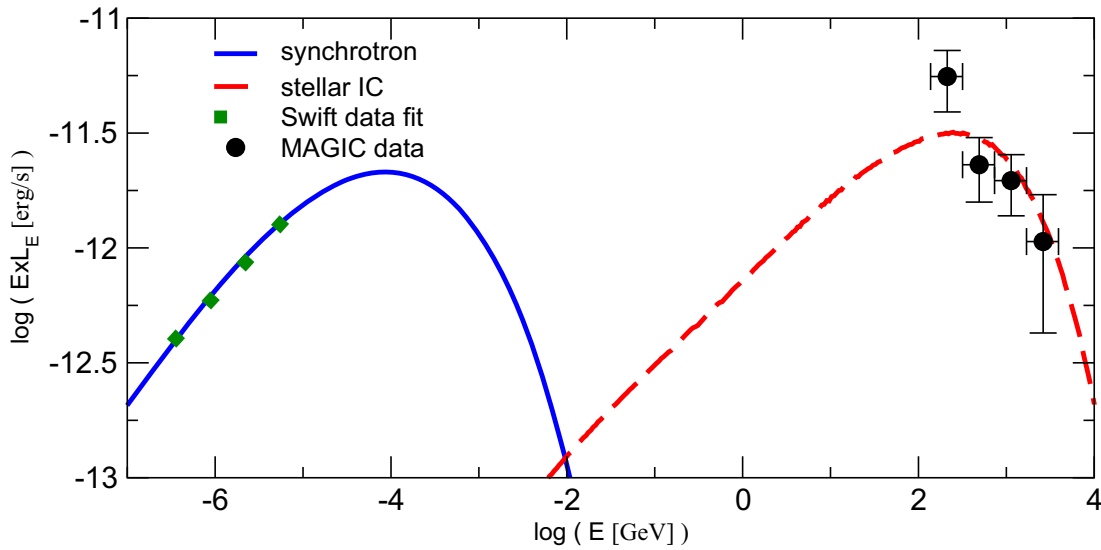
Figure 9.5: Spectral energy distribution for HESS J0632+057 as measured by MAGIC (full points) and Swift/XRT (thick dotted line) during the 2011 February outburst. We also show the modeling in a leptonic scenario where the X-ray and the VHE radiation is produced by synchrotron emission (solid line) and IC scattering off stellar photons (dashed line), respectively (see text for details).

To properly distinguish between the hadronic and leptonic pictures, and also model in detail the emitter, a better sampling of the light curve, and the X-ray/VHE spectral index correlation, are needed at the relevant orbital phases.

9.6 Conclusions

We observed the gamma-ray binary HESS J0632+057 with the MAGIC Telescopes in 2010 and 2011, covering the 2011 February X-ray outburst detected by *Swift*. We detected the system during the February observations extending the spectrum from Aharonian et al. (2007) down to $\sim$140 GeV. Our spectrum is well fit with a powerlaw with a photon index $\Gamma = 2.6 \pm 0.3_{\mathrm{stat}} \pm 0.2_{\mathrm{syst}}$ and shows no evidence of a turnover in the low-energy region. There is no evindence for variability during the February data. We modelized the emission with an homogeneous emitter at the compact object position at orbital phase $\sim$0.3. The model provides a reasonable description of our data as IC emission. However, a hadronic origin of the emission cannot be discarded.

10

Observations of the microquasar SS 433 with the MAGIC Telescopes

10.1 The SS 433 system

SS 433 is an eclipsing X-ray binary system discovered more than 30 years ago as an α emitting star in the Milky Way (Stephenson & Sanduleak 1977). This binary was the first in which relativistic jets were discovered (Spencer 1979). It is composed by an A-type super-giant star of about 30 M$_\odot$ orbited every 13.1 days by a likely BH in a circular orbit of 79 R$_\odot$ (Fabrika 2004; Cherepashchuk et al. 2005). The system is located at a distance of 5.5 ± 0.2 kpc (Blundell & Bowler 2004). However, new results from optical observations suggest that the donor star is a A4–8 I–III supergiant and the compact object a 1.56 ± 0.31 M$_\odot$ neutron star (Goranskij 2011) The system has jets moving at a velocity of $0.26c$, that precess with a period of 162.3 days in cones of half opening angle $\theta_{\mathrm{prec}} \approx 21°$ with respect to the normal to the orbital plane. The plane of the orbit, in turn subtends an angle of $i \approx 78°$ with the line of sight (Eikenberry et al. 2001).

The donor star provides a powerful flow of gas through the Roche lobe overflow, leading to a regime of continuous supercritical accretion onto the compact object via an accretion disk. This accretion regime could be responsible for the large kinetic energy in the jets, $L_{\mathrm{kin}}^{\mathrm{jet}} \sim 10^{39}$ erg s^{-1} (Dubner et al. 1998). Moreover, SS 433 is one of the two binary systems in which the presence of hadrons in their jets has been found (the other system is 4U 1630-47, Díaz Trigo et al. 2013). At growing distances from the central binary system, the jets expand and can be detected in X-rays, optical and radio bands, and are thought to be responsible of the distortion of the supernova remnant W50 shell where SS 433 is

embedded (Green 2006).

10.1.1   Gamma-ray emission and absorption processes in SS 433

SS 433 is an exceptional laboratory to test theoretical predictions of the HE and VHE emission produced in microquasar jets (see, e.g. Atoyan & Aharonian 1999; Markoff et al. 2001; Georganopoulos et al. 2002; Bosch-Ramon et al. 2006; Orellana et al. 2007). IC emission is expected by the scattering of stellar photons from the donor star and from the thick accretion disk (Gies et al. 2002; Fuchs et al. 2006) by relativistic electrons from the jet. Also synchrotron-self-Compton emission as well as relativistic Bremsstrahlung reaching VHEs would be expected from the interaction of accelerated electrons with jet ions. Finally, hadronic processes, such as pp interactions of protons in the jet leading to the emission of VHE emission by the formation and decay of π^0 must be taken into account.

The detection of VHE emission, however, can be of great difficulty since strong absorption processes are thought to be at work in this binary system: both the donor star and the compact object are thought to be embedded in a thick envelope (Zwitter et al. 1991) causing strong opacity for the propagation of VHE gamma rays. Moreover, the companion's star photon field might be also a strong source of absorption throug pair creation (Reynoso et al. 2008a).

The eclipses of the compact object when the companion star crosses the line of sight are thought to be the most important source of attenuation of the predicted gamma-ray emission. Eclipses occur every 13.1 days. Moreover, the precessional movement of the system causes that the equatorial envelope changes its inclination with respect to our line of sight and thus its attenuation of radiation may be also important. As seen in Reynoso et al. (2008b) (hereafter R08b) the precessional phases when the absorption due to the envelope is expected to be the lowest are between 0.91 and 0.09. In these phases the envelope is not blocking the jet inner regions and the probabilities for the gamma rays to escape the system are higher.

10.2   VHE observations and results

According to the ephemeris from Gies et al. (2002), precessional phase $\phi = 0$ took place on 2010 June 6.

The MAGIC telescope pointed to SS 433 for 7 nights in 2010, beginning on May 20 and lasting until June 10, for a total observation time of $\sim$10 h under dark sky and light Moon conditions. SS 433 was observed at zenith angles in the range $24°$–$30°$ using the *wobble* mode (Fomin et al. 1994) in which the telescope points at $0.4°$ offset from the true source position. This observation mode allowed to image not only the central binary system, but also the east interaction regions "e1" and "e2" (Safi-Harb & Oegelman 1997), providing in addition simultaneous background sky regions necessary for the data reduction process.

However, the study of the interaction regions is out of the scope of this thesis and only data from the central source have been analyzed.

Quality cuts based on the event rate have been applied to the entire dataset. A total amount of 7.9 hours have finally been processed through the standard MAGIC analysis chain (Albert et al. 2008a; see Appendix A for a detailed overview of the MAGIC analysis chain).

Our observations do not show any significant excess beyond 150 GeV above the background level. The 95% c.l. upper limits on the number of excess events have been calculated using the method in Rolke et al. (2005), with a systematic error of 30 %, assuming a photon spectral index $\Gamma = 2.5$. Table 10.1 summarizes the obtained integral upper limits to the emission from the central binary system. The differential upper limits are displayed in Fig. 10.1 toghether with the Crab Nebula flux for comparison.

Epoch	$\phi_{\mathrm{Prec}}{}^{a}$	$\phi_{ul}[\mathrm{ph\ cm^{-2}\ s^{-1}}]$	% c.u.^{b}
		$E > 300$ GeV	
All	0.90–0.03	1.6×10^{-12}	1.3
May	0.90–0.92	3.7×10^{-12}	3.0
June	0.01–0.03	1.8×10^{-12}	1.5
		$E > 800$ GeV	
All	0.90–0.03	3.3×10^{-13}	0.26

Table 10.1: Integral flux ULs of SS 433 (95% c.l.). Note: a: precessional phase according to Goranskij (2011) ephemeris. b: the Crab Nebula flux is $\phi_{Crab} = 1.24 \times 10^{-12}$ ph cm^{-2} s^{-1}.

10.3 Discussion

The reported upper limits to the γ-ray fluxes from SS 433 can help to constrain some physical mechanisms operating in this system. The emission in this binary system can be produced in different parts of the jet, either very close to the compact object or at further distances. It is expected that in the inner parts of the jet gamma rays will suffer strong absorption due to the companion star and the thick envelope (R08b). Besides the acceleration of particles, a dense photon and/or matter field is required in order to generate gamma rays by leptonic and/or hadronic processes. This condition is fullfilled by the contribution of the donor star and the thick envelope.

A crucial parameter in order to test the possible gamma-ray emission in SS 433 is the particle acceleration efficiency. We can define this efficiency as the ratio of relativistic non-thermal emission over the jet bulk kinetic power, $q_{\mathrm{acc}} = L_{\mathrm{nt}}/L_{\mathrm{kin}}^{\mathrm{jet}}$.

For the case of hadronic emission, R08b assume an efficiency of $q_{\mathrm{acc}}^{\mathrm{p}} = 10^{-4}$ and a jet kinetic power of $L_{\mathrm{kin}}^{\mathrm{jet}} = 10^{39}$ erg s^{-1} to compute the expected gamma-ray emission, taking also into account absorption effects due to the precession of the system. They
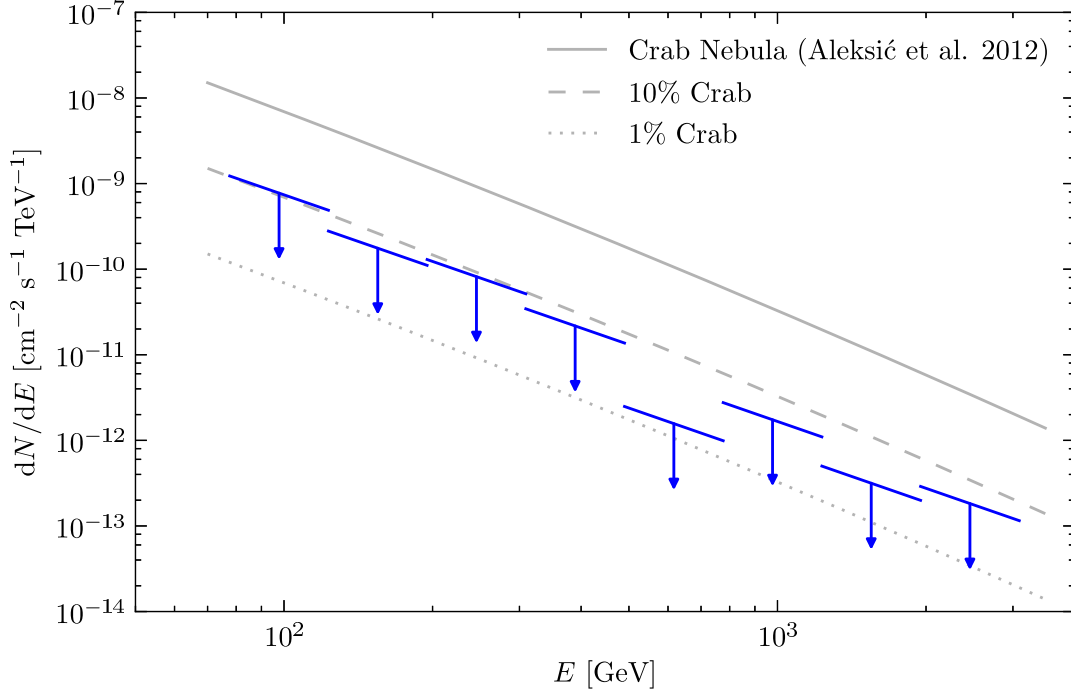
Figure 10.1: Differential 95% c.l. upper limits to the gamma-ray fluxes generated at the inner regions of SS 433 computed assuming a photon index $\Gamma = 2.5$. The three grey lines indicate, from top to bottom, the Crab Nebula flux (solid), its 10% (dashed) and its 1% (dotted) fractions. The Rolke method (Rolke et al. (2005)) with a statistical uncertainty of 30% is applied to compute the upper limits by using the excess events and the error of the background counts.

obtain a mean value for the phases with low absorption of $\phi_{\mathrm{mean}} \simeq 2 \times 10^{-12}$ ph cm^{-2} s^{-1}. Comparing the HEGRA upper limit from Aharonian et al. (2005a) with the average value from their model they obtain a more constrained value of $q^{\mathrm{p}}_{\mathrm{acc}} < 2.9 \times 10^{-4}$. It is worth noting, however, that the HEGRA measurement was taken during phases that could be different from the ones with expected low absorption. Comparing our derived UL with the averaged flux from the model in R08b we can constrain even more the value of the proton acceleration efficiency setting an upper limit of $q^{\mathrm{p}}_{\mathrm{acc}} < 1.7 \times 10^{-5}$, which is more than one order of magnitude below their limit.

Our ULs can also tell us which fraction of the total luminosity of the jet is, at most, released in the form of gamma rays. The more restrictive UL is the one for the whole dataset above 300 GeV, $F(E > 300 \text{ GeV}) < 1.6 \times 10^{-12}$ ph cm^{-2} s^{-1}. Assuming a photon spectral index $\Gamma = 2.5$ and using the estimated distance of 5.5 kpc to SS 433, the UL translates into a luminosity $L(E > 300\text{GeV}) < 8.4 \times 10^{33}$ erg s$^{-1} \simeq 8.4 \times 10^{-6} L_{\mathrm{jet}}$.

To conclude, SS 433 remains undetected at VHE. However, we have computed differ-

ential and integral upper limits which help to constrain physical parameters of the system, such as the acceleration efficiency of the protons in the jet. Further observations at VHE energies with the new generation of Cherenkov telescopes, like CTA, and at lower gamma-ray energies with *Fermi* after enough exposure time, will provide new information on the physics of this system with unique properties in our Galaxy.

11
Concluding remarks

The non-thermal emitting universe is a perfect laboratory to test some of the features of the extreme physics. Along this thesis we have explored, by means of X-ray and gamma-ray observations, the capabilities of different kind of sources to accelerate particles up to relativistic energies which, in turn, produce non-thermal radiation in several ways.

We have studied two main kinds of sources: MYSOs and binary systems containing a compact object. We summarize now the main conclusions that we reached from our research.

11.1 Young stellar objects and star-forming regions

The first part of this thesis has brought us to explore the possibility of MYSOs and SFRs to be gamma-ray emitters. After a brief introduction to the physics involved in the processes studied along this thesis, in Chapter 3 we took advantage of the public availability of the *Fermi*/LAT data to crossmatch the first *Fermi* catalog with catalogs of MYSOs, OB associations, WR and Of stars. We also studied the statistical significance of the crossmatch results by means of Monte Carlo simulations. We found interesting coincidences for MYSOs and *Fermi* sources with high statistical significance, although other possible gamma-ray counterparts cannot be ruled out. For WR and Of stars, the statistical correlation remains unclear due to the overdensity of sources in the regions where these sources are located. For OB associations the probability of chance association is negligible. However, the angular size of these associations is such that englobes several

possible gamma-ray counterparts other than young stars or MYSOs. In our work we have presented the first statistical evidence for gamma-ray emission from massive MYSOs. This work has been published in Munar-Adrover et al. (2011).

We also studied a few MYSO and SFRs candidates to be gamma-ray emitters. Those candidates came from observations and from theoretical works (Bosch-Ramon et al. 2010). The candidates are Monoceros R2 and IRAS 16547−4247, a SRF and a MYSO, respectively.

11.1.1 Monoceros R2

Monoceros R2 is a SRF located in the Unicorn constellation which contains a number of young sources within its boundaries. This source lies within the error ellipse of an unidentified *Fermi*/LAT source, 2FGL J0607.5−0618c. In the study presented in this thesis, we selected and analyzed all the available *Fermi*/LAT data on this source until 2012 April 4. Our analysis confirmed 2FGL J0607.5−0618c as a real source with emission below 2 GeV, and with parameters comparable to those reported in the Second *Fermi* point-source catalog. The spectrum fit is compatible with a powerlaw and the light-curve analysis indicates that the source is not variable at two-months timescales.

We have explored the new error circle derived from our analysis in order to find candidate counterparts to the detected gamma-ray emission. Within the error circle we find a population of ∼100 T-Tauri stars and a MYSO or group of them driving powerful outflows. All these sources have been detected in X-rays and some theoretical works predict a significant amount of gamma-ray emission from them. Given the characteristics of the detected gamma-ray emission and the population of young high-mass and low-mass protostars present in the Monoceros R2 region, we concluded that 2FGL J0607.5−0618c is compatible with being the counterpart of the collective effects of all or part of these populations of sources. Other possible origins of the gamma-ray emission cannot be ruled out, however. This study is part of the work published in Martí et al. (2013).

11.1.2 IRAS 16547−4247

IRAS 16547−4247 has been studied from the observational point of view by analyzing archival *XMM-Newton* observations and also from the theoretical point of view, by computing the expected spectral energy distribution of the lobes of this MYSO. Our X-ray analysis yielded the discovery of the X-ray counterpart of this MYSO as a hard X-ray emitter (between 4.5 and 12 keV). However, it is not clear whether the emission arises from the central protostar or from the interaction of the lobes with the parent cloud. We computed the expected non-thermal emission with a one-zone model which improves previous efforts to predict gamma-ray emission from MYSOs by introducing Coulombian losses. In our model we considered that the emission is arising from the jet-cloud interaction region. The predicted emission is incompatible with our X-ray detection. Other considerations on

the origin of the detected X-ray emission must be taken into account, such as a possible thermal origin. We introduced an absorbed thermal Bremsstrahlung component in our one-zone model. To still predict a significant amount of gamma-ray emission we also had to consider two distinct densities in the region, accounting for mixing of the material from the shocked region and the one from the unshocked part of the lobe. This assumptions allow us to explain our X-ray data and predict a significant amount of gamma rays above the GeV energy band, which might be detectable by current and future HE and VHE gamma-ray telescopes. If the detected X-ray emission is actually coming from the MYSO lobe it would be the first time that such a hard X-ray emission is detected in an X-ray source of this kind. This work has been published in Munar-Adrover et al. (2013).

11.2 High-mass X-ray binaries

In the second part of this thesis we have studied three different HMXBs by means of observations with space- and ground-based observatories. Here we remark some of the main results obtained for each studied system.

11.2.1 MWC 656

This binary system has centered out attention for the last three years since it was suggested as the optical counterpart of a gamma-ray flare detected by *AGILE*. After the confirmation of the BH nature of the compact object, our *XMM-Newton* observation allowed us to discover the X-ray counterpart of MWC 656 and thus to classify it as a HMXB, the first comprising a Be star orbited by a BH. Besides the limited quality of the obtained spectrum we could study this binary within the context of the correlation found for BH XRBs in the low/hard and quiescent states. Our results, together with the radio upper limits, are compatible with this correlation. This result is important because it indicates that the correlation might also be valid for HMXBs at very low accretion regimes. This work will be published in ApJ Letters (Munar-Adrover et al. 2014, in press).

We also observed the binary system with the MAGIC Telescopes and we did not detect the source. It is not unexpected given the X-ray luminosity and the expected low accretion regime of the BH. We conclude that even in a flaring state, this binary system might be very difficult to be detected at VHE by the current or the next generation of Cherenkov telescopes. This work will be published in the next months within the MAGIC Collaboration.

11.2.2 HESS J0632+057

We observed this binary system with the MAGIC Telescopes during a campaing between 2010 and 2011. The campaign coincided with one of the X-ray outbursts of the binary and VHE gamma rays were detected during the peak of the X-ray outburst. Although we could

not get evidence for variation in a day-by-day basis during the outburst, we could clearly see the off and on states of the source during the observation campaign. The obtained spectrum extends down to ∼140 GeV, improving the previous detection by HESS. There is no evindence for a cutoff at lower energies. We studied the obtained spectrum and explained the detection as IC scattering of stellar photons. This study is published in Aleksić et al. (2012a) (corresponding author P. Munar-Adrover).

11.2.3 SS 433

Finally, we presented our MAGIC observations of the first microquasar discovered. This binary system was observed in 2010 during the phases where we expect less absorption due to the thick envelope in which the two components of the binary are embedded. We did not detect the source during the 2010 campaign but uper limits are computed in a few energy bands. With this upper limits we can set constraints on the efficiency of the acceleration of protons in the jet and improve previous results. It seems that, if gamma rays are produced in the jet, the current generation of Cherenkov telescopes will have difficulties in detecting them, but maybe with CTA we will be able to detect this microquasar. This work will be published in the next months as a joint paper of the MAGIC and HESS Collaborations.

A

The MAGIC Telescopes

The most energetic photons arriving to the Earth interact with its atmosphere producing what is called Cherenkov light. This process is the only way we have up to now to study the most energetic emission processes taking place in the universe. In this Appendix we explain the main characteristics of the Major Atmospheric Gamma-ray Imaging Cherenkov (MAGIC) Telescopes and the analysis chain used to get the results already explained along this thesis.

A.1 The Imaging Cherenkov Telescopes

When a VHE photon enters the atmosphere it interacts with the coulombian field of the present molecules. This interaction produces a chain reaction generating electron/positron pairs, which in turn produce photons via Bremsstrahlung process that will interact with the ambient molecules again. This process takes place until the energy of the produced pairs is not enough to keep producing the interactions with the atmosphere. The produced pairs are slightly superluminical in the atmosphere and they produce Cherenkov light during their travel. The produced light reaches the ground producing a patch of 100-150 m in diameter. The energy of the parent VHE photon will determine the number of particles created during the shower development and hence the number of Cherenkov photons detectable by IACTs. However, other particles, such as hadronic cosmic rays, produce similar interactions with the atmospheric molecules, creating cascades of pions and other particles, which will give rise to Cherenkov light as well. This particles constitute the background of VHE observations.

The characteristics of the recorded shower are different for photons than for hadronic

Figure A.1: The MAGIC Telescopes.

cosmic rays. The latter are produced by particles with higher transverse momentum, which translates into a wider development of the shower. The images generated by photons have a narrower elliptical shape. The major axis of the image is the projection of the axis of the shower onto the detector.

By using more than one telescope, IACTs operate in stereoscopic mode and can better determine the origin of the cascade that produces the Cherenkov light by triggering on the same shower. It also improves the determination of the height at which the shower was originated. The background rejection is improved by observing in stereoscopic mode since the system records more precise information about the observed cascades (3D parameters) and thanks to the fact that only simultaneously triggered showers are recorded. Hence, the distance between the telescopes must be such that allows all the telescopes to see the light from a shower, typically from 70 to 150 meters.

The current population of IACTs that are operating comprises HESS, MAGIC and VERITAS. All of them operate in stereoscopic mode and share similar characteristics in spatial resolution (0.1°) and in energy threshold ($\sim$100 GeV), being MAGIC and HESS the ones with better sensitivity at lower energies.

A.2 The MAGIC Telescopes

The MAGIC Telescopes are located at the island of La Palma, in the Canary Islands, Spain, at the observatory of El Roque de Los Muchachos (28°N, 18°W, 2200 m above the sea level). The system consists in two 17 m in diameter IACTs each with a pixelized camera containing photo-multipliers, covering a field of view of $\sim 3.5°$. In 2004 the system began to observe as a single dish IACT, MAGIC I, and is has been operating in stereoscopic mode since 2009 when the second telescope (MAGIC II) ended its commissioning phase. In the last two years a major upgrade was carried out in the MAGIC I camera in order to make it equal to the MAGIC 2 one (with larger trigger area and more pixels). The electronics of both telescopes were also upgraded. The current sensitivity of the MAGIC Telescopes is 0.7% of the Crab Nebula flux in 50 h of observation for energies above 250 GeV. The spatial resolution at these energies is $\lesssim 0.1°$ and the energy resolution is $\sim 18\%$ (Sitarek et al. 2013).

A.3 The MAGIC analysis chain

The current standard analysis software package to analyze MAGIC data is MARS (Bretz et al. 2003). The data is processed following a series of steps that will be briefly described in this section.

In a first step and for each telescope individually, a calibration is made based on the calibration and pedestal runs. After that, the data is cleaned in a way that only individual pixels containing information about the shower survive, rejecting those with night sky background. Such a process provides shower images which are parametrized with the Hillas parameters (Aliu et al. 2009). In the case of stereo data, only events that are triggered by both telescopes are recorded and with those the stereo parameters are calculated. The direction of the incoming shower is determined by the intersection of the major axis of the shower image in each camera.

To determine whether the event is of hadronic nature or not, the Random Forest method is used (Albert et al. 2008b). As a result, this method assigns a parameter to each recorded shower, the so called *hadronness*, which can be understood as a probability of the event of being of hadronic origin and hence be rejected. The cuts applied in order to select the best data possible are optimized on a Crab Nebula sample of data taken under similar conditions as the current source. The energy estimation is done using look-up-tables generated from MC simulations. The signal selection uses cuts in the hadronness and in the source-independent parameter θ, which is the angular distance between the shower reconstructed and the expected source position on the camera plane (θ). For convenience, the sqared value of θ is used (θ^2), since its distribution is flat for background events while it peaks at lower values when an emitting source signal is present.

The energy spectrum is obtained by dividing the number of events by the observation effective time and by the effective area. Finally, the energy spectrum is unfolded, account-

ing for the energy resolution and possible energy reconstruction bias (Albert et al. 2007a).

In the case of observations carried out with only one of the two telescopes the analysis of the data changes slightly. To select the signal we used the source-dependent parameter α which is the angle between the major shower axis and the direction determined by the image center of gravity and the assumed (or expected) position of the source. If the shower is produced by a gamma ray, the α parameter will be small, since the shower will point approximately towards the source, whereas for hadron-produced showers, their α distribution will be isotropically distributed on the camera.

B

Exploring the minimum detectable time delay between X-ray and TeV emission in gamma-ray binaries with CTA

B.1   Introduction

The next generation of Cherenkov telescopes is embodied in the Cherenkov Telescope Array (CTA), a project that involves more than 1000 scientists from 27 countries. There will be two arrays of telescopes located in the North and in the South hemispheres. Each array will consist in ∼100 telescopes of different sizes. The biggest ones with diameters of ∼23 m will be sensitive to the lowest energies of the VHE domain (30 to 150 GeV) and will extend the current low energy limit achievable with IACTs. Intermediate and low size telescopes will be distributed in a wide area and will cover the highest energies. CTA will posses an unpredecented sensitivity in the VHE gamma-rays, improving by one order of magnitude the sensitivity of the current IACTs. The number of telescopes for each array and its distribition is still under study. For this reason, several tests and simulations have been carried out in order to characterize the expected results of observations with CTA of a number of different sources for different configurations of the arrays. In this Appendix we present a set of simulations carried out in order to test the capabilities of CTA to study delays between X-rays and VHE gamma rays.

B.2   Measuring the delay

The MAGIC collaboration reported on the existence of a correlation between the X-ray emission and VHE gamma-ray emission from the gamma-ray binary LS I +61 303 (Anderhub et al. 2009) (see however Acciari et al. 2011). The electron cooling times owing to synchrotron, IC and adiabatic losses inside the system are expected to be around a few thousand seconds (see, e.g. Zabalza et al. (2011)). If there is a time delay between the non-thermal emission at different bands (e.g., X-ray and TeV) larger than the electron cooling time scale, the emission from these bands would most likely have an origin in different locations in the binary. The detection of such a delay has been impossible with the current generation of IACTs, so here we present a study of the capability of CTA for such a study. Furthermore, since CTA will operate together with a new generation of X-ray telescopes, such as the Japanese X-ray telescope *Astro-H*, we have done this study considering the capabilities of this new instrument. LS I +61 303 is the binary system selected for this study.

Based on the short X-ray flares from LS I +61 303 detected in (Rea et al. 2010), we have chosen to model a Gaussian flare with a width of $1500\,\mathrm{s}$. In the *Chandra* observations, these flares have a baseline count rate of $0.35\,\mathrm{s}^{-1}$ and a peak of $0.8\,\mathrm{s}^{-1}$, corresponding to unabsorbed energy fluxes of ~ 8 and ~ 19 times $10^{-12}\,\mathrm{erg\,cm}^{-2}\,\mathrm{s}^{-1}$, respectively. We used these parameters to simulate the light curve detected by *Astro-H*. Using the correlation between X-rays and VHE gamma rays found in Anderhub et al. (2009) and the tools for simulating the CTA response, we generate the corresponding VHE light curves of the flare as seen by CTA array above 65 GeV in configuration I. We have used a time binning of 600 s for both the CTA and the *Astro-H* light curves (LC), and studied positive delays of the TeV light curve with respect to the X-ray light curve in the range 0 to 2000 s in steps of 100 s. We show in the top panels of Figure B.1 the simulated light curves corresponding to 500-s delay (left) and 1000-s delay (right). In the middle panels of Figure B.1 we show the X-ray fluxes as a function of the TeV fluxes in both cases. A low correlation coefficient is obtained due to a loop structure induced by the delay. When the delay is 0 the average correlation coefficient is r=0.86±0.04.

To clearly detect such delayed correlations, we have used the *z*-transformed discrete correlation function (ZDCF), which determines 68% confidence level intervals for the correlation coefficient for running values of the delay (see, e.g. Edelson & Krolik (1988)). We show in the bottom panels of Figure B.1 the ZDCF in the case of 500-s delay (left) and 1000-s delay (right). The detection of correlated signals is clear in both cases. Since the VHE LC is generated from the X-ray one, their errors are correlated and the scattering of one original (X-ray) light curve affects the second one (VHE). To correct this problem we went through simulations: we started with 100 *Astro-H* LC. With each of this 100 LC we produced 10 other X-ray LC by adding a Gaussian noise to the original ones, for each simulated delay. Then we simulated the corresponding VHE LC. At the end we had, for each delay, a sample of 1000 pairs of LC. For each pair of light curves we have calculated
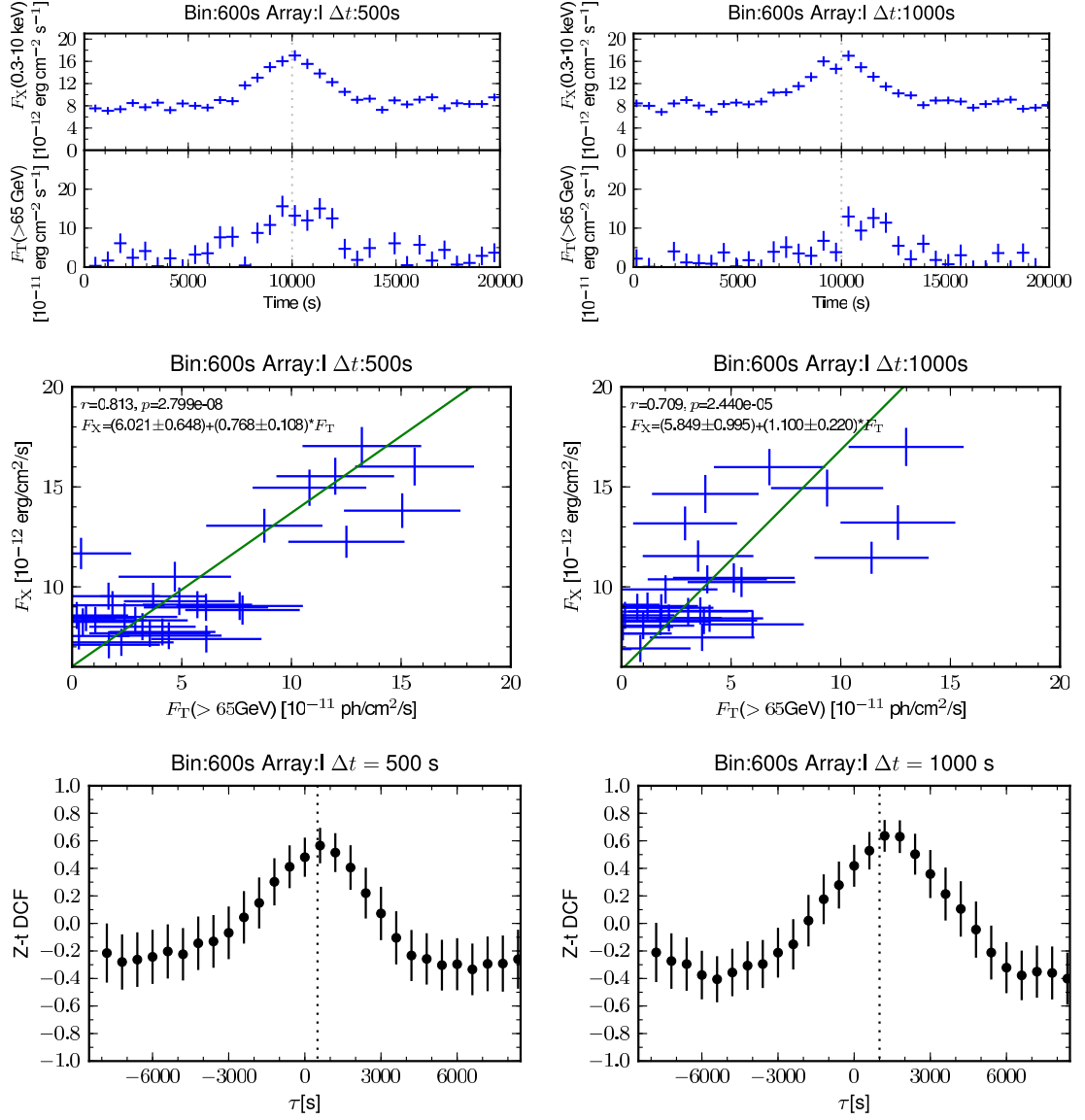
Figure B.1: CTA simulations of LS I +61 303. *Top left:*X-ray and VHE light curves of a Gaussian flare with sigma of 1500 s and 500-s delay. *Top right:* same with 1000-s delay. *Middle left:* X-ray flux vs. VHE flux for 500-s delay. *Middle right:* same with 1000-s delay. *Bottom left:* ZDCF for 500-s delay. *Bottom right:* same with 1000-s delay.

the ZDCF. To evaluate how significant is the measurement of a delay using the ZDCF we have fitted Gaussian functions to the maxima of the ZDCF. At the end we have 1000 values of the peak for each simulated delay distributed around the real delay (see Figure B.2). The measured delay is then calculated as the mean value of the distribution and its uncertainty is the standard deviation. In Figure B.3 we show the measured delay as a function of the simulated delay following the procedure described above. Considering all possible uncertainties, delays of ∼1000 s can be significantly detected at a 3σ confidence level in simultaneous light curves obtained with *Astro-H* and CTA. These results are, to first order, independent of the duration of the short flares, as far as they last longer than the binning. Overall, these results indicate that CTA will allow us to localize and constrain the X-ray ant TeV emitting regions of gamma-ray binaries and their properties.

The work presented here corresponds to a part of the article published as Paredes et al. (2013).
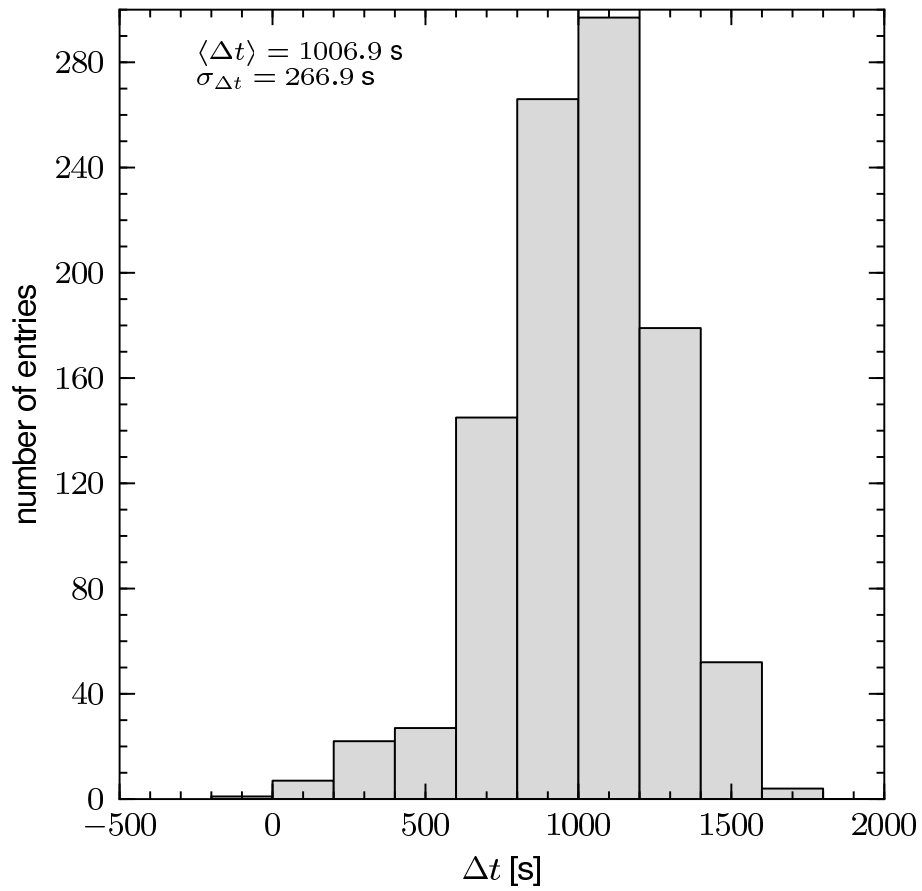
Figure B.2: Distribution of the fitted peak of the ZDCF for the simulated light curves for an introduced delay of 1000 s. A Gaussian fit gives the measured delay $\langle \Delta t \rangle$ and its standard deviation $\sigma_{\Delta t}$.
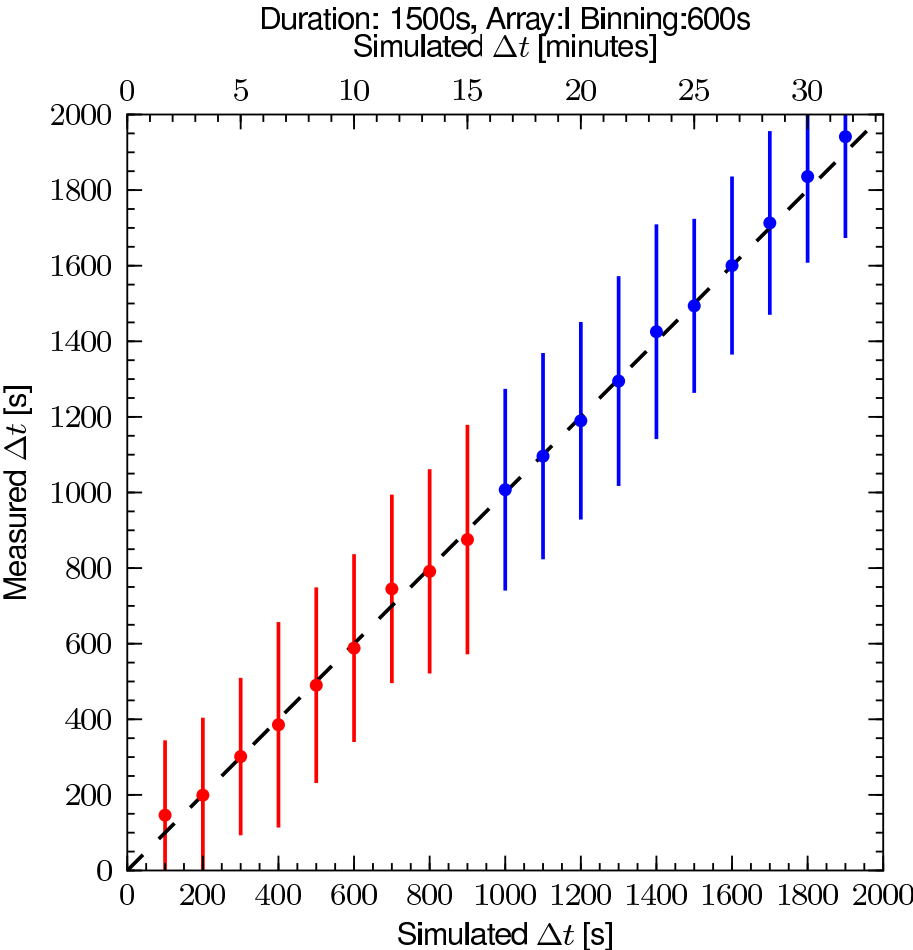
Figure B.3: CTA simulations of LS I +61 303. Measured time delay as a function of the simulated delay. Delays as short as 1000 s can be significantly measured.

C

Fermi/LAT sources coincident with OB associations

In this appendix we show the coincidences between *Fermi* sources and OB associations, which are discussed in Chapter 3, section 3.3.3.

C. Fermi/LAT sources coincident with OB associations

Table C.1: Positional coincidence of *Fermi* sources with OB associations.

Fermi Name (1FGL)	RA (°)	Dec (°)	95% Semi Major Axis (°)	Γ ($F \propto E^{-\Gamma}$)	Flux(E>100 MeV) $\times 10^{-12}$ erg cm^{-2} s^{-1}	OB association	RA (°)	Dec (°)	Distance[I] (kpc)	$\Delta\theta$ (°)	OB Size[I] (°)
J0205.6+6449	31.4090	64.8286	–	2.36±0.06	3.78±0.60	CLUST 1	31.03140	64.70406	0.89	0.20	0.9
J0214.1+6020	33.5476	60.3446	0.1624	2.1±0.2	1.95±0.68	PER 1 B	33.47470	59.59772	1.60	0.75	0.8
J0521.6+0103	80.4230	1.0512	0.1077	2.1±0.2	0.92±0	ORI 1 B	83.30102	-0.39051	0.50	3.22	6.6
J0534.7-0531	83.6872	-5.5222	0.1035	2.37±0.09	3.51±0.58	ORI 1 B	83.30102	-0.39051	0.50	5.15	6.6
J0536.2-0607	84.0623	-6.1285	0.0857	2.42±0.07	3.79±0.40	ORI 1 C	83.86341	-5.53543	0.66	0.63	3.0
J0539.4-0400	84.8703	-4.0166	0.2809	2.5±0.1	1.06±0.45	ORI 1 B	83.30102	-0.39051	0.50	3.95	6.6
J0540.4-0737	85.1220	-7.6268	0.0999	2.2±0.1	1.31±0.45	ORI 1 C	83.86341	-5.53543	0.66	2.44	3.0
J0540.9-0547	85.2317	-5.7900	0.3870	2.4±0.1	1.29±0.45	ORI 1 C	83.86341	-5.53543	0.66	1.39	3.0
J0541.9-0204	85.4885	-2.0754	0.0791	2.3±0.1	1.77±0.47	ORI 1 B	83.30102	-0.39051	0.50	2.76	6.6
J0547.0+0020	86.7698	0.3362	0.1868	2.50±0.09	1.61±0.43	ORI 1 B	83.30102	-0.39051	0.50	3.54	6.6
J0636.0+0458	99.0050	4.9806	0.0724	2.3±0.1	4.76±0.75	MON 1 B	99.37146	4.81144	1.48	0.40	0.6
J0705.9-1051	106.4985	-10.8528	0.1715	2.5±0.1	1.72±0.75	CMA 1 A	106.03646	-11.01884	0.75	0.48	1.0
J0709.0-1116	107.2576	-11.2758	0.0942	1.3±0.6	2.08±0.66	CMA 1 B	107.10737	-12.28821	1.30	1.02	1.2
J0841.9-4620	130.4865	-46.3448	0.2748	1.99±0.09	2.42±0.68	VELA 1 A	129.95838	-45.96976	1.43	0.52	1.1
J0854.0-4632	133.5039	-46.5424	0.1569	2.10±0.09	4.19±1.23	VELA 1 B	132.76816	-45.93533	1.41	0.79	1.0
J1045.2-5942	161.3059	-59.7059	0.0231	2.14±0.03	26.2±1.60	CAR 1 E	161.24112	-59.73526	2.64	0.04	1.5
J1057.2-6026	164.3242	-60.4495	0.0779	2.25±0.06	6.86±1.43	CAR 1-2	164.67677	-60.20707	2.62	0.30	0.5
J1104.0-6047	166.0209	-60.7974	0.0633	2.27±0.06	6.84±2.59	CAR 2	167.12384	-60.51125	2.16	0.61	2.5
J1106.7-6150	166.6808	-61.8449	0.0649	2.3±0.1	5.46±1.29	CAR 2	167.12384	-60.51125	2.16	1.35	2.5
J1112.1-6041	168.0486	-60.6929	0.0461	2.12±0.05	14.2±1.60	CAR 2	167.12384	-60.51125	2.16	0.49	2.5
J1115.2-6124	168.8028	-61.4022	0.1037	2.25±0.08	9.73±0	CAR 2	167.12384	-60.51125	2.16	1.21	2.5
J1119.4-6127	169.8532	-61.4528	0.0576	2.15±0.08	5.51±1.66	NGC 3576	169.66457	-61.13154	2.58	0.33	0.3
J1124.6-5916	171.1632	-59.2720	–	2.36±0.06	4.54±0.79	CAR 2	167.12384	-60.51125	2.16	2.38	2.5
J1127.7-6244	171.9345	-62.7412	0.1243	2.2±0.1	3.99±1.43	CRU 1 A	172.81985	-63.46201	2.58	0.82	1.0
J1134.8-6055	173.7198	-60.9320	0.0634	2.35±0.07	4.16±1.01	SCO 2 A	188.20526	-61.74213	0.16	7.00	8.0
J1136.0-6226	174.0206	-62.4342	0.1073	2.2±0.1	4.16±1.09	SCO 2 A	188.20526	-61.74213	0.16	6.68	8.0
J1207.4-6239	181.8754	-62.6552	0.0719	2.35±0.06	8.20±1.08	SCO 2 A	188.20526	-61.74213	0.16	3.09	8.0
J1213.7-6240	183.4475	-62.6743	0.0988	2.29±0.08	4.77±1.34	SCO 2 A	188.20526	-61.74213	0.16	2.41	8.0
J1234.0-5736	188.5059	-57.6129	0.0826	2.0±0.1	1.26±0.53	SCO 2 A	188.20526	-61.74213	0.16	4.13	8.0
J1241.6-6240	190.4160	-62.6798	0.1885	2.51±0.09	4.71±1.04	SCO 2 A	188.20526	-61.74213	0.16	1.39	8.0
J1256.1-5922	194.0496	-59.3778	0.1363	2.2±0.2	1.19±0.50	SCO 2 A	188.20526	-61.74213	0.16	3.72	8.0
J1256.9-6337	194.2482	-63.6213	0.1954	2.2±0.1	4.97±1.13	SCO 2 A	188.20526	-61.74213	0.16	3.35	8.0
J1300.7-5547	195.1930	-55.7989	0.2962	2.8±0.1	1.92±0.49	SCO 2 A	188.20526	-61.74213	0.16	6.96	8.0
J1301.4-6245	195.3587	-62.7609	0.1266	2.29±0.09	5.22±1.94	SCO 2 A	188.20526	-61.74213	0.16	3.48	8.0
J1306.4-6038	196.6202	-60.6381	0.1336	2.2±0.1	1.76±0.67	SCO 2 A	188.20526	-61.74213	0.16	4.20	8.0
J1307.3-6701	196.8482	-67.0235	0.1657	2.6±0.1	1.32±0.50	SCO 2 A	188.20526	-61.74213	0.16	6.47	8.0
J1309.9-6229	197.4964	-62.4869	0.1471	2.2±0.1	5.16±1.48	SCO 2 A	188.20526	-61.74213	0.16	4.41	8.0
J1315.0-6235	198.7644	-62.5971	0.1860	2.3±0.1	6.86±0	SCO 2 A	188.20526	-61.74213	0.16	5.00	8.0
J1317.5-6318	199.3793	-63.3037	0.0685	2.1±0.1	6.64±0	SCO 2 A	188.20526	-61.74213	0.16	5.39	8.0
J1320.6-6258	200.1639	-62.9693	0.1976	2.3±0.1	4.60±1.42	SCO 2 A	188.20526	-61.74213	0.16	5.68	8.0
J1322.0-4515	200.5154	-45.2652	0.2206	2.8±0.1	4.01±0.52	SCO 2 B	211.14639	-44.22469	0.18	7.62	7.8
J1325.6-4300	201.4148	-43.0110	0.0796	2.71±0.06	7.94±0.58	SCO 2 B	211.14639	-44.22469	0.18	7.15	7.8

Table C.1: Positional coincidence of *Fermi* sources with OB associations.

Fermi Name (1FGL)	RA (°)	Dec (°)	95% Semi Major Axis (°)	Γ ($F \propto E^{-\Gamma}$)	Flux(E>100 MeV) $\times 10^{-12}$ erg cm^{-2} s^{-1}	OB association	RA (°)	Dec (°)	Distance[l] (kpc)	$\Delta\theta$ (°)	OB Size[l] (°)
J1328.2-4729	202.0508	-47.4991	0.0986	2.1±0.1	2.53±0.51	SCO 2 B	211.14639	-44.22469	0.18	7.13	7.8
J1333.4-4036	203.3574	-40.6042	0.4217	2.7±0.1	1.80±0.40	SCO 2 B	211.14639	-44.22469	0.18	6.80	7.8
J1334.2-4448	203.5635	-44.8136	0.1873	2.4±0.1	1.23±0.46	SCO 2 B	211.14639	-44.22469	0.18	5.44	7.8
J1347.8-3751	206.9674	-37.8551	0.1517	2.7±0.1	2.13±0.39	SCO 2 B	211.14639	-44.22469	0.18	7.11	7.8
J1400.1-3743	210.0356	-37.7177	0.1705	1.9±0.2	1.67±0	SCO 2 B	211.14639	-44.22469	0.18	6.56	7.8
J1407.5-4256	211.8885	-42.9485	0.1592	2.1±0.2	1.06±0.39	SCO 2 B	211.14639	-44.22469	0.18	1.38	7.8
J1417.7-4407	214.4286	-44.1320	0.2160	2.3±0.2	1.98±0.45	SCO 2 B	211.14639	-44.22469	0.18	2.36	7.8
J1417.7-5030	214.4405	-50.5111	0.2019	2.6±0.2	1.57±0.50	SCO 2 B	211.14639	-44.22469	0.18	6.67	7.8
J1428.2-4204	217.0711	-42.0819	0.0982	2.31±0.07	2.99±0.42	SCO 2 B	211.14639	-44.22469	0.18	4.83	7.8
J1501.6-4204	225.4096	-42.0819	0.4820	2.9±0.2	1.62±0.42	SCO 2 C	228.91604	-42.39408	0.16	2.61	5.8
J1513.2-5904	228.3209	-59.0821	0.0723	1.6±0.3	6.56±0	PIS 20	229.83477	-60.14507	0.96	1.31	1.3
J1514.1-4745	228.5328	-47.7527	0.1479	2.3±0.1	1.45±0.49	SCO 2 C	228.91604	-42.39408	0.16	5.37	5.8
J1514.7-5917	228.6808	-59.2924	0.1121	1.6±0.3	4.40±0	PIS 20	229.83477	-60.14507	0.96	1.03	1.3
J1542.9-2559	235.7479	-25.9849	0.1772	2.4±0.2	1.21±0.39	SCO 2 D	243.54161	-23.91278	0.18	7.36	11.7
J1548.7-2250	237.1930	-22.8394	0.0732	2.0±0.2	1.92±0.47	SCO 2 D	243.54161	-23.91278	0.18	5.93	11.7
J1548.9-5509	237.2377	-55.1647	0.0942	2.36±0.09	3.63±0.11	NOR 1	238.67814	-54.75670	1.10	0.92	1.1
J1553.4-2425	238.3711	-24.4210	0.1813	2.4±0.2	1.30±0.44	SCO 2 D	243.54161	-23.91278	0.18	4.74	11.7
J1553.5-3116	238.3877	-31.2713	0.0718	1.7±0.2	1.17±0.39	SCO 2 D	243.54161	-23.91278	0.18	8.66	11.7
J1554.0-5345	238.5184	-53.7663	0.1074	2.24±0.07	15.6±1.63	NOR 1	238.67814	-54.75670	1.10	0.99	1.1
J1600.7-3055	240.1792	-30.9264	0.0973	1.8±0.1	1.25±0	SCO 2 D	243.54161	-23.91278	0.18	7.62	11.7
J1607.5-2030	241.9000	-20.5118	0.0681	2.3±0.2	1.29±0.42	SCO 2 D	243.54161	-23.91278	0.18	3.73	11.7
J1613.6-5100	243.4201	-51.0010	0.0661	2.20±0.06	7.65±2.34	R 103 B	243.67674	-51.07046	3.00	0.18	0.3
J1614.7-5138	243.6767	-51.6411	0.1434	2.15±0.06	12.8±1.91	R 103 A	244.40278	-51.81465	3.22	0.48	0.4
J1620.9-2731	245.2310	-27.5272	0.1896	2.4±0.1	1.49±0.48	SCO 2 D	243.54161	-23.91278	0.18	3.92	11.7
J1623.5-2345	245.8923	-23.7527	0.3570	2.3±0.1	3.62±0	SCO 2 D	243.54161	-23.91278	0.18	2.16	11.7
J1625.7-2524	246.4282	-25.4163	0.0677	2.36±0.06	4.52±1.02	SCO 2 D	243.54161	-23.91278	0.18	3.02	11.7
J1625.8-2429	246.4749	-24.4971	0.0888	2.25±0.07	7.00±1.02	SCO 2 D	243.54161	-23.91278	0.18	2.74	11.7
J1626.2-2956	246.5667	-29.9409	0.1656	2.4±0.1	1.85±0.47	SCO 2 D	243.54161	-23.91278	0.18	6.60	11.7
J1626.2-2038	246.5702	-20.6485	0.4539	2.5±0.1	1.83±0.49	SCO 2 D	243.54161	-23.91278	0.18	4.30	11.7
J1627.8-3204	246.9511	-32.0761	0.1646	2.1±0.1	1.22±0.37	SCO 2 D	243.54161	-23.91278	0.18	8.70	11.7
J1627.8-1711	246.9712	-17.1897	0.1481	2.2±0.2	0.99±0.41	SCO 2 D	243.54161	-23.91278	0.18	7.45	11.7
J1628.6-2419	247.1638	-24.3296	0.1817	2.1±0.1	4.19±0	SCO 2 D	243.54161	-23.91278	0.18	3.33	11.7
J1632.7-2431	248.1931	-24.5203	0.1713	2.3±0.1	1.79±0.63	SCO 2 D	243.54161	-23.91278	0.18	4.29	11.7
J1632.9-4802	248.2264	-48.0402	0.0527	2.17±0.05	14.0±2.85	ARA 1A A	249.78617	-48.95281	1.59	1.38	1.3
J1640.8-4634	250.2024	-46.5816	0.0969	2.32±0.04	19.2±3.08	NGC 6204	251.38377	-47.30858	1.94	1.09	1.5
J1645.0-2155	251.2549	-21.9319	0.1919	2.3±0.1	1.43±0.43	SCO 2 D	243.54161	-23.91278	0.18	7.38	11.7
J1648.4-4609	252.1112	-46.1599	0.0553	2.29±0.05	15.9±3.98	NGC 6204	251.38377	-47.30858	1.94	1.25	1.5
J1702.4-4147	255.6043	-41.7857	0.1040	2.50±0.07	4.07±0.53	SCO 1	253.59121	-41.50018	1.92	1.53	1.9
J1715.2-3319	258.8207	-33.3323	0.1397	2.3±0.1	3.11±0	SCO 4	258.66248	-33.68906	1.23	0.38	1.2
J1717.9-3343	259.4985	-33.7269	0.0832	2.42±0.05	6.88±1.03	SCO 4	258.66248	-33.68906	1.23	0.70	1.2
J1732.3-3243	263.0869	-32.7293	0.1243	2.33±0.05	13.9±1.91	TR 27	263.17260	-32.92243	1.31	0.21	1.1
J1810.9-1905	272.7486	-19.0843	0.0878	2.26±0.06	11.0±1.42	SGR 4	273.93407	-18.92533	1.85	1.13	1.5
J1811.3-1959	272.8294	-19.9920	0.0985	2.1±0.2	5.75±0	SGR 7	273.41595	-20.64018	1.28	0.85	0.8
J1814.0-1736	273.5201	-17.6008	0.0470	2.34±0.04	14.8±1.69	SGR 4	273.93407	-18.92533	1.85	1.38	1.5
J1817.6-1651	274.4099	-16.8602	0.1466	2.30±0.06	5.91±2.77	SER 1 A	275.20333	-16.63491	1.50	0.79	1.5
J1818.7-1557	274.6776	-15.9591	0.1114	2.34±0.07	12.4±1.92	SER 1 A	275.20333	-16.63491	1.50	0.84	0.9
J1821.1-1425	275.2907	-14.4198	0.0837	2.26±0.06	7.58±2.34	SCT 3	276.31989	-14.33074	1.48	1.00	0.9
J1823.2-1336	275.8135	-13.6060	0.0738	2.12±0.05	16.3±2.77	SCT 3	276.31989	-14.33074	1.48	0.88	1.1

Continued on next page

Table C.1: Positional coincidence of *Fermi* sources with OB associations.

Fermi Name (1FGL)	RA (°)	Dec (°)	95% Semi Major Axis (°)	Γ (F ∝ E^−Γ)	Flux(E>100 MeV) ×10^−12 erg cm^−2 s^−1	OB association	RA (°)	Dec (°)	Distance[1] (kpc)	Δθ (°)	OB Size[1] (°)
J1825.7-1410	276.4394	-14.1818	0.0553	1.1±0.3	6.86±2.29	SCT 3	276.31989	-14.33074	1.48	0.19	1.1
J1826.2-1450	276.5630	-14.8481	-	2.38±0.03	28.7±2.31	SCT 3	276.31989	-14.33074	1.48	0.57	1.1
J1943.4+2340	295.8670	23.6818	0.1118	2.2±0.1	2.62±0.67	VUL 4	296.49937	24.37678	1.21	0.90	1.0
J1948.6+2437	297.1532	24.6293	0.1326	2.2±0.1	2.26±0.68	VUL 4	296.49937	24.37678	1.21	0.65	1.0
J2015.7+3708	303.9291	37.1402	0.0400	2.26±0.03	13.9±1.37	CYG 1,8,9	305.03403	38.92113	1.37	1.98	4.9
J2020.0+4049	305.0036	40.8191	0.1014	2.12±0.08	8.16±3.01	CYG 1,8,9	305.03403	38.92113	1.37	1.90	4.9
J2021.5+4026	305.3817	40.4460	-	2.25±0.01	97.2±3.48	CYG 1,8,9	305.03403	38.92113	1.37	1.55	4.9
J2030.0+3641	307.5021	36.6844	0.0559	2.10±0.07	3.42±1.07	CYG 1,8,9	305.03403	38.92113	1.37	2.97	4.9
J2032.8+3928	308.2006	39.4703	0.2507	2.59±0.07	5.12±1.39	CYG 1,8,9	305.03403	38.92113	1.37	2.51	4.9
J2034.7+3639	308.6968	36.6512	0.1254	2.2±0.1	2.30±0.69	CYG 1,8,9	305.03403	38.92113	1.37	3.68	4.9
J2040.0+4157	310.0158	41.9536	0.1970	2.66±0.06	7.92±1.19	CYG 1,8,9	305.03403	38.92113	1.37	4.86	4.9
J2207.5+6440	331.8799	64.6720	0.1971	2.65±0.08	4.14±0.52	CEP 2 B	328.84072	61.71559	0.77	3.26	3.6
J2214.5+5949	333.6453	59.8288	0.1184	2.4±0.1	2.23±0.62	CEP 2 B	328.84072	61.71559	0.77	3.01	3.6
J2243.4+4104	340.8659	41.0733	0.1923	2.6±0.2	1.71±0	LAC 1	339.37867	39.90053	0.63	1.63	1.7
J2250.8+6336	342.7210	63.6153	0.0687	2.33±0.07	3.39±0.43	CEP 3	344.37054	62.90856	0.84	1.02	1.9

Continued on next page

[1]From Cruz-González et al. (1974)

References

Abdo, A. A., Ackermann, M., Ajello, M., et al. 2010, ApJSS, 188, 405

Abdo, A. A., Ackermann, M., Ajello, M., et al. 2009, Astrophysical Journal, Letters, 706, L1

Abell, G. O. & Margon, B. 1979, Nature, 279, 701

Acciari, V. A., Aliu, E., Arlen, T., et al. 2011, ApJ, 738, 3

Acciari, V. A., Aliu, E., Arlen, T., et al. 2009, Astrophysical Journal, Letters, 698, L94

Ackermann, M., Ajello, M., Albert, A., et al. 2012, ApJSS, 203, 4

Aharonian, F., Akhperjanian, A., Beilicke, M., et al. 2005a, A&A, 439, 635

Aharonian, F., Akhperjanian, A. G., Aye, K.-M., et al. 2005b, A&A, 442, 1

Aharonian, F., Akhperjanian, A. G., Bazer-Bachi, A. R., et al. 2006, A&A, 460, 743

Aharonian, F. A. 2004, Very high energy cosmic gamma radiation : a crucial window on the extreme Universe

Aharonian, F. A., Akhperjanian, A. G., Bazer-Bachi, A. R., et al. 2007, A&A, 469, L1

Aharonian, F. A. & Atoyan, A. M. 1981, A&SS, 79, 321

Aharonian, F. A. & Atoyan, A. M. 1996, A&A, 309, 917

Aharonian, F. A. & Atoyan, A. M. 2000, A&A, 362, 937

Albert, J., Aliu, E., Anderhub, H., et al. 2009, ApJ, 693, 303

Albert, J., Aliu, E., Anderhub, H., et al. 2006, Science, 312, 1771

Albert, J., Aliu, E., Anderhub, H., et al. 2008a, Nuclear Instruments and Methods in Physics Research A, 594, 407

Albert, J., Aliu, E., Anderhub, H., et al. 2008b, Nuclear Instruments and Methods in Physics Research A, 588, 424

Albert, J., Aliu, E., Anderhub, H., et al. 2007a, Nuclear Instruments and Methods in Physics Research A, 583, 494

Albert, J., Aliu, E., Anderhub, H., et al. 2007b, Astrophysical Journal, Letters, 665, L51

Aleksić, J., Alvarez, E. A., Antonelli, L. A., et al. 2012a, Astrophysical Journal, Letters, 754, L10

Aleksić, J., Alvarez, E. A., Antonelli, L. A., et al. 2012b, ApJ, 746, 80

Aliu, E., Anderhub, H., Antonelli, L. A., et al. 2009, Astroparticle Physics, 30, 293

Allington-Smith, J. R., Perryman, M. A. C., Longair, M. S., Gunn, J. E., & Westphal, J. A. 1982, MNRAS, 201, 331

REFERENCES

Anderhub, H., Antonelli, L. A., Antoranz, P., et al. 2009, Astrophysical Journal, Letters, 706, L27

Aragona, C., McSwain, M. V., & De Becker, M. 2010, ApJ, 724, 306

Araudo, A. T. & Rodríguez, L. F. 2012, in American Institute of Physics Conference Series, Vol. 1505, American Institute of Physics Conference Series, ed. F. A. Aharonian, W. Hofmann, & F. M. Rieger, 281–284

Araudo, A. T., Romero, G. E., Bosch-Ramon, V., & Paredes, J. M. 2007, A&A, 476, 1289

Arnaud, K. A. 1996, in Astronomical Society of the Pacific Conference Series, Vol. 101, Astronomical Data Analysis Software and Systems V, ed. G. H. Jacoby & J. Barnes, 17

Atoyan, A. M. & Aharonian, F. A. 1999, MNRAS, 302, 253

Bally, J. & Lada, C. J. 1983, ApJ, 265, 824

Banerjee, R. & Pudritz, R. E. 2006, ApJ, 641, 949

Banerjee, R. & Pudritz, R. E. 2007, ApJ, 660, 479

Beckwith, S., Evans, II, N. J., Becklin, E. E., & Neugebauer, G. 1976, ApJ, 208, 390

Bednarek, W. & Giovannelli, F. 2007, A&A, 464, 437

Belczynski, K. & Ziolkowski, J. 2009, ApJ, 707, 870

Benaglia, P. & Romero, G. E. 2003, A&A, 399, 1121

Berghoefer, T. W., Schmitt, J. H. M. M., Danner, R., & Cassinelli, J. P. 1997, A&A, 322, 167

Beuther, H., Kerp, J., Preibisch, T., Stanke, T., & Schilke, P. 2002a, A&A, 395, 169

Beuther, H., Schilke, P., Sridharan, T. K., et al. 2002b, A&A, 383, 892

Binns, W. R., Wiedenbeck, M. E., Arnould, M., et al. 2008, New Astronomy Review, 52, 427

Blondin, J. M., Konigl, A., & Fryxell, B. A. 1989, Astrophysical Journal, Letters, 337, L37

Blumenthal, G. R. & Gould, R. J. 1970, Reviews of Modern Physics, 42, 237

Blundell, K. M. & Bowler, M. G. 2004, Astrophysical Journal, Letters, 616, L159

Bodaghee, A., Tomsick, J. A., Pottschmidt, K., et al. 2013, ApJ, 775, 98

Bohlin, R. C., Savage, B. D., & Drake, J. F. 1978, ApJ, 224, 132

Bongiorno, S. D., Falcone, A. D., Stroh, M., et al. 2011, Astrophysical Journal, Letters, 737, L11

Bosch-Ramon, V. & Khangulyan, D. 2009, International Journal of Modern Physics D, 18, 347

Bosch-Ramon, V., Romero, G. E., Araudo, A. T., & Paredes, J. M. 2010, A&A, 511, A8

Bosch-Ramon, V., Romero, G. E., & Paredes, J. M. 2006, A&A, 447, 263

Bretz, T., Wagner, R., & MAGIC Collaboration. 2003, International Cosmic Ray Conference, 5, 2947

Bulgarelli, A., Pittori, C., Lucarelli, F., et al. 2010, The Astronomer's Telegram, 2512, 1

Cameron, P. B. & Kulkarni, S. R. 2007, Astrophysical Journal, Letters, 665, L135

Carpenter, J. M. & Hodapp, K. W. 2008, The Monoceros R2 Molecular Cloud, ed. B. Reipurth, 899

Carpenter, J. M., Meyer, M. R., Dougados, C., Strom, S. E., & Hillenbrand, L. A. 1997, AJ, 114, 198

Carrasco-González, C., Rodríguez, L. F., Anglada, G., et al. 2010, Science, 330, 1209

Casares, J., Negueruela, I., Ribó, M., et al. 2014, Nature, 505, 378

Casares, J., Ribó, M., Ribas, I., et al. 2012, MNRAS, 421, 1103

Chaves, R. C. G., Renaud, M., Lemoine-Goumard, M., & Goret, P. 2008, in American Institute of Physics Conference Series, Vol. 1085, American Institute of Physics Conference Series, ed. F. A. Aharonian, W. Hofmann, & F. Rieger, 372–375

Cherepashchuk, A. M., Sunyaev, R. A., Fabrika, S. N., et al. 2005, A&A, 437, 561

Cohen, D. H., Cassinelli, J. P., & Macfarlane, J. J. 1997, ApJ, 487, 867

Condon, J. J., Cotton, W. D., Greisen, E. W., et al. 1998, AJ, 115, 1693

Corbel, S., Coriat, M., Brocksopp, C., et al. 2013, MNRAS, 428, 2500

Coriat, M., Corbel, S., Prat, L., et al. 2011, MNRAS, 414, 677

Cruz-González, C., Recillas-Cruz, E., Costero, R., Peimbert, M., & Torres-Peimbert, S. 1974, Rev. Mex. Astron. Astrofis., 1, 211

del Valle, M. V., Romero, G. E., Luque-Escamilla, P. L., Martí, J., & Sánchez-Sutil, J. R. 2011, ApJ, 738, 115

Dhawan, V., Mioduszewski, A., & Rupen, M. 2006, in VI Microquasar Workshop: Microquasars and Beyond

Dhawan, V., Mirabel, I. F., & Rodríguez, L. F. 2000, ApJ, 543, 373

Díaz Trigo, M., Miller-Jones, J. C. A., Migliari, S., Broderick, J. W., & Tzioumis, T. 2013, Nature, 504

Dickey, J. M. & Lockman, F. J. 1990, ARA&A, 28, 215

Dougherty, S. M., Pittard, J. M., Kasian, L., et al. 2003, A&A, 409, 217

Drury, L. O. 1983, Reports on Progress in Physics, 46, 973

Dubner, G. M., Holdaway, M., Goss, W. M., & Mirabel, I. F. 1998, AJ, 116, 1842

Dubus, G. 2006, A&A, 456, 801

Dutra, C. M., Bica, E., Soares, J., & Barbuy, B. 2003, A&A, 400, 533

Edelson, R. A. & Krolik, J. H. 1988, ApJ, 333, 646

Eikenberry, S. S., Cameron, P. B., Fierce, B. W., et al. 2001, ApJ, 561, 1027

Fabian, A. C. 1980, MNRAS, 192, 11P

Fabrika, S. 2004, Astrophysics and Space Physics Reviews, 12, 1

Falcone, A. D., Grube, J., Hinton, J., et al. 2010, Astrophysical Journal, Letters, 708, L52

Feigelson, E. D. & Montmerle, T. 1999, ARA&A, 37, 363

Fender, R. 2010, in Lecture Notes in Physics, Berlin Springer Verlag, Vol. 794, Lecture Notes in Physics, Berlin Springer Verlag, ed. T. Belloni, 115

Fermi LAT Collaboration, Abdo, A. A., Ackermann, M., et al. 2009, Science, 326, 1512

REFERENCES

Fomin, V. P., Stepanian, A. A., Lamb, R. C., et al. 1994, Astroparticle Physics, 2, 137

Fuchs, Y., Koch Miramond, L., & Ábrahám, P. 2006, A&A, 445, 1041

Gallo, E. 2007, in American Institute of Physics Conference Series, Vol. 924, The Multi-colored Landscape of Compact Objects and Their Explosive Origins, ed. T. di Salvo, G. L. Israel, L. Piersant, L. Burderi, G. Matt, A. Tornambe, & M. T. Menna, 715–722

Gallo, E. & Fender, R. P. 2002, MNRAS, 337, 869

Gallo, E., Fender, R. P., & Pooley, G. G. 2003, MNRAS, 344, 60

Gallo, E., Miller, B. P., & Fender, R. 2012, MNRAS, 423, 590

Garay, G., Brooks, K. J., Mardones, D., & Norris, R. P. 2003, ApJ, 587, 739

Garay, G. & Lizano, S. 1999, PASP, 111, 1049

Georganopoulos, M., Aharonian, F. A., & Kirk, J. G. 2002, A&A, 388, L25

Gies, D. R., McSwain, M. V., Riddle, R. L., et al. 2002, ApJ, 566, 1069

Ginzburg, V. L. & Syrovatskii, S. I. 1964, The Origin of Cosmic Rays, New York: Macmillan, 1964

Ginzburg, V. L. & Syrovatskij, S. I. 1967, in IAU Symposium, Vol. 31, Radio Astronomy and the Galactic System, ed. H. van Woerden, 411

Goranskij, V. 2011, Peremennye Zvezdy, 31, 5

Green, D. A. 2006

Gyulbudaghian, A. L., Glushkov, Y. I., & Denisyuk, E. K. 1978, Astrophysical Journal, Letters, 224, L137

Herbst, W. & Racine, R. 1976, AJ, 81, 840

Hinton, J. A., Skilton, J. L., Funk, S., et al. 2009, Astrophysical Journal, Letters, 690, L101

Homan, J. & Belloni, T. 2005, A&SS, 300, 107

Kaul, R. K. & Mitra, A. K. 1997, in American Institute of Physics Conference Series, Vol. 410, Proceedings of the Fourth Compton Symposium, ed. C. D. Dermer, M. S. Strickman, & J. D. Kurfess, 1271–1274

Kelner, S. R., Aharonian, F. A., & Bugayov, V. V. 2006, Physical Review D, 74, 034018

Lang, K. R. 1999, Astrophysical formulae / K.R. Lang. New York : Springer, 1999. (Astronomy and astrophysics library,ISSN0941-7834)

Li, J., Torres, D. F., Zhang, S., et al. 2011, ApJ, 733, 89

Li, T.-P. & Ma, Y.-Q. 1983, ApJ, 272, 317

Longair, M. S. 2011, High Energy Astrophysics, by Malcolm S. Longair, Cambridge, UK: Cambridge University Press, 2011

López-Oramas, A., Blanch Bigas, O., Cortina, J., et al. 2013, ArXiv e-prints

López-Santiago, J., Peri, C. S., Bonito, R., et al. 2013, Astrophysical Journal, Letters, 776, L22

Lucarelli, F., Verrecchia, F., Striani, E., et al. 2010, The Astronomer's Telegram, 2761, 1

Mahony, E. K., Sadler, E. M., Murphy, T., et al. 2010, ApJ, 718, 587

Maraschi, L. & Treves, A. 1981, MNRAS, 194, 1P

Markoff, S., Falcke, H., & Fender, R. 2001, A&A, 372, L25

Markoff, S., Nowak, M. A., & Wilms, J. 2005, ApJ, 635, 1203

Martí, J., Luque-Escamilla, P. L., Muñoz-Arjonilla, A. J., et al. 2013, A&A, 556, A131

Martí, J., Rodríguez, L. F., & Reipurth, B. 1993, ApJ, 416, 208

Massi, M., Ros, E., & Zimmermann, L. 2012, A&A, 540, A142

Mel'Nik, A. M. & Efremov, Y. N. 1995, Astronomy Letters, 21, 10

Mirabel, I. F. 2006, Science, 312, 1759

Mirabel, I. F., Rodríguez, L. F., Cordier, B., Paul, J., & Lebrun, F. 1992, Nature, 358, 215

Mitsuda, K., Inoue, H., Koyama, K., et al. 1984, PASJ, 36, 741

Moldón, J. 2012, PhD thesis, Universitat de Barcelona

Moldón, J., Ribó, M., & Paredes, J. M. 2011, A&A, 533, L7

Moldón, J., Ribó, M., & Paredes, J. M. 2012, A&A, 548, A103

Montmerle, T. & André, P. 1989, in European Southern Observatory Conference and Workshop Proceedings, Vol. 33, European Southern Observatory Conference and Workshop Proceedings, ed. B. Reipurth, 407–422

Morrison, R. & McCammon, D. 1983, ApJ, 270, 119

Munar-Adrover, P., Bosch-Ramon, V., Paredes, J. M., & Iwasawa, K. 2013, A&A, 559, A13

Munar-Adrover, P., Paredes, J. M., Bosch-Ramon, V., & Iwasawa, K. 2012, in American Institute of Physics Conference Series, Vol. 1505, American Institute of Physics Conference Series, ed. F. A. Aharonian, W. Hofmann, & F. M. Rieger, 285–288

Munar-Adrover, P., Paredes, J. M., Ribó, M., et al. 2014, Astrophysical Journal, Letters, in press

Munar-Adrover, P., Paredes, J. M., & Romero, G. E. 2011, A&A, 530, A72

Nakajima, H., Imanishi, K., Takagi, S.-I., Koyama, K., & Tsujimoto, M. 2003, PASJ, 55, 635

Nazé, Y. 2009, A&A, 506, 1055

Nolan, P. L., Abdo, A. A., Ackermann, M., et al. 2012, ApJSS, 199, 31

Nowak, M. A. & Wilms, J. 1999, ApJ, 522, 476

Orellana, M., Bordas, P., Bosch-Ramon, V., Romero, G. E., & Paredes, J. M. 2007, A&A, 476, 9

Pacholczyk, A. G. 1970, Radio astrophysics. Nonthermal processes in galactic and extragalactic sources, Ed. Freeman & Company

Paredes, J. M., Bednarek, W., Bordas, P., et al. 2013, Astroparticle Physics, 43, 301

Paredes-Fortuny, X., Ribó, M., Fors, O., & Núñez, J. 2012, in American Institute of Physics Conference Series, Vol. 1505, American Institute of Physics Conference Series, ed. F. A. Aharonian, W. Hofmann, & F. M. Rieger, 390–393

REFERENCES

Plotkin, R. M., Gallo, E., & Jonker, P. G. 2013, ApJ, 773, 59

Pravdo, S. H., Tsuboi, Y., Suzuki, Y., Thompson, T. J., & Rebull, L. 2009, ApJ, 690, 850

Preibisch, T., Balega, Y. Y., Schertl, D., & Weigelt, G. 2002, A&A, 392, 945

Protheroe, R. J. 1999, in Topics in Cosmic-Ray Astrophysics, ed. M. A. Duvernois, 247

Ragan, S. E., Bergin, E. A., Plume, R., et al. 2006, ApJSS, 166, 567

Rea, N. & Torres, D. F. 2011, Astrophysical Journal, Letters, 737, L12

Rea, N., Torres, D. F., van der Klis, M., et al. 2010, MNRAS, 405, 2206

Reipurth, B. & Bally, J. 2001, ARA&A, 39, 403

Remillard, R. A. & McClintock, J. E. 2006, ARA&A, 44, 49

Reynoso, M. M., Christiansen, H. R., & Romero, G. E. 2008a, Astroparticle Physics, 28, 565

Reynoso, M. M., Romero, G. E., & Christiansen, H. R. 2008b, MNRAS, 387, 1745

Rodríguez, L. F., Curiel, S., Moran, J. M., et al. 1989, Astrophysical Journal, Letters, 346, L85

Rodríguez, L. F., Moran, J. M., Franco-Hernández, R., et al. 2008, AJ, 135, 2370

Rolke, W. A., López, A. M., & Conrad, J. 2005, Nuclear Instruments and Methods in Physics Research A, 551, 493

Romero, G. E. 2008, in American Institute of Physics Conference Series, Vol. 1085, American Institute of Physics Conference Series, ed. F. A. Aharonian, W. Hofmann, & F. Rieger, 97–103

Romero, G. E., Benaglia, P., & Torres, D. F. 1999, A&A, 348, 868

Russeil, D. & Castets, A. 2004, A&A, 417, 107

Rybicki, G. B. & Lightman, A. P. 1979, Radiative processes in astrophysics, Ed. Wiley-Interscience

Sabatini, S., Striani, E., Verrecchia, F., et al. 2010, The Astronomer's Telegram, 2715, 1

Safi-Harb, S. & Oegelman, H. 1997, ApJ, 483, 868

Sitarek, J., Carmona, E., Colin, P., et al. 2013, ArXiv e-prints

Skilton, J. L., Pandey-Pommier, M., Hinton, J. A., et al. 2009, MNRAS, 399, 317

Smits, D. P., Cohen, R. J., & Hutawarakorn, B. 1998, MNRAS, 296, L11

Sokal, K. R., Skinner, S. L., Zhekov, S. A., Güdel, M., & Schmutz, W. 2010, ApJ, 715, 1327

Spencer, R. E. 1979, Nature, 282, 483

Sridharan, T. K., Beuther, H., Schilke, P., Menten, K. M., & Wyrowski, F. 2002, ApJ, 566, 931

Stephenson, C. B. & Sanduleak, N. 1977, ApJSS, 33, 459

Stirling, A. M., Spencer, R. E., de la Force, C. J., et al. 2001, MNRAS, 327, 1273

Straizys, V. & Kuriliene, G. 1981, A&SS, 80, 353

Tavani, M., Sabatini, S., Pian, E., et al. 2009, Astrophysical Journal, Letters, 698, L142

Torres, D. F., Domingo-Santamaría, E., & Romero, G. E. 2004, Astrophysical Journal, Letters, 601, L75

Tsuboi, Y., Koyama, K., Murakami, H., et al. 1998, ApJ, 503, 894

Urquhart, J. S., Hoare, M. G., Lumsden, S. L., Oudmaijer, R. D., & Moore, T. J. T. 2008, in Astronomical Society of the Pacific Conference Series, Vol. 387, Massive Star Formation: Observations Confront Theory, ed. H. Beuther, H. Linz, & T. Henning, 381

van den Bergh, S. 1966, AJ, 71, 990

van der Hucht, K. A. 2001, New Astronomy Review, 45, 135

van der Hucht, K. A. 2006, A&A, 458, 453

Voelk, H. J. & Forman, M. 1982, ApJ, 253, 188

Walsh, A. J., Burton, M. G., Hyland, A. R., & Robinson, G. 1998, MNRAS, 301, 640

Williams, P. M., van der Hucht, K. A., van der Woerd, H., Wamsteker, W. M., & Geballe, T. R. 1987, in Astrophysics and Space Science Library, Vol. 136, Instabilities in Luminous Early Type Stars, ed. H. J. G. L. M. Lamers & C. W. H. De Loore, 221–226

Williams, S. J., Gies, D. R., Matson, R. A., et al. 2010, Astrophysical Journal, Letters, 723, L93

Wilner, D. J., Reid, M. J., & Menten, K. M. 1999, ApJ, 513, 775

Wolf, G. A., Lada, C. J., & Bally, J. 1990, AJ, 100, 1892

Zabalza, V., Paredes, J. M., & Bosch-Ramon, V. 2011, A&A, 527, A9

Zdziarski, A. A. 2012, MNRAS, 422, 1750

Zdziarski, A. A., Poutanen, J., Mikolajewska, J., et al. 1998, MNRAS, 301, 435

Zwitter, T., Calvani, M., & D'Odorico, S. 1991, A&A, 251, 92

List of Figures

List of Tables

List of Acronyms

AGN   Active galactic nuclei

BH   Black hole

BHXB   Black hole X-ray binary

CR   Cosmic Ray

CTA   Cherenkov Telescope Array

DSA   Diffussive shock acceleration

EGRET   Energetic Gamma Ray Experiment Telescope

EVN   European VLBI network

FS   Forward shock

GBM   Gamma-ray Burst Monitor

GMRT   Giant Metrewave Radio Telescope

GRB   Gamma-ray burst

HE   High Energy

HESS   High Energy Stereoscopic System

HMXB   High-mass X-ray binary

IACT   Imaging Atmospheric Cherenkov Telescope

IC   Inverse Compton

IR   Infrared

IRF   Instrument response function

ISM   Interstellar medium

LAT   Large Area Telescope

LC   Light curve

LMXB   Low-mass X-ray binary

MAGIC   Major Atmospheric Gamma-ray Imaging Cherenkov

MC   Monte Carlo

MYSO   Massive young stellar object

NDP   Non detection period

NS   Neutron star

PWN   Pulsar wind nebula

RMS   Red MSX Source

ROI   Region of interest

RS   Reverse shock

SED   Spectral energy distribution

SFR   Star-forming region

SNR   Supernova remnant

TS   Test statistic

VERITAS   Very Energetic Radiation Imaging Telescope Array System

VHE   Very high energy

VLA   Very Large Array

VLBI   Very long baseline interferometry

WR   Wolf Rayet

XRB   X-ray binary

YSO   Young stellar object

ZDCF   Z-transformed Discrete Correlation Function